2016-06-14

Modeling the Biomechanics and Mechanobiology of Intervertebral Discs

Xin Gao
University of Miami, xingao@outlook.com

UNIVERSITY OF MIAMI

MODELING THE BIOMECHANICS AND MECHANOBIOLOGY OF INTERVERTEBRAL DISCS

By

Xin Gao

A DISSERTATION

Submitted to the Faculty
of the University of Miami
in partial fulfillment of the requirements for
the degree of Doctor of Philosophy

Coral Gables, Florida

August 2016

UNIVERSITY OF MIAMI

A dissertation submitted in partial fulfillment of
the requirements for the degree of
Doctor of Philosophy

MODELING THE BIOMECHANICS AND MECHANOBIOLOGY OF INTERVERTEBRAL DISCS

Xin Gao

Approved:

_____
Weiyong Gu, Ph.D.
Professor of
Mechanical and Aerospace Engineering
and Biomedical Engineering

_____
Chun-Yuh Huang, Ph.D.
Associate Professor of
Biomedical Engineering

_____
Qingda Yang, Ph.D.
Associate Professor of
Mechanical and Aerospace Engineering

_____
Guillermo Prado, Ph.D.
Dean of the Graduate School

_____
Landon R. Grace, Ph.D.
Assistant Professor of
Mechanical and Aerospace Engineering

GAO, XIN (Ph.D., Mechanical Engineering)

Modeling the Biomechanics and Mechanobiology of Intervertebral Discs (August 2016)

Abstract of a dissertation at the University of Miami.

Dissertation supervised by Professor Weiyong Gu
No. of pages in text. (142)

The degeneration of lumbar intervertebral discs (IVDs) has been implicated as a possible cause of low back pain which affects more than 600 million people worldwide. Abnormal mechanical loading is thought to be a primary etiological factor leading to degenerative changes in the discs. The abnormal mechanical loading could initiate disc degeneration through two pathways: causing the failure of disc structures, and disturbing the balance between cellular anabolic and catabolic activities. The latter one is thought to be the main pathway. However, the mechanism of extracellular mechanotransduction is not fully understood, neither the abnormal mechanical loading is quantified. The objectives of this dissertation were to develop mathematical models to characterize the biomechanics and mechanobiology of discs in order to quantify the abnormal mechanical loading and delineate how the cells perceive and respond to mechanical stimuli.

A new constitutive model for hydration-dependent aggregate modulus of soft and hydrated materials was developed based on the biphasic theory and transport models, and it was validated with experimental results on hydrogel and cartilage tissues. An anisotropic multiphysics model was developed based on the continuum mixture theory and employed to characterize the nonlinear couplings among anisotropic and large solid deformation,

anisotropic transport of interstitial water and solutes, and the electro-osmotic effect in the disc. Numerical simulations demonstrated that this model is capable of systematically predicting the mechanical and electrochemical signals within the disc under various loading conditions. This anisotropic multiphysics model was then further developed by incorporating a continuum damage model to investigate the initiation and propagation of damage in the annulus fibrosus (AF). The simulated results showed that damages initiate in different regions under compression, flexion, and compression-flexion. The posterior AF was shown to be more susceptible to structure failures as it may be damaged under all three loading conditions with sufficient high magnitudes.

A cell volume dependent glycosaminoglycan (GAG) synthesis mathematical model was developed to quantitatively describe the response of cell biosynthetic behaviors to extracellular mechanical stimuli. It was found that our proposed mathematical model is able to describe the change of GAG synthesis rate in isolated cells and in cartilage with variations of the osmotic loading or mechanical loading. Then, a multiscale mathematical model was developed based on the cell volume dependent GAG synthesis model and biphasic theory to quantify the effect of mechanical loading on GAG synthesis. This multiscale mathematical model was shown to be capable of predicting the effect of static load (creep load) on GAG synthesis in bovine tail discs. This model was also used to investigate the effect of static and diurnal loads on GAG synthesis.

These models developed in this dissertation provide numerical approaches to quantify the abnormal mechanical loading which may cause disc degeneration. These mathematical

models are important in understanding the etiology of disc degeneration, as well as in preventing and treating disc degeneration. These models are also important in designing scaffolds and optimizing loading conditions to grow engineered disc tissues.

Acknowledgements

At this point, I would like to take the opportunity to acknowledge numerous people for their support and encouragement over the past years in different ways and at different times.

First and foremost, I want to express my deepest gratitude to my advisor, Dr. Weiyong Gu, whose thoughtful insights, patient guidance, and constant encouragement helped me to shape and develop this dissertation. I thank Dr. Gu for offering me this opportunity to transit from a civil engineer to a bioengineer. Throughout my graduate studies, he encouraged and trained me to be an independent researcher, and he talked to me like a friend both on research and on life.

I would like to thank Dr. Chun-Yuh Huang, Dr. Qingda Yang, and Dr. Landon R. Grace for kindly serving on my dissertation committee board. I greatly appreciate the time you have spent and the advice you have provided in helping me achieve this work.

I would like to thank all the members of the Tissue Biomechanics Lab and the Mechanobiology Lab, I thank you for your support and friendship. You have made my research and life here wonderful and fulfilling. I would like to thank many friends in the Department of Mechanical and Aerospace Engineering, for kindly providing support on my research and my teaching assistant job.

I will always be thankful to my dear family. I wish to express my deep love and appreciation to my grandparents, my parents, my older brother, and my sister-in-law, for your limitless and unconditional love and support. Although we are separated by the ocean, you are always there when I need you. Last but not least, I want to express my deepest gratitude to my beloved Qiaoqiao Zhu who always stand aside me in these years and makes me who I am. We shared the happiness and struggled the harshness hand-in-hand. No words can express how grateful I am for your love, encouragement, endurance, and sacrifice. I always feel I am the luckiest one to meet you and fall in love with you.

Table of Contents

List of Figures

List of Tables

Chapter 1

Introduction

1.1 Motivation, Specific Aims, and Significances

Degeneration of intervertebral discs (IVDs) is a significant socio-economic concern, affecting millions of people in the United States each year. During degeneration, the disc undergoes a cascade of biological, chemical, electrical and mechanical changes, including the loss of cellularity and activities, the reduction of proteoglycan (PG) and water contents, the decrease in disc volume, and resultantly the failure in tissue-level structure and functions. Abnormal mechanical loading is thought as one of the primary causes of disc degeneration. Abnormal mechanical loading has been suggested to initiate disc degeneration through two pathways. It may directly cause the failure of disc structure, such as rupture of the cartilaginous endplate (CEP) and/or fissure in the annulus fibrosus (AF). The other pathway is through cell-mediated remodeling in response to the mechanical stimuli. The balance between cellular anabolic and catabolic activities is disturbed under abnormal mechanical loading, and resultantly causing degenerative changes in the disc. The cell-mediated remodeling pathway appears to be the main pathway that abnormal mechanical loading initiates disc degeneration.

Although many experiments at multi-levels (from molecular to tissue levels) and interdisciplinary (biochemical and biomechanical) studies have been conducted to understand the effect of abnormal mechanical loading on disc degeneration, it is still very challenging to systematically compile and analyze these experimental results and findings to quantify these effects on the multi-physical behaviors of the disc, let alone to reveal the mechanism of disc degeneration, to diagnose early disc degeneration, or to develop optimal treatment strategies for disc degeneration. This is mainly due to the couplings among the biological, chemical, electrical, and mechanical behaviors within the disc. The objectives of this dissertation are to develop mathematical models to characterize the biomechanics and mechanobiology of discs in order to quantify the abnormal mechanical loading and delineate how the cells perceive and respond to mechanical stimuli. More specifically, this goal will be accomplished with the following specific aims:

Specific Aim #1: To develop biomechanical models to characterize disc mechanical behaviors. A new hydration dependent aggregate modulus model will be developed for soft and hydrated tissues. An anisotropic multiphysics model will be developed and validated for discs. Then, this anisotropic multiphysics model will be employed to quantify the mechanical loading that may initiate damages in the annulus fibrosus by incorporating a continuum damage model.

Specific Aim #2: To develop mechanobiological models to characterize the responses of cellular biosynthetic behaviors to mechanical stimuli. This model will be employed

to analyze the biosynthetic responses of isolated cells and cells embedded within the disc tissue to mechanical stimuli.

With the development of the biomechanical and mechanobiological models, if validated, they can be widely used for basic research and clinical application. Firstly, these models can be used to systematically and quantitatively analyze the existing multi-level and interdisciplinary experimental results to understand the mechanism of disc degeneration caused by abnormal mechanical loading. This application could help to reduce the amount of new experimental studies by: 1) digging new results from the past experiments; 2) designing new experiments with optimized parameters. Secondly, these models can be used to help prevent disc degeneration by quantifying the abnormal mechanical loading that may cause disc degeneration. Thirdly, these models can be used to predict the development of degeneration process and treatment outcomes, which could be helpful in choosing the treatment timing and treatment approaches. Fourthly, these models are also important in designing scaffolds and optimizing loading conditions to grow engineered disc tissues.

1.2 Outline of This Dissertation

After this introductory **Chapter 1**, seven more chapters are presented to achieve the goal of this dissertation:

In **Chapter 2**, a background of the IVD and its structure, composition, biomechanics, mechanobiology, and degeneration is given. A review of biomechanics and mechanobiology mathematical models of the IVD is also presented.

In **Chapter 3**, hydration-dependent constitutive models for the mechanical properties of soft tissue and hydrogels are developed and verified for soft and hydrated tissues. The development and validation of such models are presented in this chapter. Moreover, the limitations and the potential applications of such models are discussed.

In **Chapter 4**, an anisotropic multiphysics model for IVDs is developed based on the continuum mixture theory to characterize the couplings among anisotropic and large solid deformation, anisotropic transport of interstitial water and solutes, and electro-osmotic effect in the IVD. The validation of this model with experimental results is presented.

In **Chapter 5**, a computational model is developed to investigate the initiation and propagation of damage in the AF. The computational model is based on the anisotropic multiphysics model developed in Chapter 4 and a continuum damage model. The initiation and propagation of damage in the AF under compression, flexion, and compression-flexion are simulated.

In **Chapter 6**, a mechanobiology mathematical model to quantitatively describe the cell volume dependent GAG synthesis rate in the cartilaginous tissues is developed. This model is validated with experimental results and shown to be able to describe the change of GAG synthesis rate in isolated cells or in the cartilage with variations of the osmotic loading or mechanical loading.

In Chapter 7, a multiscale mathematical model is developed to quantify GAG synthesis rate in the discs under mechanical loading. This multiscale model is validated with experimental results. This model is also applied to investigate the effect of static and diurnal loads on GAG synthesis.

In **Chapter 8**, a summary is given to reflect the presented important findings and contribution, and recommendations for further work are given to show the potential applications of proposed biomechanical and mechanobiological models.

Chapter 2

Background

2.1 Structure and Composition of the Intervertebral Disc

The intervertebral disc (IVD) is a soft, hydrated, and avascular tissue lying between two adjacent vertebrae in the spinal column. There are 23 IVDs in the human spine (6 in the cervical region, 12 in the thoracic region, and 5 in the lumbar region), and they occupy about one-third of the spinal column height, see Figure 2-1 (a). The lumbar IVD is about 7-10 mm in thickness and 40 mm in diameter (anterior-posterior plane) (Urban and Roberts, 2003).

Each IVD comprises a central gelatinous core, i.e., the nucleus pulposus (NP), a surrounding fiber-reinforced lamellar ring, i.e., the annulus fibrosus (AF), and two thin cartilaginous endplates (CEPs) which connect the NP and AF with the superior and inferior vertebral bodies, see Figure 2-1 (b). The structure and composition of each component are distinct, indicating a unique mechanical role for each.

The NP is highly gelatinous, and it composed of randomly oriented collagen fibers embedded in a water-proteoglycan (PG) gel. Water is the major component of the NP, making up 75-90% of the wet weight of NP. The content of PG is about 40% of the dry

weight of NP, and the type of the PG is predominated by aggrecan. Collagen, primarily type II, makes up about 25% of the dry weight of NP (Adams and Muir, 1976; Antoniou et al., 1996).

The AF structure is comprised of a series (15-25 layers) of concentric lamellae, see Figure 2-1 (c). Structure and composition of the AF continuously vary in the radial direction. The thickness of the lamella decreases from the innermost layer to the outmost layer (from about 0.4 mm to about 0.1 mm). Each lamella consists of a series of parallel fiber bundles, but the orientation is alternative in the adjacent lamellae (Cassidy et al., 1989; Marchand and Ahmed, 1990). The AF is also mostly composed of water which makes up 65% to 80 % of the wet weight of AF. The solid matrix consists of mainly collagen (40% to 90 % of the dry weight of AF), PG (10% to 35 % of the dry weight of AF), and other proteins (5% to 40% of the dry weight of AF) (Antoniou et al., 1996). The contents of type I and type II collagens in the AF change gradually and inversely in the radial direction, with type I collagen content increasing from inner AF to outer AF (Eyre and Muir, 1976). The contents of water and PG have the similar distribution across the AF, with higher content in the inner AF (Antoniou et al., 1996).

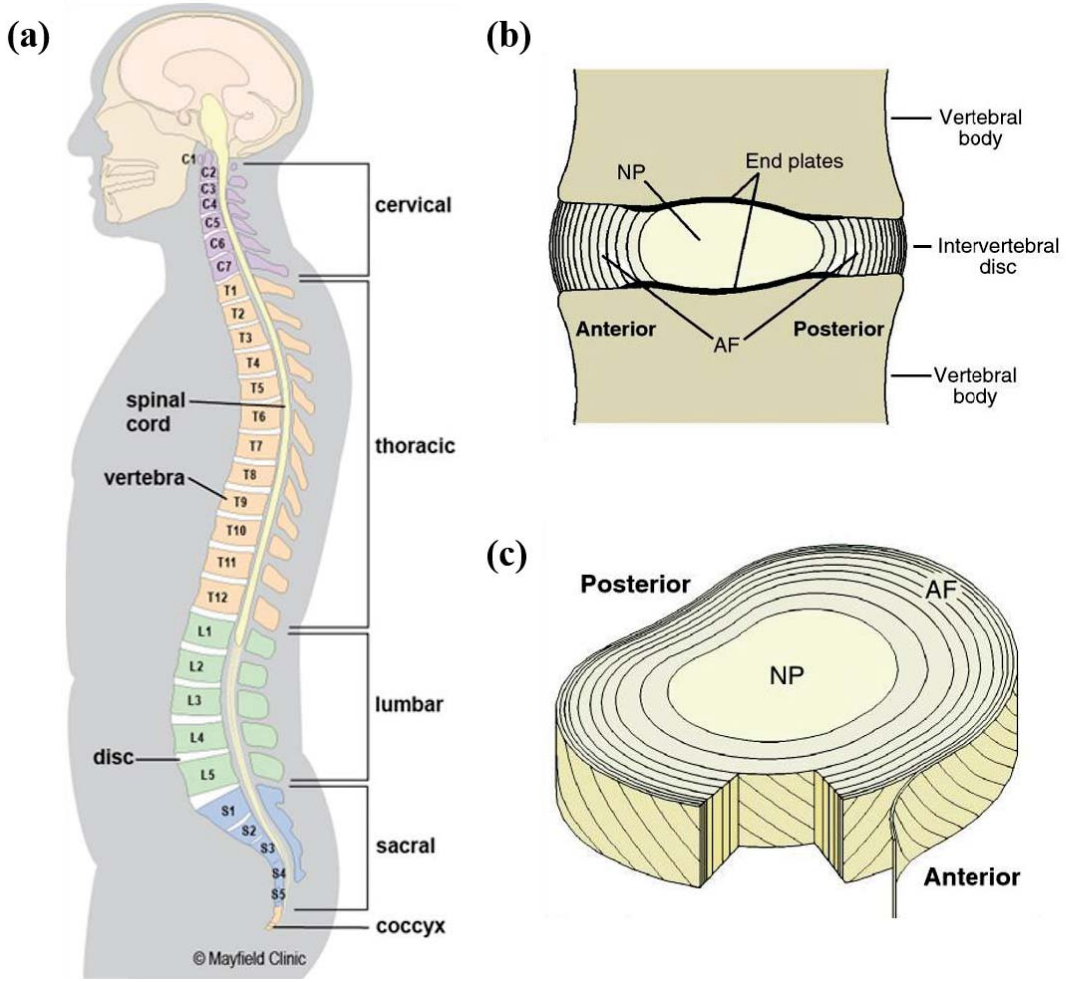

Figure 2-1 (a) Schematic of the human spine, adopted from www.mayfieldclinic.com; (b) Schematic of IVD structure; (c) Schematic of AF lamellar structure; adopted from (Smith et al., 2011).

The CEP is a thin (about 0.6 mm) horizontal layer of hyaline cartilage (Roberts et al., 1989). The CEP is also composed of water (about 60% of the wet weight of CEP), collagen (60% to 80% of the dry weight of CEP), and PG (about 20% of the dry weight of CEP) (Roberts et al., 1989; Setton et al., 1993). The composition and thickness are heterogeneous, with higher water and PG contents and thinner thickness in the central region than those in the peripheral region (Moon et al., 2013; Roberts et al., 1989).

2.2 Biomechanics of the Intervertebral Disc

The disc tissue is a mixture of water, PG, collagen, and other proteins. The network of collagen, together with the trapped PG, forms the porous solid matrix. The structure of PG is like a bottlebrush, which consists of a central protein core with glycosaminoglycan (GAG) side chains, see Figures 2-2. Chondroitin-6-sulfate (CS) and keratan sulfate (KS) are the primary GAGs in the disc (Rosenberg and Schubert, 1967), and they contain charged acidic groups (SO_3^- and COO^-), see Figure 2-2 (c). The negatively charged groups are fixed to the solid matrix, and their density is defined as the fixed charge density (FCD). They attract counter-ions, such as Na^+, to maintain the tissue in the electro-neutrality condition. Thus, the osmolarity in the tissue is higher than that in the ambient environment. This imbalance of ion concentrations across the disc leads to an electro-osmotic effect that imbibes water into the porous solid matrix and causes the tissue to swell. The driving force for water movement is the gradient of water chemical potential. At the equilibrium state, the difference of fluid pressure between the inside of disc and the ambient environment is called Donnan osmotic pressure or swelling pressure (Donnan, 1924).

The NP has a high GAG content, thus has a high swelling pressure and water content due to the electro-osmotic effect, which makes the NP possesses both solid and fluid mechanical characteristics (Iatridis et al., 1996). Thus, the NP can be represented as a biphasic material which usually is characterized by elastic moduli and hydraulic permeability (Mow et al., 1980). Confined or unconfined compression tests are widely used to measure the biphasic material properties of NP (Heneghan and Riches, 2008; Johannessen and Elliott, 2005; Perie et al., 2005). The viscoelastic feature of NP is due not only to the interaction between the solid matrix and interstitial water but also to the intrinsic viscoelasticity of the solid matrix (Iatridis et al., 1997b).

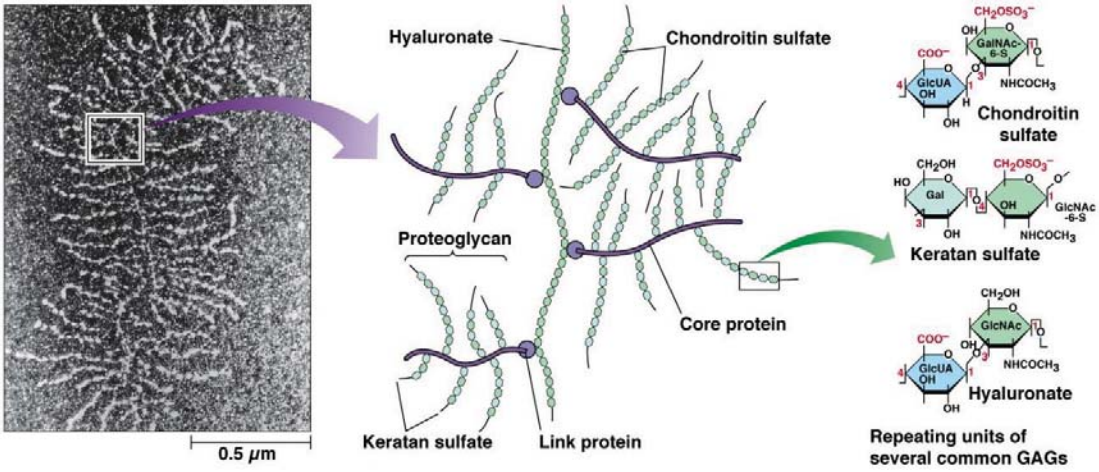

Figure 2-2 Diagram of PG structure and GAG structure, adopted from (Hardin et al., 2011)

The AF also contains GAG, but its content is less than that in the NP (Antoniou et al., 1996), thus the electro-osmotic effect is lower than that in the NP. The GAG, along with type II collagen and other proteins, makes up the ground matrix of the AF. This ground

matrix also possesses both solid and fluid mechanical characteristics, and thus can be represented as a biphasic material. The obliquely oriented collagen fiber bundles are embedded in the ground matrix, which provide the tensile strength to the AF. The tensile properties of AF have been found to be nonlinear, heterogeneous, anisotropic, and viscoelastic with uniaxial and biaxial tension tests (Ebara et al., 1996; Galante, 1967; O'Connell et al., 2012). The tensile properties also have been found to vary from the outer AF to inner AF, and from anterior AF to posterior AF due to the variation of collagen content, the ratio between type I and type II collagen contents, and the orientation of the fiber bundles (Eyre and Muir, 1976; Holzapfel et al., 2005; Skaggs et al., 1994).

The CEP can also be characterized as a biphasic material according to its composition. Experimental studies of its biomechanical properties are far less than those of NP and AF. But, interestingly, the hydraulic permeability of CEP has been found to depend on the flow directions, which may be important in maintaining the water content in the disc (Ayotte et al., 2000; Ayotte et al., 2001).

The biomechanical function of the disc is to transmit axial load, resist shear load, absorb shock, and to provide flexibility to the spine. The disc achieves these mechanical functions through its unique tissue composition and structure. The swelling tendency of NP is restrained by the AF and CEPs, whereas water and electrolytes can inflow and outflow through AF and CEPs. Thus, the interactions of multiphasic components (solid, fluid, and ions) cause the coupling of multi-physical (mechanical, electrical, and chemical) behaviors, which gives the disc its unique mechanical functions.

2.3 Mechanobiology of the Intervertebral Disc

Mechanical loading on the disc generates a complex extracellular environment, including high level of stresses and strains arising from the deformation of extracellular matrix, high magnitude of hydrostatic pressure, shear stress caused by interstitial fluid flow, electrokinetic effects caused by the interactions among fixed charge groups and mobile charged ions, and others (Setton and Chen, 2006), see Figure 2-3. All these extracellular environment factors can be varied by mechanical loading. Extensive in vivo and/or in vitro experiments have been conducted to study the effects of mechanical stimuli on the biological processes at the cellular, tissue, organ, and organismal level, or, briefly, to study the mechanobiology of IVD (Chan et al., 2011; Setton and Chen, 2006).

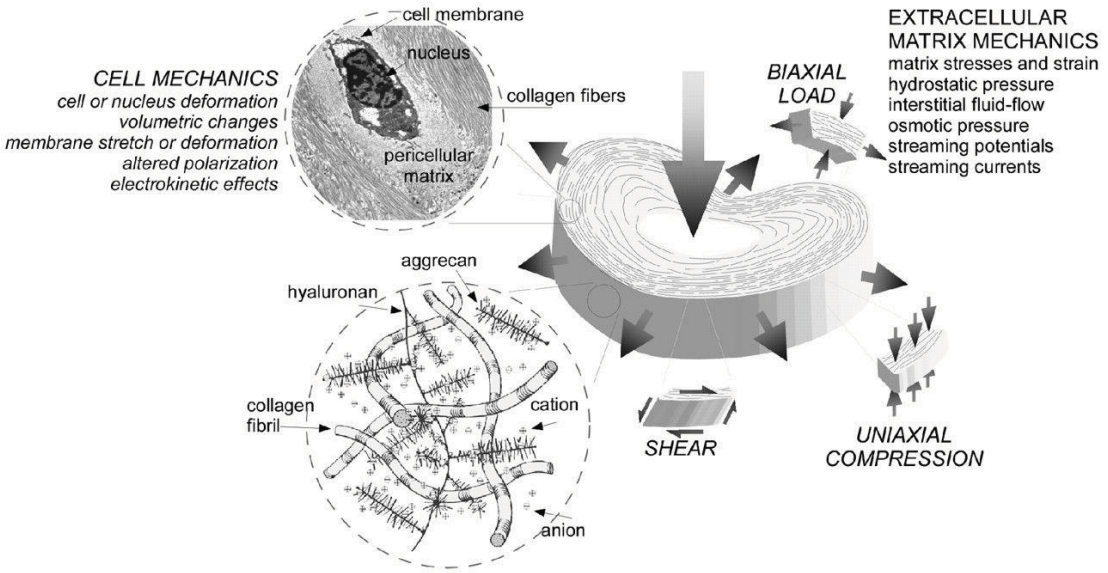

Figure 2-3 Illustration of complex extracellular environment generated by mechanical loading, adopted from (Setton and Chen, 2006).

The effects of static compression on the biological processes within the disc tissue have been shown to depend on the magnitude of the loading and the anatomic regions, which

have been reviewed in details in literature (Setton and Chen, 2004). For example, Ohshima et al experimentally studied the effects of static compression (0.5kg-15kg) on the synthesis of GAG and collagen (represented by the incorporation of ^{35}S-sulphate and ^{3}H-prolin, respectively) within the bovine tail discs (Ohshima et al., 1995). They found that the synthesis rates in the NP and inner AF are highest under a 5-10 kg load.

The effects of dynamical loading on the biological processes within the disc tissue have been shown to depend on the magnitude, amplitude, frequency, duration of the loading, as well as on the anatomic regions, which have been reviewed in details by Chan et al (Chan et al., 2011). For example, Maclean et al investigated the metabolic response of rat disc cells to dynamic loading with different magnitudes and frequencies (Maclean et al., 2004). They found that in the NP with the load magnitude of 1 MPa the anabolic genes are stimulated at 0.01 Hz and catabolic genes are stimulated at 1 Hz, whereas dynamical loading at all frequencies (0.01, 0.2, 1 Hz) at 1 MPa significantly stimulate the catabolic mRNA.

The effects of osmotic pressure on metabolic activities of disc cells have attracted a lot of research efforts because the osmolarity in the disc is higher than that in other tissues (Johnson et al., 2014). Ishihara et al experimentally investigated the biosynthetic responses of bovine NP cells to variations of osmolarity in the culture medium by adding NaCl or sucrose (Ishihara et al., 1997). They found that the cells exhibit the maximum GAG synthesis rate at osmolarity in the medium close to the in vivo value (about 430 mOsm), regardless of the type of osmolyte, and at osmolarity larger or smaller than the in vivo value,

the GAG synthesis rate drops significantly. Some other researchers also found that the cells in the NP explant exhibit a higher synthesis rate of GAG when the osmolarity in the medium is raised (using polyethylene glycol) close to the in vivo value (van Dijk et al., 2011; van Dijk et al., 2013).

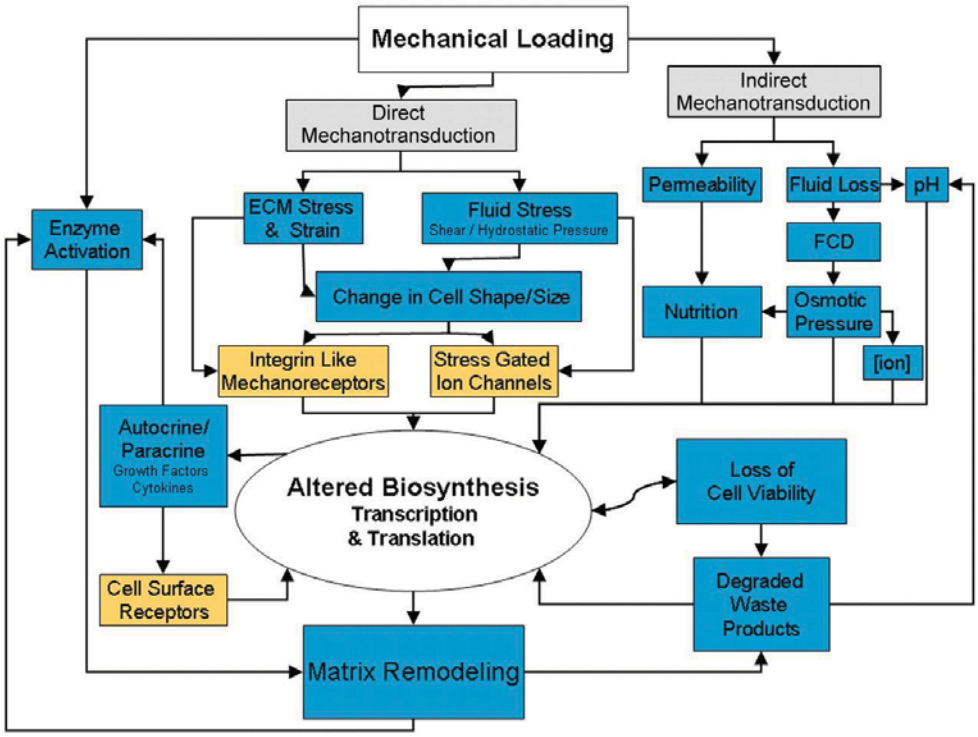

Figure 2-4 Flow chart of the direct and indirect extracellular mechanotransduction pathways, adopted from (Iatridis et al., 2006).

Upon the brief review of experimental findings on the mechanobiology of discs, the biosynthetic responses of disc cells to external mechanical stimuli seem to be very complicated. The mechanical stimuli may directly regulate cell shape and size, and hence, regulate cell activities and viability. For example, stretch (e.g., a 5% elongation or 15% area change) of rabbit AF cells could enhance the production of nitric oxide, inhibit the synthesis of PG, and increase cell apoptosis (Rannou et al., 2003; Rannou et al., 2004). The mechanical stimuli may also affect cell activities and viability indirectly, via altering the

localized nutrient concentration, pH, osmolarity, and other regulators (Iatridis et al., 2006), see Figure 2-4. For example, the concentration of glucose has been found to be the primary factor governing the cell viability (Bibby and Urban, 2004) and the concentration is affected by mechanical loading (Zhu et al., 2012). Thus, mechanical loading can either directly or indirectly affect cell activities and viability and eventually results in the remodeling of extracellular matrix (Setton and Chen, 2006; Stokes and Iatridis, 2004).

2.4 Degeneration of the Intervertebral Disc

2.4.1 Low Back Pain

Low back pain is a prevalent healthy problem, with more than 600 million people affected globally (Hoy et al., 2012; Hoy et al., 2014). It is the leading cause of years lived with disability for several decades (Vos et al., 2012). It causes enormous financial burdens on both the patient and their families, and the whole society as well. For example, the annual cost of low back pain was estimated to be ranging from $100 to $200 billion, including both direct cost and indirect cost such as loss of wages, or reduced productivity, in the United States alone (Katz, 2006). Low back pain is more prevalent in men than that in women (Hoy et al., 2014). It is also more prevalent in elder people, such as in those aged 40 years old or older (Hoy et al., 2012; Hoy et al., 2014).

The cause of low back pain is still not definitive yet, but the degeneration of IVD is thought to play an important role in it (Buckwalter, 1995; Freemont, 2009; Luoma et al., 2000).

2.4.2 Degenerated Intervertebral Discs

Degeneration of IVDs occurs much earlier than that in other musculoskeletal tissue, it encompasses a broad set of changes in disc morphology, biochemical composition, and disc function (Boos et al., 1993; Miller et al., 1988; Urban and Roberts, 2003). During disc degeneration, the boundary between AF and NP becomes less distinctive as the NP becomes less gel-like and more fibrotic. The lamellae in the AF become irregular (e.g., bulging inward and/or radial fissure), and the collagen and elastin networks also become disorganized, see Figure 2-5. Consequently, cleft and fissures occur frequently in degenerated discs, leading to the ingrowth of nerves and blood vessels into tissues (Urban and Roberts, 2003).

The most significant biochemical change during disc degeneration is the loss of PG content (Urban and Roberts, 2003). Osmotic pressure and hydration in the disc decrease with the loss of PG content, which leads to the compromise of disc mechanical functions in supporting axial compression, absorbing shocks, and providing flexibility to the spinal system. While the loss of another major component, collagen, is not as obvious as the loss of PG because the turnover time for collagen is over 100 years which is much longer than the turnover time (about 20 years) for PG (Adams and Roughley, 2006).

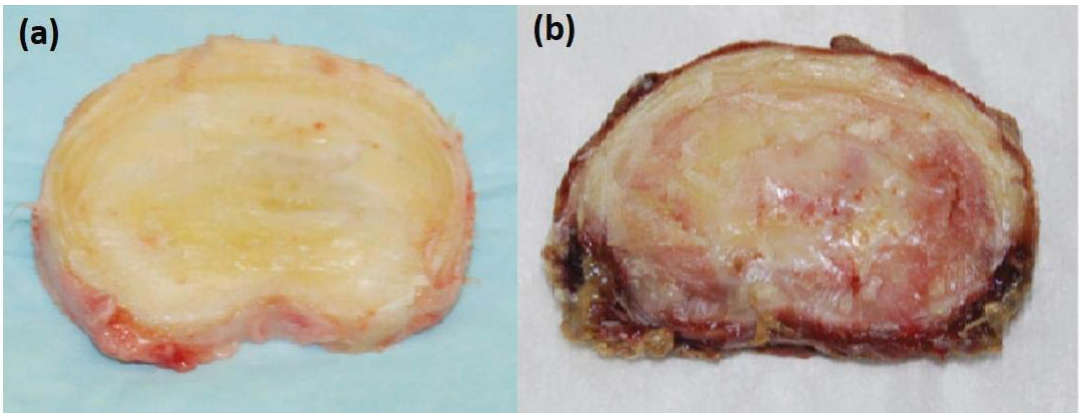

Figure 2-5 Photographs of (a) a non-degenerated disc and (b) a degenerated disc, adopted from (Jackson, 2010).

Degeneration of the disc affects its mechanical properties. The viscoelastic shear properties of human NP are found to undergo alterations with disc degeneration. The instantaneous and dynamic shear moduli increase with degeneration, whereas the phase shift angle decreases with degeneration. The NP transforms from a "fluid-like" material to a more "solid-like" material with disc degeneration (Iatridis et al., 1997a). The biphasic material properties of human NP are also found to change with disc degeneration. The effective aggregate modulus of NP decreases with disc degeneration while the hydraulic permeability increases with disc degeneration (Johannessen and Elliott, 2005). Degeneration of the disc also affects the mechanical properties of AF. The dynamic modulus of AF increases with disc degeneration, whereas the phase angle does not change (Sen et al., 2012). The elastic properties, such as Poisson's ratio, failure stress, and strain energy density, of AF are strongly influenced by disc degeneration (Acaroglu et al., 1995). The elastic modulus at the toe-region in the nonlinear tensile stress-stretch curve of AF has a two-fold increase with degeneration (Guerin and Elliott, 2006; O'Connell et al., 2009). The elastic anisotropy and anatomic region-dependent tensile properties of human AF

remain unchanged during disc degeneration (Acaroglu et al., 1995; Skaggs et al., 1994). The anisotropic hydraulic permeability of non-degenerated AF tends to be isotropic with disc degeneration, with increases in the axial and circumferential directions and a decrease in the radial direction (Gu et al., 1999). The aggregate modulus of CEP from moderately degenerated human discs is slightly lower than that from non-degenerated human discs (DeLucca et al., 2016). The hydraulic permeability is found to decrease by about 50-60% with degeneration with a confined stress-relaxation test (DeLucca et al., 2016), but it is found to increase with degeneration with a permeation test (Rodriguez et al., 2011).

2.4.3 Etiology of Disc Degeneration

The cause of disc degeneration is still not clear yet, but it is generally thought that genetic factors, poor nutrient supply, and abnormal mechanical loading are three primary factors that can cause disc degeneration (Urban and Roberts, 2003), see Figure 2-6.

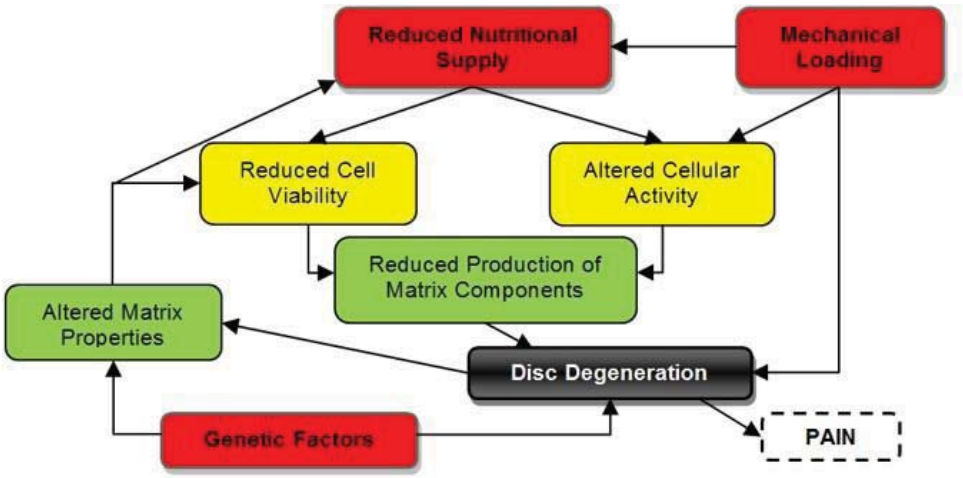

Figure 2-6 Schematic showing possible causes and pathways related to disc degeneration.

Genetic factors. Several studies on human twins have shown that genetic predisposition plays an important role in disc degeneration (Heikkila et al., 1989; Matsui et al., 1998; Varlotta et al., 1991). Heritability is found to exceed 60% in a study with 326 twins (Sambrook et al., 1999). The mutations in genes of matrix components have been found to associate with disc degeneration in a Finnish population and a Japanese population (Annunen et al., 1999; Kawaguchi et al., 1999; Paassilta et al., 2001). Polymorphisms in the promoter region of the MMP-3 gene and vitamin D receptor gene also have been found to associate with disc degeneration (Kawaguchi et al., 2002; Takahashi et al., 2001).

Poor nutrient supply. The disc is the largest avascular tissue, and thus the disc cells rely on diffusion of nutrients such as glucose and oxygen from the blood vessels at disc margins to survive (Holm et al., 1981). Nutrients can diffuse into the disc through two pathways: the CEP-NP pathway and the periphery AF pathway (Brodin, 1955; Nachemso.A et al., 1970; Urban et al., 1978). The cells in the NP mainly depend on nutrients supplied from the capillaries above the CEP through the CEP-NP pathway, and the diffusion distance for the nutrients could be as far as 8 mm (Urban and Roberts, 2003; Urban et al., 1978). The cells in the AF mostly rely on nutrients supplied from the blood vessels at the periphery of AF.

The cells cannot survive long with low extracellular glucose level and pH value (Horner and Urban, 2001). The biosynthetic behaviors of cells slow down significantly at a low oxygen level and pH value environment (Ishihara and Urban, 1999; Ohshima and Urban, 1992). Thus, poor nutrient supply could compromise cell viability and activity, thus, the

synthesis of extracellular matrix cannot be maintained to balance the degradation, leading to disc degeneration (Nachemso.A et al., 1970). Many factors, such as atherosclerosis, sickle cell anemia, and cigarette smoking, have been found to affect the nutrients supply at disc margins (Jackson et al., 2015; Kauppila et al., 1997; Urban and Roberts, 2003). Poor nutrient supply also could be due to the calcification of CEP, in which the pores in CEP could be blocked (Roberts et al., 1996).

Abnormal mechanical loading. Abnormal mechanical loading may initiate the disc degeneration through causing damage to the disc structure, such as the rupture of CEP and/or the fissure of AF (Adams et al., 2000; Allan and Waddell, 1989; Urban and Roberts, 2003). This pathway to initiate degeneration is supported by many epidemiological studies which have found an association between disc degeneration and disorder with obesity, heavy physical work, lifting, and truck-driving (Deyo and Bass, 1989; Heliovaara, 1989; Pope et al., 2002). This pathway is also supported by animal model studies which have shown that surgical tear of AF or CEP could cause subsequent degenerative changes in the NP (Holm et al., 2004; Melrose et al., 1992; Osti et al., 1990). Though damage in disc structure is a potential cause of disc degeneration, this process may take many years to be apparent (Hassett et al., 2003; Kerttula et al., 2000b).

Abnormal mechanical loading may also initiate disc degeneration through cell-mediated remodeling in response to the mechanical stimuli, and this pathway appears to be the main pathway through which abnormal mechanical loading initiates disc degeneration (Setton and Chen, 2006). Cell-mediated remodeling could be due to the change of cellular

metabolism activity, and could also be due to cell apoptosis (Iatridis et al., 2006). As shown in Section 2.3, the disc cells exhibit different anabolic and catabolic responses to the mechanical stimuli, depending on the loading type, magnitude, duration, frequency, as well as the anatomic region of cell origin (Setton and Chen, 2004). It has been summarized that, in general, mechanical loading with low to moderate magnitude promotes anabolic response of cells, whereas loading with higher magnitudes increases the catabolic response of cells. For example, expression of genes related to the production of matrix component (collagen and aggrecan) is higher at low frequency of compressive loading (e.g., 1 MPa at 0.01 Hz), whereas the mRNA expression of proteases (MMP-3 and MMP-13) is more active at higher frequency of compressive loading (e.g., 1 MPa at 1 Hz) (Maclean et al., 2004; Walsh and Lotz, 2004). There is a homeostasis state in which the catabolic and anabolic responses are balanced. Disturbance tilting the balance between matrix synthesis and degradation could initiate degenerative changes in the disc (Iatridis et al., 2006; Lotz et al., 2002; Setton and Chen, 2006). Dynamic loading has been found to increase the transport of nutrients into the disc helping keep normal cell population to be alive and functional to maintain the synthesis of matrix components (Zhu et al., 2012).

2.5 Mathematical Models for the Intervertebral Disc

2.5.1 Biomechanical Models

Many biomechanical models have been developed to study the biomechanical behavior of IVDs [cf. (Schmidt et al., 2013) and the references therein]. These models may be classified into three types, the single-phase model [e.g., (Belytschko et al., 1974; Eberlein et al., 2001; Schmidt et al., 2007)], the biphasic/biphasic-swelling model [e.g., (Argoubi and ShiraziAdl,

1996; Ehlers et al., 2009; Jacobs et al., 2014; Karajan, 2012; Laible et al., 1993; Schroeder et al., 2010)], and the multiphasic mechano-electrochemical model (Iatridis et al., 2003; Sun and Leong, 2004; Yao and Gu, 2006). The single-phase model treats the NP as an ideal fluid and the AF as a solid, which cannot characterize the interstitial fluid flow in the AF and swelling pressure (Belytschko et al., 1974). The biphasic model describes the disc as a mixture of fluid and solid (Mow et al., 1980). The biphasic model is able to characterize the interstitial fluid flow and hence, the flow caused time-dependent viscoelastic behavior of the disc. However, the electro-osmotic effect is not accounted for in the biphasic model. A shortcut is to add the swelling pressure term to the total mixture stress based on the Lanir's assumption that the electro-osmotic equilibrium in the tissue is achieved instantaneously (Lanir, 1987). This approach is called biphasic-swelling model and it has been used as an approximation to include the electro-osmotic effect (Wilson et al., 2005). The diffusivity of ions in this type of model is assumed to be infinitely large, which is not physiologically relevant. Thus, a more realistic multiphasic model is developed for the disc (Yao and Gu, 2006) based on the mechano-electrochemical continuum triphasic theory (Lai et al., 1991). In this model, the solid, fluid, and solutes (e.g., ions) are modeled as separated phases, so all the mechano-electrochemical phenomena in the tissue can be described. In this model, the solid matrix is treated as an isotropic material and undergoes small deformation, and the transport of fluid and ions are assumed to be isotropic.

Though many models have been developed for characterizing the biomechanical behavior of IVDs, it is still challenging to quantitatively describe the behavior of the disc under various loading conditions. The major challenge arises from the complicated couplings of

multiple physical fields in the IVD and the anisotropic behavior of the AF. Moreover, the fiber bundles in the AF give the AF not only anisotropic mechanical properties but also anisotropic transport properties (Elliott and Setton, 2001; Gu et al., 1999; Iatridis et al., 1998; Jackson et al., 2012).

Theoretical and/or numerical models also have been used to investigate the deformation of cells embedded in the extracellular matrix. Baer et al and Cao et al studied the micromechanical environment around the disc cells and the deformation behaviors of the cells using biphasic finite element method (Baer et al., 2003; Baer and Setton, 2000; Cao et al., 2007, 2011). They found that the micromechanical environment varies dramatically with the anatomic region, and is also influenced by the geometry of cells. The volumetric strain of NP cell is found to be 1.9-3.7 times greater than that of the extracellular matrix, and this ratio is found to be 3.1-3.8 for AF cells (Cao et al., 2007, 2011).

2.5.2 Mechanobiological Models

Current mathematical models on the mechanobiology of the IVD mainly focus on the indirect mechanotransduction mechanism. Shirazi-Adl et al are the first to propose a theoretical model to describe the coupling of cell viability and nutrition level in IVD (Shirazi-Adl et al., 2010). In this model, the cell density was assumed to vary instantaneously with glucose concentration. However, this model is unrealistic, as the model would predict the resurrection of dead cells when the glucose level recovers after falling below certain critical level for cell survival (e.g., 0.5 mM). Later, Zhu et al proposed a more sophisticated glucose concentration dependent cell viability model (Zhu et al.,

2012). Recently, Gu et al further coupled the biosynthesis/turnover of GAG in their model, and this model has successfully simulated the long-term (over 50 years) degeneration process (Gu et al., 2014). Moreover, this model also has been used to predict the outcome of several biological treatment strategies (Zhu et al., 2016).

The mechanism of mechanotransduction also has been studied with semi-numerical approaches. Lotz et al. experimentally evaluated the spatial variation of histologic and biologic data of IVD under mechanical loading, and then correlated them with the spatial mechanical signals (e.g., strain and hydrostatic pressure) calculated with finite element method to find the potential mechanism of mechanotransduction (Lotz et al., 1998; Lotz et al., 2002). They suggested that the mechanical loading applied on the IVD is “filtered” into spatial patterns of fluid pressure and matrix stress to affect cell metabolic activities (Lotz et al., 2002).

Chapter 3

Constitutive Models for Hydration-dependent Mechanical Properties of Biological Soft Tissues and Hydrogels

3.1 Introductory Remarks

The mechanical and transport properties of biological soft tissues and hydrogels play an important role in governing the extracellular environment (e.g., stress, strain, and nutrition distributions) in such materials as discussed in Section 2.3, and the knowledge of these properties are important for understanding tissue growth and degeneration, or designing scaffolds with hydrogels for tissue engineering applications.

It has been reported that the effective mechanical properties of the porous materials are dependent on the composition of the solid matrix and the deformation (Armstrong and Mow, 1982; Best et al., 1994; Hu et al., 2012; Li et al., 2003; Watase and Nishinari, 1983). Armstrong and Mow found a strong correlation between the equilibrium modulus and

water content in cartilage tissues. Their results showed that the equilibrium modulus increases with the decrease in water content (Armstrong and Mow, 1982). In other soft tissues, such as AF and cornea, this correlation has also been found (Hatami-Marbini and Etebu, 2013; Klisch and Lotz, 2000). The dependence of mechanical properties on water content has been reported in agarose gels as well (Gu et al., 2003; Normand et al., 2000). The mechanical properties of both soft tissues and hydrogels also are shown to depend on the deformation (Chahine et al., 2004; Chen et al., 2001; Stammen et al., 2001). This may be partially due to the change of water content caused by deformation (Lai et al., 1991; Mow et al., 1980). It may be also due to the intrinsic nonlinear mechanical behaviors of these materials (Iatridis et al., 1998).

It has been found experimentally that the mechanical properties of these materials are correlated with their transport properties (Aoki et al., 2012; Evans and Quinn, 2005), since both the mechanical and transport properties of porous materials are dependent on material composition and structure (Armstrong and Mow, 1982; Best et al., 1994; Hu et al., 2012; Julkunen et al., 2008; Mow et al., 1984; Roberts et al., 1996; Williamson et al., 2001). Evans and Quinn showed that an increase in Young's modulus is correlated with the decrease of solute diffusivities in articular cartilage and cartilage-like materials (Evans and Quinn, 2005). The emerging quantitative magnetic resonance imaging (MRI) techniques have been used to probe the transport properties and water content of biological tissues (Chiu et al., 2001; Edelman et al., 1994; Kerttula et al., 2001; Kerttula et al., 2000a; Liess et al., 2002; Xia et al., 1994). However, the noninvasive determination of the mechanical properties of biological tissues is very challenging.

Many constitutive models have been proposed for the hydraulic permeability and solute diffusivity in porous tissues and hydrogels (Clague et al., 2000; Ehlers and Markert, 2001; Gu et al., 2003; Holmes and Mow, 1990; Lai and Mow, 1980). For example, Gu et al. proposed an empirical model for hydraulic permeability in agarose gels. This model works well for cartilage and agarose gels with a wide range of water content (Gu et al., 2003). Many constitutive models have been developed for solute diffusivity in hydrated porous materials as well (Masaro and Zhu, 1999). One of them is the well-known Mackie and Meares' model. In this model, the ratio of solute diffusivity in tissue to that in aqueous solution, i.e., the relative solute diffusivity, is a function of volume fraction of fluid (i.e., hydration) only (Mackie and Meares, 1955). This model was developed for small solutes only because the effect of solute size has not been taken into consideration. Gu et al. proposed a model for the spherical solutes in biological tissues and hydrogels. In this model, the diffusivity is an exponential function of the ratio of the solute size to the square root of intrinsic Darcy permeability of tissue (Gu et al., 2004). This model is able to predict the diffusivity of the molecules in agarose gels and in the porcine AF(Gu et al., 2004).

Theoretical and empirical constitutive models have been developed for porous elastic, hyperelastic, and viscoplastic materials, such as ceramics and elastomeric foam, to study the porosity-dependent mechanical properties (Agoras and Castaneda, 2014; Danielsson et al., 2004; Poutet et al., 1996; Roberts and Garboczi, 2000). However, these models were proposed for the rigid and low porosity materials which may be not capable of predicting the hydration-dependent mechanical properties in biological soft tissues and hydrogels. For

example, Danielsson *et al.* developed a constitutive model for a porous hyperelastic material based on the micromechanics framework. They assumed that the porous material was represented as a thick-walled sphere and the pores were not openly connected with each other (Danielsson et al., 2004). This theoretical model may not be suitable for biological soft tissues or hydrogels since the pores in these materials are openly interconnected.

Therefore, the objective of this chapter is to theoretically develop a new constitutive model for hydration-dependent mechanical properties of biological soft tissues and hydrogels. This study is important for developing a new technique for noninvasively assessing the mechanical properties of biological soft tissues using quantitative imaging methods as well as for designing scaffolds with proper mechanical properties for tissue engineering applications.

3.2 Development of Constitutive Models

A hydrated porous material (such as biological soft tissues and hydrogels) may be modeled as a biphasic mixture consisting of a porous solid phase and an interstitial fluid phase (Mow et al., 1980). Both phases are assumed to be intrinsically incompressible, but the volume of the whole mixture may change due to the fluid flowing in or exuding out of the mixture. Each phase $_{\alpha}$ ($\alpha = s$ for the solid phase and $\alpha = w$ for the fluid phase) has a volume fraction ϕ^{α}, and the mixture is assumed to be saturated (i.e., $\phi^{s} + \phi^{w} = 1$). Therefore, the continuity equation for the mixture reduces to (Ateshian, 2007; Lai et al., 1991; Mow et al., 1980; Nguyen-minh et al., 1998),

$$\nabla \cdot (\phi^w \mathbf{v}^w + \phi^s \mathbf{v}^s) = 0, \tag{3-1}$$

where $\mathbf{v}^\alpha$ is the velocity of phase α . Neglecting the body force and inertia, the conservation of momentum for the mixture at the quasi-static condition states:

$$\nabla \cdot \boldsymbol{\sigma} = \mathbf{0}, \tag{3-2}$$

where $\boldsymbol{\sigma}$ is the Cauchy stress in the mixture. For an isotropic mixture with linear elastic solid phase with infinitesimal deformation, the total stress in the mixture may be written as (Mow et al., 1980),

$$\boldsymbol{\sigma} = -p\mathbf{I} + \lambda(\nabla \cdot \mathbf{u})\mathbf{I} + \mu[\nabla \mathbf{u} + (\nabla \mathbf{u})^T], \tag{3-3}$$

where p is the fluid pressure, λ and μ are the Lamé constants, and $\mathbf{u}$ is the displacement. A fluid volume flux (relative to the solid phase) is defined as $\mathbf{J}^w = \phi^w(\mathbf{v}^w - \mathbf{v}^s)$ and is related to fluid pressure p by Darcy's law:

$$\mathbf{J}^w = -k\nabla p, \tag{3-4}$$

where k is the hydraulic permeability. Using eqs. (3-1), (3-3) and (3-4), together with the saturation assumption, one can derive that,

$$\frac{\partial e}{\partial t} = H_A k \nabla^2 e, \tag{3-5}$$

where $H_A = \lambda + 2\mu$ is the aggregate modulus (Mow et al., 1980), and $e = \nabla \cdot \mathbf{u}$ is the dilatation of the mixture. With the assumption of infinitesimal deformation, the volume fraction of fluid is a linear function of e with $\phi^w = \phi_r^w + (1 - \phi_r^w)e$ (Lai et al., 1991; Nguyen-minh et al., 1998), where ϕ_r^w is the fluid volume fraction at the reference state. Thus, eq. (3-5) can be written (in terms of variable ϕ^w) as,

$$\frac{\partial \phi^w}{\partial t} = D\nabla^2 \phi^w, \tag{3-6}$$

where

$$D = H_A k\,. \tag{3-7}$$

Equations (3-5) and (3-6) are both in the form of diffusion equation. D is the mutual diffusivity of fluid (water) in the biphasic mixture with intrinsically incompressible constituents (see Appendix), and it is also known as the cooperative diffusivity (Tanaka and Fillmore, 1979) or water diffusivity (Hu et al., 2012) in the literature.

For the biphasic materials with intrinsically incompressible solid and fluid phases, the following constraints must be satisfied:

$$\lim_{\phi^w \to 0} k = 0, \lim_{\phi^w \to 0} H_A = +\infty, \lim_{\phi^w \to 0} D = 0\,, \tag{3-8}$$

$$\lim_{\phi^w \to 1} k = +\infty, \lim_{\phi^w \to 1} H_A = 0, \lim_{\phi^w \to 1} D = D_0\,, \tag{3-9}$$

where D_0 is the diffusivity of fluid in the aqueous solution. For example, the value of water self-diffusion coefficient in pure water is 2.3×10^{-9} m^2/s at 25 °C (Holz et al., 2000).

The dependence of hydraulic permeability on water content of biological soft tissues and hydrogels may be expressed as (Gu et al., 2003),

$$k = a\left(\frac{\phi^w}{1-\phi^w}\right)^b, \tag{3-10}$$

where a and b are two material parameters. It has been shown that this model works well for predicting the hydraulic permeability of biological tissues and agarose gels over a wide range of hydration from ~0.7 to ~0.98 (Gu and Yao, 2003; Gu et al., 2003).

In this study, we adopted the Mackie and Meares model (Knauss et al., 1999; Mackie and Meares, 1955) to estimate the water mutual diffusivity, which is given by the following equation:

$$\frac{D}{D_0} = \left(\frac{1-\phi^s}{1+\phi^s}\right)^2 = \left(\frac{\phi^w}{2-\phi^w}\right)^2 . \tag{3-11}$$

Knauss et al. showed that this model could satisfactorily predict the results of water self-diffusion coefficient in cartilage and cartilage components over a wide range of hydration from 0.4 to 0.95 (Knauss et al., 1999). From eqs. (3-7), (3-10), and (3-11), the constitutive model for the hydration-dependent aggregate modulus can be obtained:

$$H_A = A\frac{(1-\phi^w)^b}{(2-\phi^w)^2}(\phi^w)^{2-b}, \tag{3-12}$$

where $A = D_0/a$. Note that eq. (3-12) satisfies the constraints described in eqs. (3-8) and (3-9) when the value of b is greater than 2.

The aggregate modulus is a linear combination of two Lamé constants. In order to explicitly separate the Lamé constants from the aggregate modulus, we adopted the following model for the second Lamé constant (i.e., shear modulus) in the literature (Danielsson et al., 2004):

$$\mu = \mu_0(1-\phi^w), \tag{3-13}$$

where μ_0 is a parameter representing the shear modulus of the solid without pores.

Using the constitutive models for the aggregate modulus and shear modulus, i.e., eqs. (3-12) and (3-13), one can determine the dependence of Poisson's ratio (υ) of the mixture on water content, by

$$\upsilon = \frac{H_A - 2\mu}{2(H_A - \mu)}. \tag{3-14}$$

3.3 Applications of Constitutive Models

In these constitutive relations for k, H_A, and μ, there are three unknown parameters a, b, and μ_0. The values of these parameters can be determined by experiments.

For agarose gels with concentration in the range of 2-14.8% (w/w), and the corresponding water content in the range of 0.98-0.88, the values of material parameters a and b are: $a = 3.39\times10^{-18}$ m^4/(Ns) and $b = 3.236$ (Gu et al., 2003). For this type of materials, the variation of aggregate modulus H_A with the change of water content is presented in Figure 3-1. It is shown that our theoretically calculated aggregate modulus decreases nonlinearly with increasing hydration of the tissue. The experimental data of H_A for agarose gels, obtained from our previous study (Gu et al., 2003), are also plotted in Figure 3-1 for comparison.

Hu et al. characterized the shear modulus of pH-sensitive hydrogels at different swelling conditions using an unconfined stress relaxation test (Hu et al., 2012). Based on the reported swelling ratio [$\theta = (1-\phi^w)^{-1/3}$], the hydration (ϕ^w) of their hydrogels was converted and found to be in the range from 0.94 to 0.88. Least-squared curve-fitting of the shear modulus of hydrogels to the model [i.e., eq. (3-13)] yielded $\mu_0 = 120.65$ kPa (R^2=0.97) and $\mu_0 = 117.53$ kPa (R^2=0.88) for two different compositions of poly (DMAEMA-co-AAm) hydrogels (Figure 3-2). The linear shear model, i.e., eq. (3-13), is verified for highly hydrated soft materials.

The constitutive relationship between the Poisson's ratio and water content [i.e., eq. (3-14)] is shown in Figure 3-2. Various values of the material parameter μ_0 are used to show this hydration-dependent Poisson's ratio. It is shown that the Poisson's ratio approaches to 0.5 as hydration is lower than 0.7. The Poisson's ratio decreases with increasing hydration slightly in the range of 0.7-0.85, and dramatically in the range of 0.85-0.95.

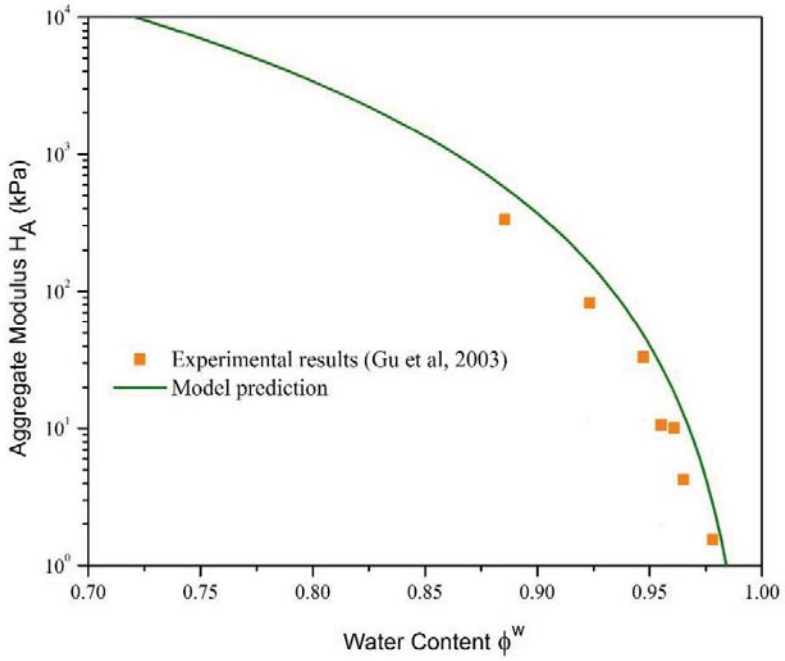

Figure 3-1 Variation of aggregate modulus with water content for agarose gels. The solid line is model prediction [i.e., eq. (3-12)], and the square dots are experimental results from (Gu et al., 2003).

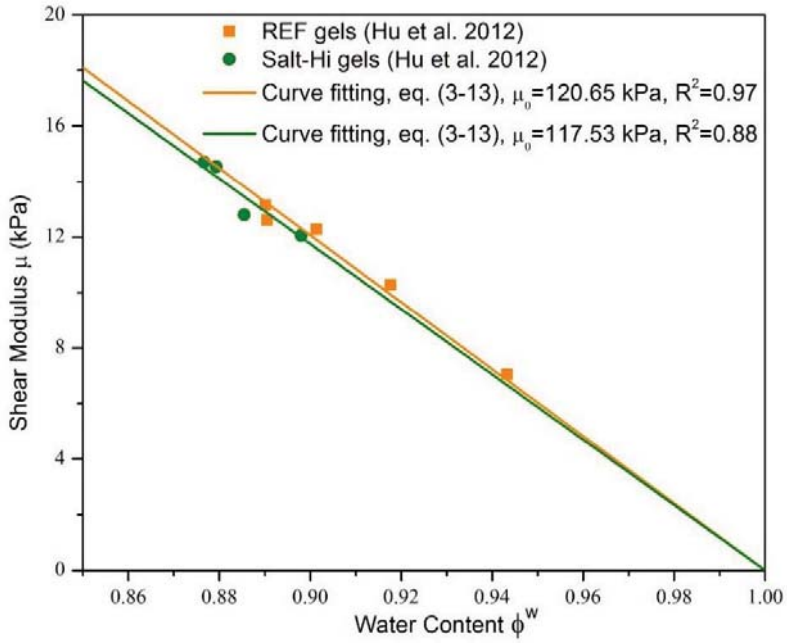

Figure 3-2 Variation of shear modulus with water content. REF gels and Salt-Hi gels are the names defined in (Hu et al., 2012) for two different compositions of poly (DMAEMA-co-AAm) hydrogels.

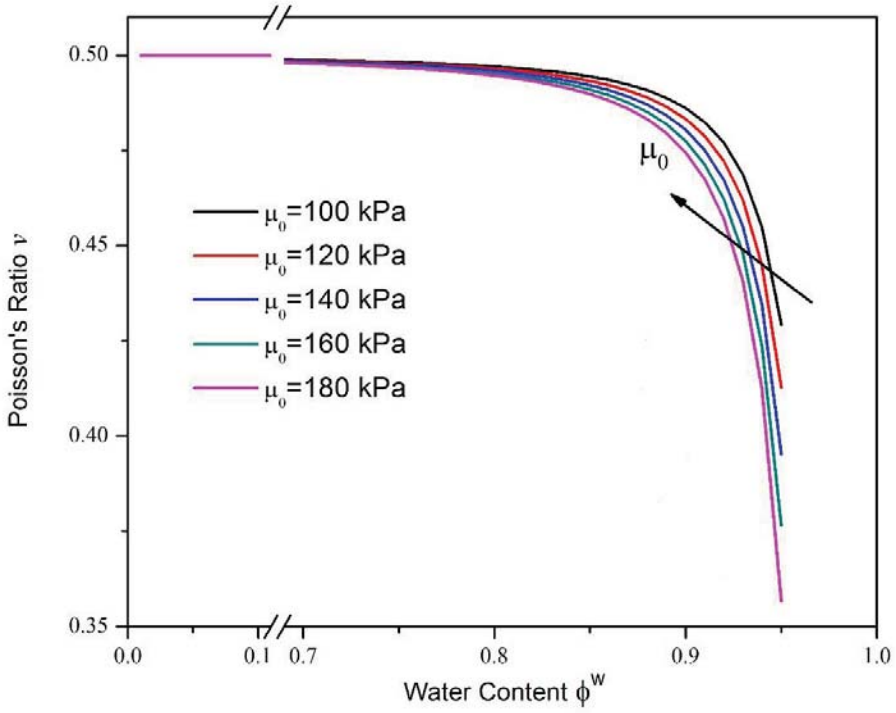

Figure 3-3 Variation of Poisson's ratio with water content for hydrogels. Poisson's ratio was calculated using eq. (3-14) with the aggregate modulus of agarose gels and different values of μ_0 (as the exact value for agarose gels is not available).

3.4 Discussion

Equation (3-7) can be written as,

$$D = \frac{k'}{\eta} H_A, \tag{3-15}$$

where k' is the Darcy permeability and η is the viscosity of fluid (e.g., water). The value of Darcy permeability k' represents the characteristic area of the pores in solid matrix (Gu et al., 2004). Equation (3-15) indicates that the value of water diffusivity is proportional to the area available for water diffusion, and proportional to the stiffness of the solid matrix, but inversely proportional to the interactions among water molecules (viscosity). This is because, at the microscopic level, the larger the pore size, the lower the probability for the

water molecules to collide with the solid matrix, thus the longer the mean distance that water molecules could travel. When it collides with the solid matrix, the water molecule will lose its momentum or kinetic energy. The loss of momentum or kinetic energy of water molecules during the collision would be less if the stiffness of the solid matrix is higher. Therefore, at the macroscopic level, the water diffusivity is related to the permeability and aggregate modulus of a biphasic material.

The mechanical properties and transport properties are related in hydrated materials, see eq. (3-7). That is, the diffusivity of water in these materials is related to the hydraulic permeability and the aggregate modulus if the material consists of intrinsically incompressible solid and fluid phases. Equation (3-7) indicates that it is unrealistic to have an isotropic hydrated material with both high stiffness and hydraulic permeability since the product of aggregate modulus and hydraulic permeability has an upper limit, which is equal to the value of water diffusivity (Figure 3-4). Understanding this limit is important for choosing a scaffold for in vitro engineering avascular tissues such as cartilage. For example, if an isotropic scaffold with high porosity is desired for the transport of nutrients, the material must be soft, not suitable for load support.

Compared with hydrogels, biological tissues usually have more complicated composition and microstructure. For example, articular cartilage has been shown as an anisotropic material with reinforced collagen fibers embedded in the isotropic matrix (Mow and Guo, 2002). The experimental results of aggregate modulus (H_A) and hydraulic permeability (k) for human and animal cartilage tissues (at the macroscopic level) have been reported

(Athanasiou et al., 1994; Athanasiou et al., 1991; Froimson et al., 1997; Mow et al., 1989). We found that the values of $H_A k$ are smaller than the value of D_0 for most cases, where D_0 is the water self-diffusivity in pure water, i.e., the upper limit for $H_A k$ (Figure 3-4). We also found that the values of $H_A k$ are close to the values of water diffusivity predicted by eq. (3-11) with ϕ^w in the range from 0.7 to 0.8 (Figures 3-4 and 3-5). This range of hydration is consistent with the experimental results for cartilage (Mow and Guo, 2002; Mow et al., 1984). These results indicate that eqs. (3-7) and (3-11) can be used for the material properties of cartilage determined at the macroscopic level. Note that the values of cartilage material properties at the macroscopic level are different from those determined by nanoindentation tests (Oyen et al., 2012).

With quantitative MRI techniques or nuclear magnetic resonance (NMR) method, one could measure the water content and diffusion coefficient in hydrated soft tissues such as articular cartilage and intervertebral disc (Chiu et al., 2001; Kerttula et al., 2001; Kerttula et al., 2000a; Liess et al., 2002; Xia et al., 1994). Equations (3-12) and (3-13) can be used to noninvasively determine the mechanical properties of biological soft tissues in vivo if the values of material parameters in eqs. (3-12) and (3-13) are known. Conversely, if the relationship between aggregate modulus and water content is known, one could noninvasively determine the hydraulic permeability of soft tissues using eq. (3-7) by measuring water diffusivity using quantitative MRI techniques.

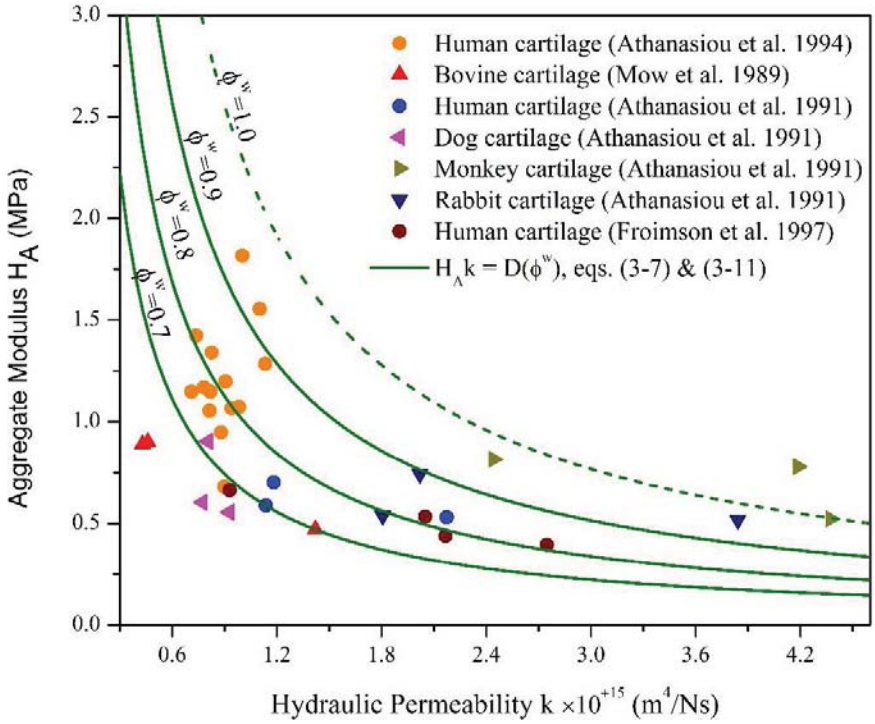

Figure 3-4 The relationship between hydraulic permeability and aggregate modulus for cartilage tissues. The solid and dash lines are predicted results with eqs. (3-7) and (3-11).

The Mackie and Meares' model was originally developed for ion diffusion in gels by assuming that the polymer network acts as a rigid sieve itself is not permeable to the solute or solvent. The motionless polymer chains increase the movement path length of the solute and solvent (Mackie and Meares, 1955; Masaro and Zhu, 1999). Therefore, this model may be more suitable to predict the self-diffusion coefficient (diffusivity under zero chemical potential gradient) of water rather than the mutual diffusion coefficient.

To our knowledge, there is no theoretical model for the mutual diffusivity of water in biological tissues and hydrogels yet. In this study, we adopted the Mackie and Meares' model to estimate the mutual diffusivity of water in biological soft tissues and hydrogels.

The water diffusivity in the agarose gel and cartilage measured by the NMR method is believed to be the self-diffusion coefficient of water, which can be predicted by the Mackie and Meares' model (Figure 3-5). The values of $H_A k$ for agarose gels determined by confined compression creep test are about 50% of the predicted values (Figure 3-5). But, interestingly, the values of $H_A k$ in cartilage determined with indentation tests (Froimson et al., 1997) are close to the predicted values, see Figure 3-5. These may be explained by the difference in methods used to determine the water diffusivity and the values of H_A and k. For example, it has been reported that the elastic modulus for cartilage obtained from the indentation test is about 30-79% higher than the value determined by confined and unconfined compression creep tests (Korhonen et al., 2002).

In this study, we derived a hydration-dependent equilibrium Poisson's ratio model for agarose gels. The Poisson's ratio for the gels approaches 0.5 as the hydration becomes lower than 0.7. This means that the gel is almost incompressible at low hydrated condition, which is consistent with the incompressible assumption of the solid phase. For gels with higher water content, the Poisson's ratio decreases nonlinearly with the increase of water content. This result is consistent with the experimental data found experimentally for other hydrogels (Hu et al., 2012). Since the Poisson's ratio is very sensitive to tissue hydration in gels with high water content, much attention should be paid to analyze the mechanical behavior of highly hydrated materials (e.g., nucleus pulposus).

In summary, a new constitutive model for hydration-dependent mechanical properties of hydrated materials has been developed. This new model has been checked with

experimental data for hydrogels and cartilage tissues in the literature. With this model, one can noninvasively measure the mechanical properties of the soft materials by determining the water content using NMR and MRI techniques. The model is also useful for designing the scaffold with proper mechanical properties for tissue engineering applications.

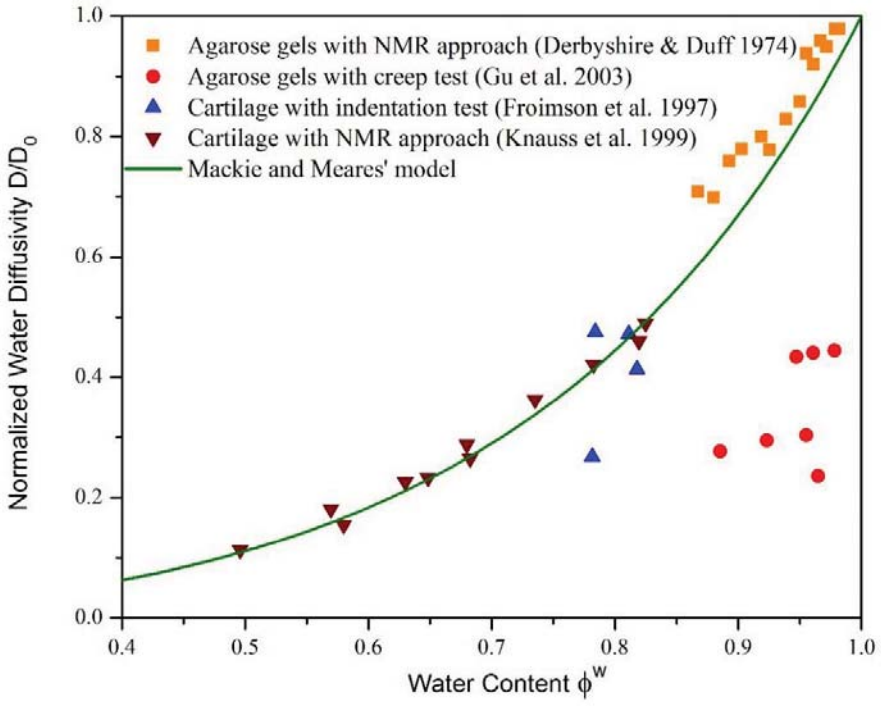

Figure 3-5 Variation of water diffusivity in cartilage tissues and agarose gels with tissue water content. The weight concentration ($c\%$, w/w) of the gel reported in (Derbyshire and Duff, 1974) was converted to water content in the gel by using a linear fitted relation ($\phi^w = -0.0065c + 0.9846$), which was obtained by curve fitting (R^2=0.98) our previous experimental results (Gu et al., 2003). The mass percentage of water in cartilage specimens reported in (Froimson et al., 1997) was converted to water content (i.e., volume fraction) by assuming the true mass density of solid matrix is 1.35 g/mm^3 (Gu et al., 1996).

Chapter 4

An Anisotropic Multiphysics Model for Intervertebral Discs

4.1 Introductory Remarks

During daily activities, IVDs act to transmit the axial load, resist shear load, and provide flexibility for the spine. The disc achieves these mechanical functions through its unique anatomic structure and tissue composition as explained in Section 2.2. Many biomechanical models have been developed to study the mechanical behavior of IVD as summarized in Section 2.5. However, it is still challenging to quantitatively describe the behavior of the disc under various loading conditions. The major challenge arises from the complicated couplings among multiple physical fields in the IVD and the anisotropic nature of the AF. The mechanical properties of cartilaginous tissues have been shown to be nonlinear and hydration dependent in Chapter 3. Moreover, the fiber bundles in the AF give the AF not only anisotropic mechanical properties but also anisotropic transport properties (Elliott and Setton, 2001; Gu et al., 1999; Iatridis et al., 1998; Jackson et al., 2012).

The objective of this chapter is to develop a more realistic anisotropic multiphysics model for the IVD, including the nonlinear couplings among anisotropic mechanical behaviors of solid matrix, anisotropic transport of interstitial fluid and ions, and electro-osmotic effect. Moreover, the hydration-dependent mechanical and transport properties will be incorporated into the model. The robustness of the proposed model will be demonstrated by performing 3D numerical simulations of the mechano-electrochemical behaviors of the disc using one set of material parameters and comparing the model predictions with those experimentally observed.

4.2 Development of Model

4.2.1 Anisotropic Multiphysics Model

The anisotropic multiphysics model presented in this study is based on the mechano-electrochemical continuum mixture theory (Frijns et al., 1997; Gu et al., 1998; Lai et al., 1991). The IVD is modeled as a mixture consisting of solid (s), fluid (w), cation ($+$), and anion ($-$). Each constituent has a volume fraction (ϕ^α, $\alpha = s, w, +, -$) relative to the whole mixture.

Governing equations. For each constituent, the mass balance equation is given by

$$\frac{\partial \rho^\alpha}{\partial t} + \nabla \cdot (\rho^\alpha \mathbf{v}^\alpha) = 0, \tag{4-1}$$

where ρ^α and $\mathbf{v}^\alpha$ are the apparent density per tissue volume and velocity of constituent α, respectively. The concentration (moles per fluid volume) instead of density is commonly used for ions. The density can be converted to concentration via $\rho^i = \phi^w M^i c^i$ ($i = +, -$),

where c^i is the concentration of ion i per fluid volume, and M^i is the molar weight of ion i. Thus, the mass balance equation of ions can be written alternatively as,

$$\frac{\partial(\phi^w c^i)}{\partial t} + \nabla \cdot (\mathbf{J}^i + \phi^w c^i \mathbf{v}^s) = 0, \tag{4-2}$$

where $\mathbf{J}^i = \phi^w c^i (\mathbf{v}^i - \mathbf{v}^s)$ is the molar flux of ion i relative to the solid phase.

Each constituent is assumed to be intrinsically incompressible with a true density, ρ_T^α, hence $\rho^\alpha = \phi^\alpha \rho_T^\alpha$. Therefore, the mass balance equation for the whole mixture can be obtained by taking summation of all the mass balance equations for each constituent,

$$\frac{\partial(\sum_\alpha \phi^\alpha)}{\partial t} + \nabla \cdot [\sum_\alpha (\phi^\alpha \mathbf{v}^\alpha)] = 0. \tag{4-3}$$

We further assume that the mixture is saturated and the volume fractions of the ions are negligible, so that, $\phi^s + \phi^w \approx 1$. Thus, the mass balance equation for the whole mixture can be alternatively written as,

$$\nabla \cdot (\mathbf{v}^s + \mathbf{J}^w) = 0, \tag{4-4}$$

where $\mathbf{J}^w = \phi^w (\mathbf{v}^w - \mathbf{v}^s)$ is the volume flux of interstitial fluid relative to the solid phase.

The electro-neutrality condition is assumed for every point in the disc, that is,

$$\sum_i z^i c^i - c^F = 0, \tag{4-5}$$

where z^i is the valence of ion i, and c^F is the fixed negatively charged density per fluid volume. The mobile ions are assumed to be monovalent in this study. The fluid content and fixed negatively charged density are both deformation dependent,

$$\phi^w = \frac{\phi_r^w + J - 1}{J}, \tag{4-6}$$

$$c^F = \frac{\phi_r^w c_r^F}{J - 1 + \phi_r^w}, \tag{4-7}$$

where ϕ_r^w is the fluid content at the reference state; $J = \det(\mathbf{F})$ is the volume ratio, where $\mathbf{F}$ is the deformation gradient tensor, and c_r^F is FCD at the reference state.

The general form of the linear momentum balance equation for constituent α is given by

$$\rho^\alpha \mathbf{a}^\alpha = \nabla \cdot \boldsymbol{\sigma}^\alpha + \rho^\alpha \mathbf{b}^\alpha + \boldsymbol{\pi}^\alpha, \tag{4-8}$$

where $\mathbf{a}^\alpha$, $\boldsymbol{\sigma}^\alpha$, and $\mathbf{b}^\alpha$ are the acceleration, Cauchy stress, and body force for constituent α, respectively, and $\boldsymbol{\pi}^\alpha$ is the momentum exchange between constituent α and other constituents. In this study, the body force term is neglected, and the acceleration term is also neglected with the assumption of quasi-static condition, thus,

$$\nabla \cdot \boldsymbol{\sigma}^\alpha + \boldsymbol{\pi}^\alpha = \mathbf{0}. \tag{4-9}$$

For the whole mixture, the exchange of linear momentum must be conserved, that is, $\sum_\alpha \boldsymbol{\pi}^\alpha = \mathbf{0}$. Therefore, the linear momentum balance equation for the whole mixture states,

$$\nabla \cdot \boldsymbol{\sigma} = \mathbf{0}, \tag{4-10}$$

where $\boldsymbol{\sigma}$ is the inner part of Cauchy stress for the mixture. Applying the restriction of entropy inequality to the whole mixture, together with the constraints of mass balance and electro-neutrality condition, the stress of the mixture is given by (Ateshian, 2007; Gu et al., 1998; Lai et al., 1991),

$$\boldsymbol{\sigma} = -p\mathbf{I} + \boldsymbol{\sigma}^s , \tag{4-11}$$

where p is the fluid pressure, and $\boldsymbol{\sigma}^s$ is the stress contributed by the solid phase.

The linear momentum balance equations for fluid and ions under quasi-static condition are (Lai et al., 1991):

$$\sum_{\alpha} \boldsymbol{\Gamma}_{\beta\alpha}(\mathbf{v}^{\alpha} - \mathbf{v}^{\beta}) - \rho^{\beta}\nabla\mu^{\beta} = \mathbf{0}, \tag{4-12}$$

where $\boldsymbol{\Gamma}_{\beta\alpha}$ is a positively defined and symmetric friction coefficient tensor (i.e., $\boldsymbol{\Gamma}_{\beta\alpha} = \boldsymbol{\Gamma}_{\alpha\beta} \geq 0$) between constituents β and α; and μ^{β} is the (electro)chemical potential per mass of constituent β. The chemical potential of fluid is given by (Gu et al., 1998; Lai et al., 1991),

$$\mu^{w} = \mu_0^{w} + \left[p - RT\sum_i \Phi^i c^i \right] \Big/ \rho_T^{w} , \tag{4-13}$$

where μ_0^{w} is the chemical potential at reference state, R is the universal gas constant, T is the absolute temperature, and Φ^i is the osmotic coefficient and it is assumed to be unity in this study. The electrochemical potential of ion is given by (Gu et al., 1998; Lai et al., 1991),

$$\mu^{i} = \mu_0^{i} + (RT / M^i)\ln(\gamma^i c^i) + z^i F_c \varphi / M^i , \tag{4-14}$$

where μ_0^i is the electrochemical potential at reference state, γ^i is the activity coefficient and it is assumed to be unity in this study, F_c is the Faraday constant, and φ is the electrical potential. In the mixture theory the electrochemical potential is continuous across the boundaries, thus the electrochemical potential of fluid and ions are chosen as the basic variables in the numerical simulation. Considering the ill-conditioning of the logarithm function with small value of c^i, and the arbitrary values of μ_0^w and μ_0^i, the following modified electrochemical potential for fluid and ions are used in numerical simulation (Sun et al., 1999):

$$\varepsilon^w = \left[(\mu^w - \mu_0^w)\rho_T^w \right] \Big/ (RT), \tag{4-15}$$

$$\varepsilon^i = \exp\left[(\mu^i - \mu_0^i) M^i / (RT) \right]. \tag{4-16}$$

From eq. (4-12), the volume flux for fluid, and molar fluxes for ions can be generally written as:

$$\begin{aligned} \mathbf{J}^w &= \phi^w (\mathbf{v}^w - \mathbf{v}^s) \\ &= -\phi^w (\mathbf{A}_{ww} \rho^w \nabla \mu^w + \sum_i \mathbf{A}_{wi} \rho^i \nabla \mu^i), \end{aligned} \tag{4-17}$$

$$\begin{aligned} \mathbf{J}^i &= \phi^w c^i (\mathbf{v}^i - \mathbf{v}^s) \\ &= \mathbf{A}_{iw} c^i \mathbf{J}^w - c^i \phi^w \sum_{j=+,-} \mathbf{A}_{ij} \rho^j \nabla \mu^j, \end{aligned} \tag{4-18}$$

where $\mathbf{A}_{ww}$, $\mathbf{A}_{wi}$, $\mathbf{A}_{iw}$, and $\mathbf{A}_{ij}$ are material coefficient tensors that are functions of friction coefficient tensors $\mathbf{\Gamma}_{\alpha\beta}$ defined in eq. (4-12). Note that $\mathbf{A}_{wi} \neq \mathbf{A}_{iw}$ and $\mathbf{A}_{ij} \neq \mathbf{A}_{ji}$.

The above two equations can be written in terms of modified electrochemical potentials [i.e., eq. (4-15) and eq. (4-16)] as:

$$\mathbf{J}^w = -RT\mathbf{K}(\nabla\varepsilon^{\mathrm{w}} + \sum_i \mathbf{M}_{wi}\frac{c^i}{\varepsilon^i}\nabla\varepsilon^i)\,, \tag{4-19}$$

$$\mathbf{J}^i = c^i\mathbf{H}_{iw}\mathbf{J}^w - c^i\phi^w\sum_{j=+,-}\frac{1}{\varepsilon^j}\mathbf{D}_{ij}\nabla\varepsilon^j\,, \tag{4-20}$$

where $\mathbf{K} = \mathbf{A}_{ww}(\phi^w)^2$ is the hydraulic permeability tensor, $\mathbf{M}_{wi} = \mathbf{A}_{ww}^{-1}\mathbf{A}_{wi}$ is the transport tensor of ion i, $\mathbf{H}_{iw} = \mathbf{A}_{iw}$ is the convection coefficient tensor of ion i, and $\mathbf{D}_{ij} = RT\phi^w c^j\mathbf{A}_{ij}$ is the coupling diffusivity tensor of ion i under the electrochemical gradient of ion j.

In this study, the $\mathbf{M}_{wi}$ and $\mathbf{H}_{iw}$ are both assumed to be unity tensors (Yao and Gu, 2007). We also neglect the coupling frictional effects between ions, that is, $\mathbf{D}_{ij} = \mathbf{0}$ for $i \neq j$. In the following sections of this chapter, we let $\mathbf{D}^i = \mathbf{D}_{ii}$.

Constitutive equations. The solid phase is modeled as a hyperelastic material. Thus, $\boldsymbol{\sigma}^s$ can be evaluated as, $\boldsymbol{\sigma}^s = \frac{2}{J}\mathbf{F}\frac{\partial\psi}{\partial\mathbf{C}}\mathbf{F}^T$, where ψ is the strain energy function, and $\mathbf{C} = \mathbf{F}^T\mathbf{F}$ is the right Cauchy-Green deformation tensor. The solid phase of NP and CEP can be modeled as isotropic material. Even though the solid phase is intrinsically incompressible, the solid phase is compressible as the result of inflow or outflow of fluid. Moreover, the microstructure of the solid phase is varying with the change of fluid content, so the

macroscopic mechanical properties depend on fluid content. Thus, the strain energy function should be able to describe the dependency on fluid content. We adopt the following strain energy function for NP and CEP (Ehlers and Eipper, 1999):

$$\psi = \psi_m = \frac{\mu}{2}(I_1 - 3) - \mu \ln J + \lambda(\phi_r^w)^2 \left[\frac{J-1}{\phi_r^w} - \ln(\frac{J-1}{\phi_r^w} + 1) \right], \qquad (4\text{-}21)$$

where μ and λ are the two Lame constants, $I_1 = tr(\mathbf{C})$ is the first invariant of $\mathbf{C}$, and $J^2 = \det(\mathbf{C})$ is the third invariant of $\mathbf{C}$.

The AF is an anisotropic tissue reinforced by two families of aligned fibers ($\mathbf{n}_r^\theta, \theta = 1,2$, representing the fiber directions at the reference state) which embed in the isotropic ground matrix. In this study, the fiber directions are assumed to be in the $\pm 30^\circ$ orientation to the horizontal plane. We adopted the fiber-reinforced model proposed by Holzapfel et al. (Holzapfel et al., 2000), in which the free energy function are decoupled into two parts to account for the contributions of the ground matrix (ψ_m) and the fibers (ψ_f) to the mechanical properties, thus,

$$\psi_{AF} = \psi_m(\mathbf{C}, \phi_r^w) + \psi_f(\mathbf{C}, \mathbf{N}_r^\theta), \qquad (4\text{-}22)$$

where $\mathbf{N}_r^\theta = \mathbf{n}_r^\theta \otimes \mathbf{n}_r^\theta$ is the structural tensor. The exponential type of strain energy function developed by Holzapfel et al. (Holzapfel et al., 2000) is adopted to characterize the mechanical behavior of fibers,

$$\psi_f = \frac{k_1}{2k_2} \{ \sum_{\theta=1}^{2} \mathcal{H}(I_f^\theta - 1) \exp[k_2 (I_f^\theta - 1)^2] - 2 \}, \qquad (4\text{-}23)$$

where k_1 and k_2 are the material parameters, $\mathcal{H}(\bullet)$ is the Heaviside step function, and $I_f^\theta = \mathbf{C}:\mathbf{N}_r^\theta$ is the square of the stretch of fiber in the direction of $\mathbf{n}_r^\theta$.

The embedded aligned fibers also affect the transport of fluid and ions within the AF. Following the permeability model for fiber-reinforced porous material proposed by Federico and Herzog (Federico and Herzog, 2008), the anisotropic hydraulic permeability tensor ($\mathbf{K}_{AF}$) for the AF can be written as,

$$\mathbf{K}_{AF} = (K_{\parallel} - K_{\perp})\mathbf{Q} + K_{\perp}\mathbf{I}, \tag{4-24}$$

where $K_{\parallel}$ and $K_{\perp}$ are the permeability parallel and the orthogonal permeability, respectively, which are defined as,

$$K_{\parallel} = (1-\phi^f)K_m, \tag{4-25}$$

and

$$K_{\perp} = (1-\phi^f)^2 K_m, \tag{4-26}$$

where ϕ^f is the volume fraction of the fiber in current state and it is dependent on the volume fraction in the reference state (ϕ_r^f) and the deformation as, $J\phi^f = \phi_r^f$, and K_m is the hydraulic permeability of the isotropic ground matrix. A hydration dependent hydraulic permeability model was developed by Gu et al. (Gu et al., 2003) for isotropic biological tissue as,

$$K_m = a\left(\frac{\phi^w}{\phi^s}\right)^b, \tag{4-27}$$

where a and b are two material parameters. The $\mathbf{Q}$ defined in eq. (4-24) is the directional average of the structure tensors,

$$\mathbf{Q} = \sum_{\theta=1}^{2} \frac{1}{2} \mathbf{N}^{\theta}, \tag{4-28}$$

where $\mathbf{N}^{\theta} = \mathbf{n}^{\theta} \otimes \mathbf{n}^{\theta}$ is the structure tensor in the current state, and $\mathbf{n}^{\theta}$ is the fiber directional vector in the current state, which can be determined via the deformation tensor as,

$$\mathbf{n}^{\theta} = \frac{1}{\sqrt{I_f^{\theta}}} \mathbf{F} \mathbf{n}_r^{\theta}. \tag{4-29}$$

The hydraulic permeability tensors for the NP ($\mathbf{K}_{NP}$) and CEP ($\mathbf{K}_{CEP}$) are isotropic tensors, so that,

$$\mathbf{K}_{NP} = \mathbf{K}_{CEP} = K_m \mathbf{I}. \tag{4-30}$$

By analogy to the models of hydraulic permeability tensor, the diffusivity tensors ($\mathbf{D}^i$) in eq. (4-20) for the AF ($\mathbf{D}^i_{AF}$), NP ($\mathbf{D}^i_{NP}$), and CEP ($\mathbf{D}^i_{CEP}$) can be written as,

$$\mathbf{D}^i_{AF} = (D^i_{\parallel} - D^i_{\perp})\mathbf{Q} + D^i_{\perp} \mathbf{I}, \tag{4-31}$$

$$\mathbf{D}^i_{NP} = \mathbf{D}^i_{CEP} = D^i_m \mathbf{I}, \tag{4-32}$$

with $D^i_{\parallel} = (1-\phi^f) D^i_m$, and $D^i_{\perp} = (1-\phi^f)^2 D^i_m$, where D^i_m is the diffusivity for the isotropic matrix. Gu. et al. (Gu et al., 2004) developed a hydration and ion size dependent diffusivity model for isotropic biological tissues, which states,

$$\frac{D^i_m}{D^i_0} = \exp\left(-m\left(\frac{r^i}{\sqrt{k_m \eta}}\right)^n\right), \tag{4-33}$$

where D^i_0 is the ion diffusivity in aqueous solution, m and n are two material parameters, r^i is the Stokes radii for the ion, and η is the viscosity of fluid and the value of 0.001 Ns/m^2 is used in this study.

4.2.2 Numerical Model

The governing equations are discretized with mixed finite element method following the approach developed by Sun et al. (Sun et al., 1999), and implemented in COMSOL software. The displacement of solid phase and electrochemical potential of fluid and ions are chosen as the basic variables. The geometry of the disc is based on a parametric model and scaled to the dimensions of the L4-5 disc (Broberg, 1983; O'Connell et al., 2007), and a half of the superior and inferior vertebral bodies are included, see Figure 4-1. In this study, the vertebral bodies are assumed to be rigid because they are much stiffer than the disc tissues. We choose the state that the disc is in equilibrium in the 300 mOsm saline solution as the reference state for all the following numerical simulations. The boundary conditions are prescribed according to each of specific simulation cases. The mechanical loads are applied on the vertebral bodies.

The parameters used in this study include the mechanical properties, transport properties, and electrochemical properties for AF, NP, and CEP, respectively. The values of mechanical properties, fluid content, and FCD are assigned uniformly in the NP and CEP, whereas linearly vary from the innermost AF to the outermost AF (Iatridis et al., 2007; Urban and Maroudas, 1979). This approach is different from the approaches in the literature, which usually assign the uniformly distributed mechanical properties to NP, CEP, and AF (or outer AF and inner AF) (Jacobs et al., 2014; Schroeder et al., 2010). Our approach also can alleviate numerical oscillation at the interface of AF and NP, which may

occur because of the jump of mechanical properties (Ruiz et al., 2013). The parameters are summarized in the Table 4-1.

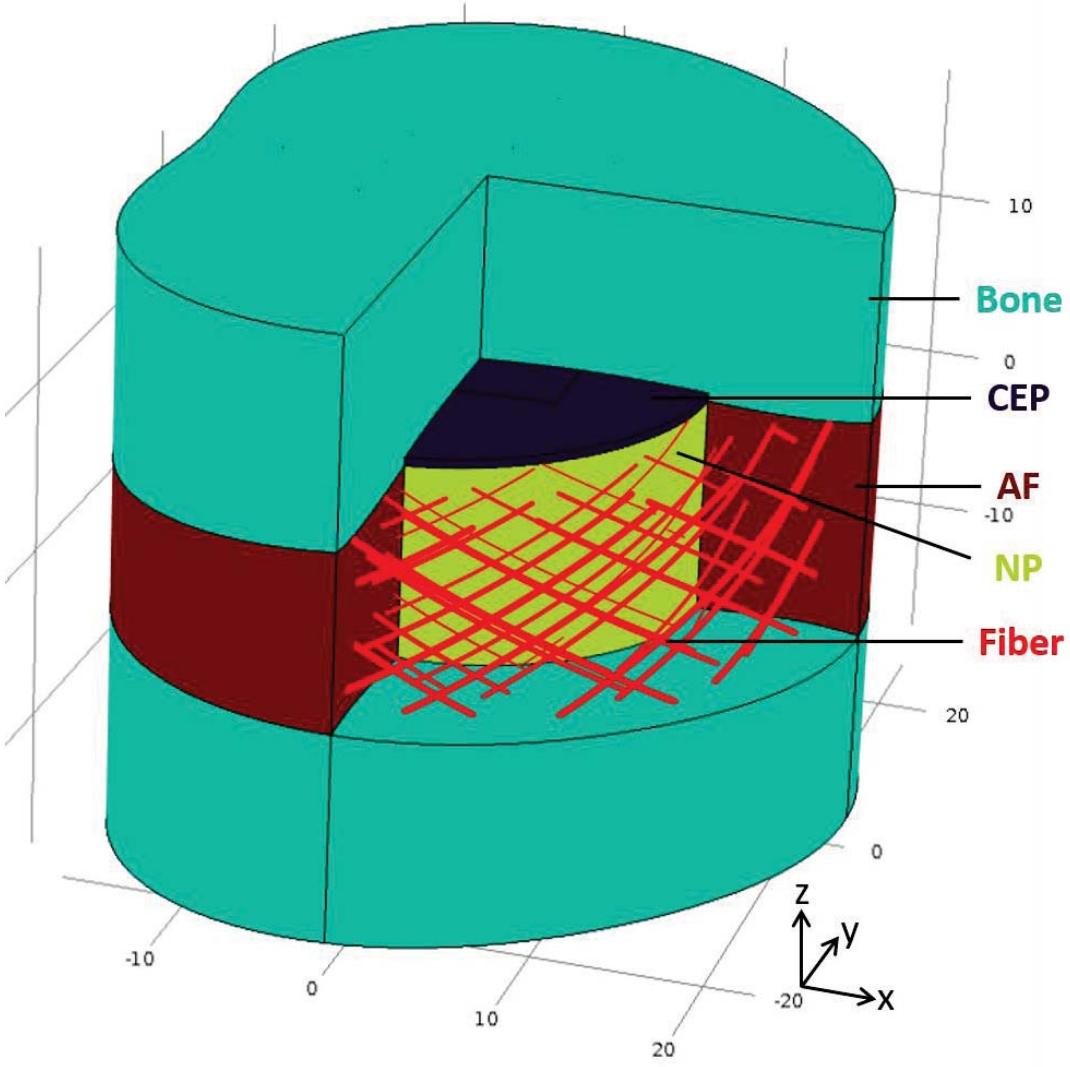

Figure 4-1 A schematic of the intervertebral disc showing the annulus fibrosus (AF), nucleus pulposus (NP), cartilaginous endplates (CEPs), and two families of fiber bundles in the AF. The dimensions are in millimeter.

Table 4-1 Material properties of IVD used in this study.

Parameter	AF*	NP	CEP	References
ϕ_r^w	0.86 to 0.77	0.86	0.75	(Cortes et al., 2014; Urban and Maroudas, 1979)
c_r^F (mM)	340 to 100	340	0	(Urban and Maroudas, 1979)
μ (kPa)	60 to 140	60	300	(Best et al., 1994; Cortes et al., 2014; Farrell and Riches, 2013; Iatridis et al., 1999; Iatridis et al., 1997a)
λ (kPa)	40 to 170	40	800	
k_1 (MPa)	1.18 to 5.34	N/A	N/A	(Ebara et al., 1996)
k_2	2.40 to 55.00	N/A	N/A	
a (10^{-17} m^4/(Ns))	3.10	2.48	0.13	(Cortes et al., 2014; Iatridis et al., 1998; Yao and Gu, 2004)
b	2.20	2.15	5.48	
r^i (nm)	0.20 (+), 0.14 (-)			(Gu et al., 2004)
D_0^i (10^{-9} m^2/s)	1.28 (+), 1.77 (-)			(Gu et al., 2004)
m	1.29	1.25	1.29	(Gu et al., 2004)
n	0.37	0.68	0.37	
ϕ_r^f	0.05 to 0.23	N/A	N/A	(Lu et al., 1996)

*(#) to (#) means the value linearly varying from the innermost to the outermost regions of AF.

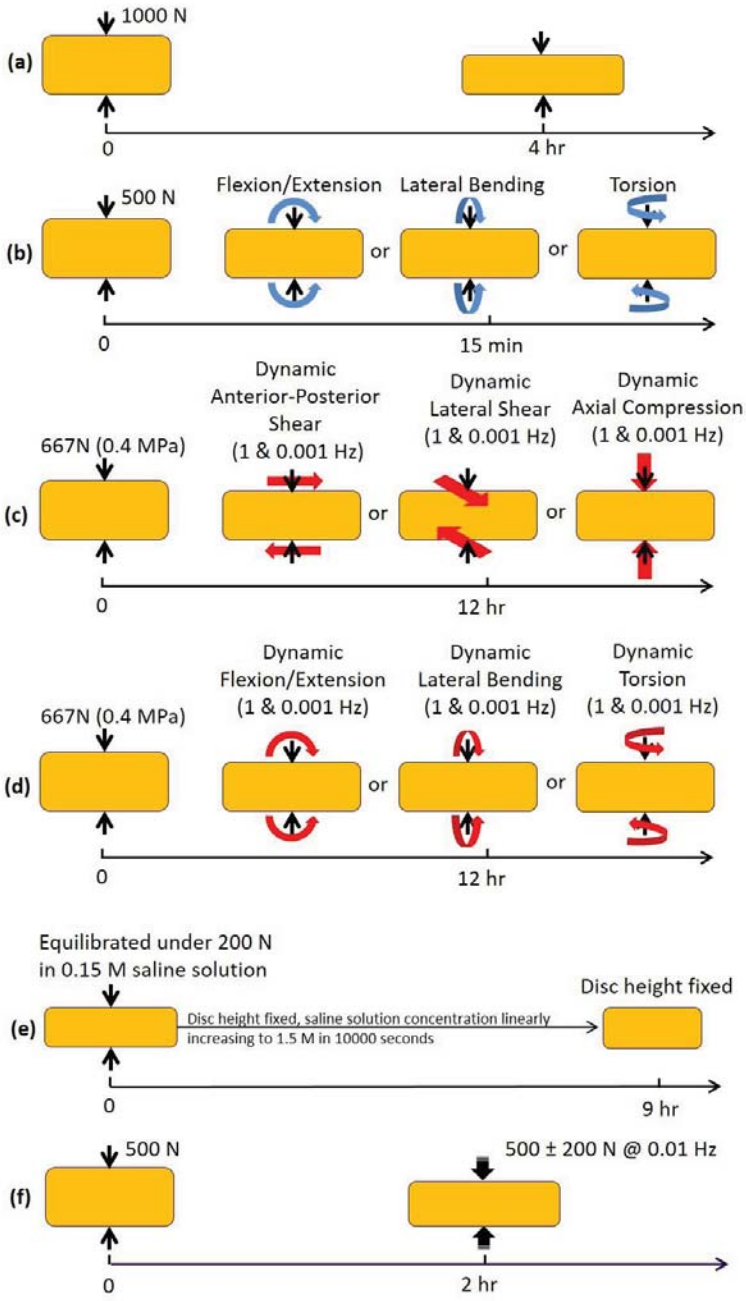

Figure 4-2 Schematic diagrams for experimental protocols used in simulations in this study. (a) creep test, (b) bending and torsion tests, (c) six-degree of dynamic loading tests (dynamic shear in anterior-posterior and lateral directions, and dynamic compression), (d) six-degree of dynamic loading tests (dynamic flexion/extension, dynamic lateral bending, and dynamic torsion), (e) osmotic loading test, and (f) dynamic loading test.

4.3 Numerical Examples

We perform numerical simulations of experiments reported in the literature to demonstrate that the proposed model is capable of predicting the complicated coupled mechano-eletrochemical phenomena observed experimentally. These experiments include the creep, bending and torsion, six-degree of freedom dynamic loading, osmotic loading, and dynamic loading (measuring electrical potential caused by dynamic loading) tests, see Figure 4-2. It is important to note that all the simulations are performed with one set of material parameters listed in Table 4-1. We are not trying to match or curve-fitting the experimental results exactly.

4.3.1 Creep Test

During most of our daily activities, the discs are subjected to the axial compressive loads. When a compressive load is applied, the disc height will decrease immediately and it will keep decreasing until reaching a new equilibrium. During the creep process, the fluid is pressed out, and the support of the compressive load shifts from fluid pressure to the stress of solid phase.

To demonstrate the capability of the proposed model to characterize the creep behavior of the whole disc, we performed finite element analysis of the creep process following the experiments conducted by O'Connell et al (O'Connell et al., 2011), in which the disc was compressed with 1000 N for 4 hours (O'Connell et al., 2011), see Figure 4-2 (a). The simulated disc height loss is 1.40 mm right after 1000 N axial load being applied at the rate of 10 N/s, and the loss increases to 3.14 mm at the end of the creep test. The predicted

history of disc height loss is reasonably consistent with the experimental results, see Figure 4-3.

During the creep, the interstitial fluid within the disc flows out through the AF periphery and CEP under the axial load. To our best knowledge, our proposed model is the first one to account for the anisotropic fluid and ions transport in the disc. Our model shows that the existing of fiber bundles decreases the averaged radial permeability in AF by about 10%. The compressive load is mainly supported by the fluid pressure, but the portion of support by the fluid decreases with the outflow of fluid. The fluid pressure in the NP is the largest and uniform across the NP, whereas the fluid pressure in AF linearly decreases from the inner AF to the outer AF, see Figure 4-4. The simulated results for distribution of fluid pressure are consistent with the experimental findings (Mcnally and Arridge, 1995). At the initial condition (no load) the fluid pressure in the NP is about 0.40 MPa, which is generated due to the higher osmolarity in the disc than that in the ambient environment, and the pressure is equilibrated by the tension of solid phase. Right after the 1000 N compressive load is applied, the fluid pressure in the NP increases to 1.33 MPa. The fluid pressure decreases to 1.18 MPa after 4 hours of creep test. McNally and Arridge (Mcnally and Arridge, 1995) reported that the fluid pressure is about 1.70 MPa in a healthy L4-5 disc under 1392 N compressive load. By linearly scaling the fluid pressure with the fraction of compressive loads, the fluid pressure at a 1000 N compressive load in the experiment would be 1.22 MPa, which is close to our simulated fluid pressure in the NP (1.18~1.33 MPa).

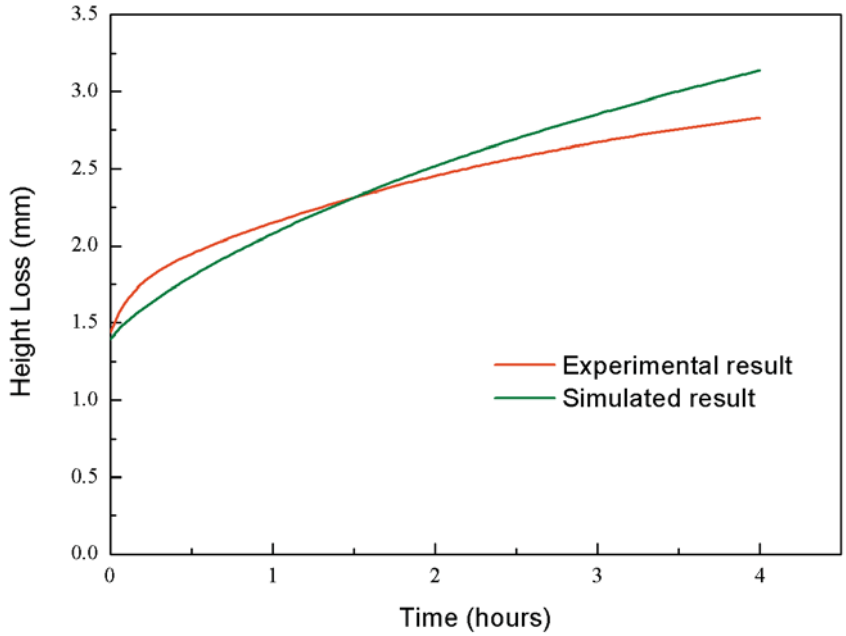

Figure 4-3 Simulated disc height loss during creep test, and compared with experimental results (O'Connell et al., 2011).

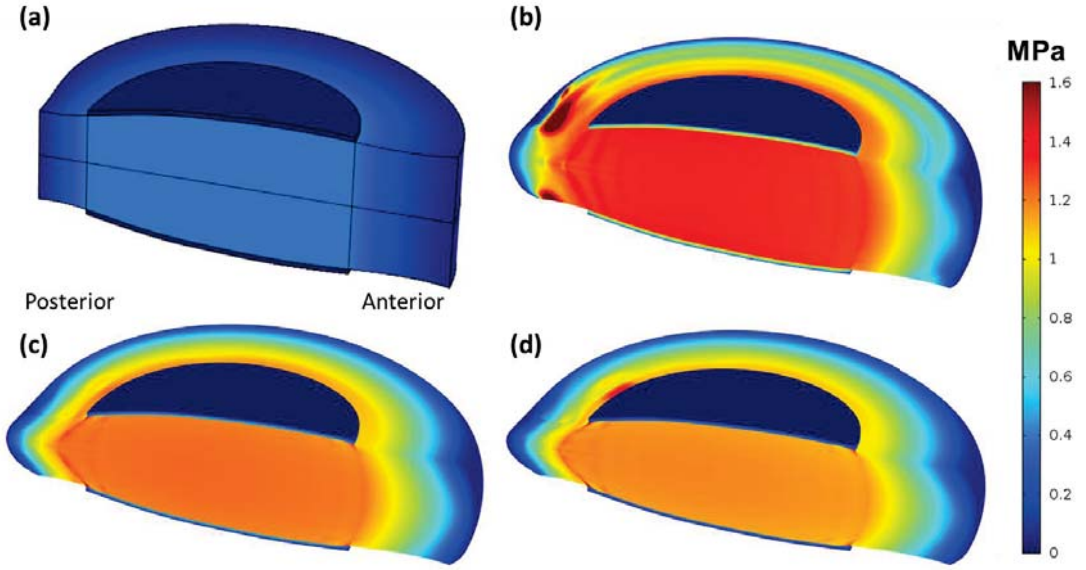

Figure 4-4 Fluid pressure during creep test. (a) before load applied, (b) right after load applied, (c) after 2 hours of creep, and (d) after 4 hours of creep.

4.3.2 Bending and Torsion Test

Besides the axial load, the disc is also subjected to bending and torsional loads during daily activities. In the experiments of Heuer et al. on the isolated human L4-5 discs, the loads were applied in three different directions, including flexion/extension, lateral bending, and axial rotation (Heuer et al., 2007). The load was applied at 1 °/s following a 15 minutes of creep under a 500 N compressive load, see Figure 4-2 (b). We simulated the disc under bending and torsional loads according to their experimental protocol, and the load is increased until the bending momentum reaching 5.0 Nm. The predicted ranges of motion under bending momentums of 2.5 Nm and 5.0 Nm are compared with experiment results, see Figure 4-5. It is shown that the predicted results are in the range of experimental data except for the axial rotation test. The stretches of fiber under the combined loads of compression (500 N) and bending (5.0 Nm) are shown to be less than 1.10 in most regions, see Figure 4-6, which are smaller than the failure stretch (1.09-1.15) (Skaggs et al., 1994). The stretch is higher for the fibers in the posterior/lateral-posterior regions for all the cases simulated, this explains why the failure occurs mostly in this region (Adams and Roughley, 2006).

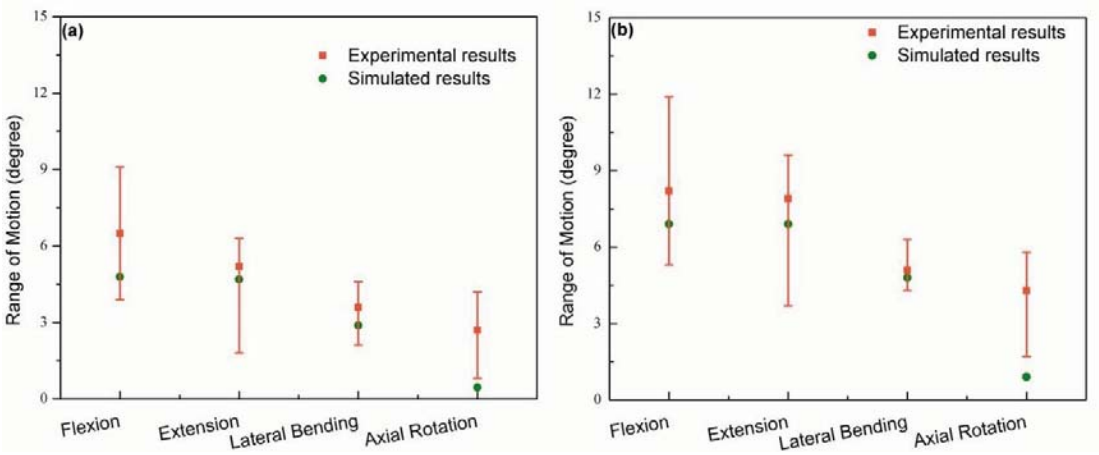

Figure 4-5 Simulated range of motion of disc under (a) 2.5 Nm and (b) 5.0 Nm bending momentums, and compared with experimental results (minimum, median, maximum) (Heuer et al., 2007)

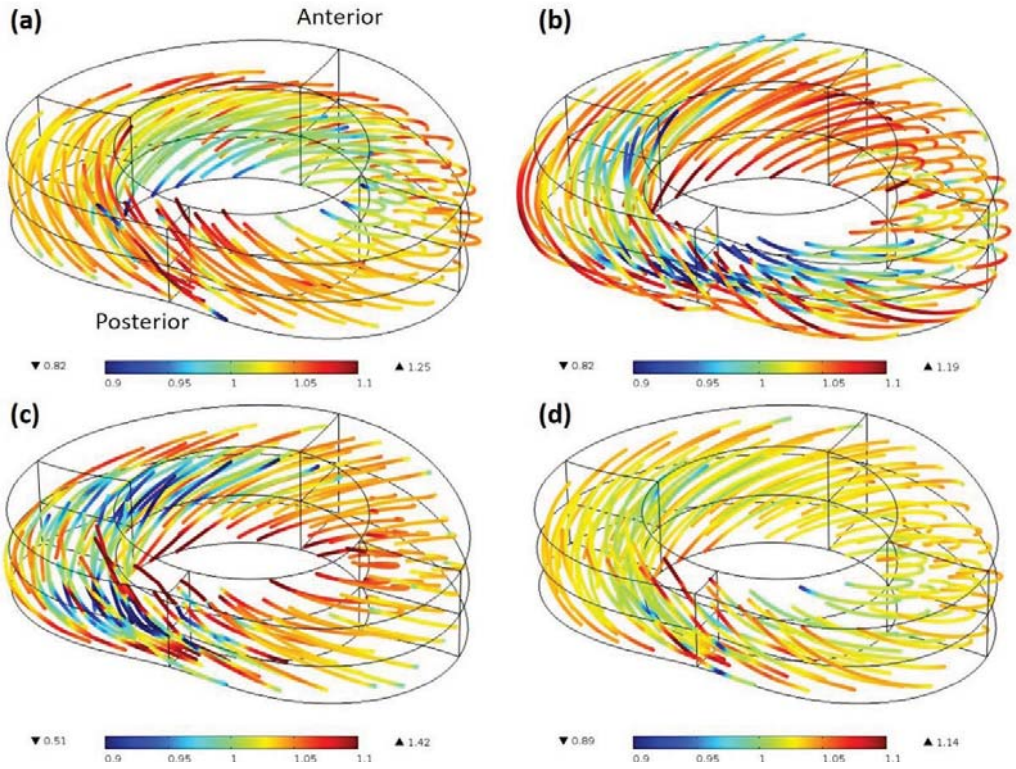

Figure 4-6 Distributions of fiber stretch under 5.0 Nm bending momentum in (a) flexion, (b) extension, (c) lateral bending, and (d) axial rotation. Only one family of fibers are shown.

4.3.3 Six-degree of Freedom Dynamic Loading

The disc usually undergoes dynamic loading and has six degrees of freedom, thus, it is important to validate the proposed anisotropic multiphysics model with a set of six-degree of freedom dynamic loading experiments. Costi et al., applied 3 displacements (Dx, Dy, and Dz in x, y, and z axial, respectively, with +x = anterior, +y = left lateral, and +z = superior) and 3 rotations (Rx, Ry, and Rz around x, y, and z axial, respectively) to motion segments (vertebra-disc-vertebra) after equilibrated overnight under 0.4 MPa preload in a bath of phosphate buffered saline at 37 °C (Costi et al., 2008), see Figures 4-2 (c) and (d). The dynamic loads were applied at four frequencies (1, 0.1, 0.01, 0.001 Hz). The amplitudes of displacements were: Dx = ± 0.6 mm; Dy = ± 0.6 mm; and Dz = ± 0.25 mm. The amplitudes of rotation angles were: Rx = ± 3°; Ry = ± 2°; Rz = ± 2°. We simulated these six-degree of freedom dynamic loading experiments following the experimental protocol at two frequencies (1 and 0.001 Hz), and the overnight preload was simulated as a constant compression for 12 hours. The simulated results were only compared with the experimental results of 2 grade 1 discs and 5 grade 3 discs (with a mean grade of 2.4) because the material properties used in this study were from non-degenerated or mildly degenerated discs. The mechanical responses of the disc under different dynamic loading with different frequencies simulated with our model were mostly comparable with experimental measurement (Costi et al., 2008; Stokes and Gardner-Morse, 2016), see Figures 4-7 and 4-8.

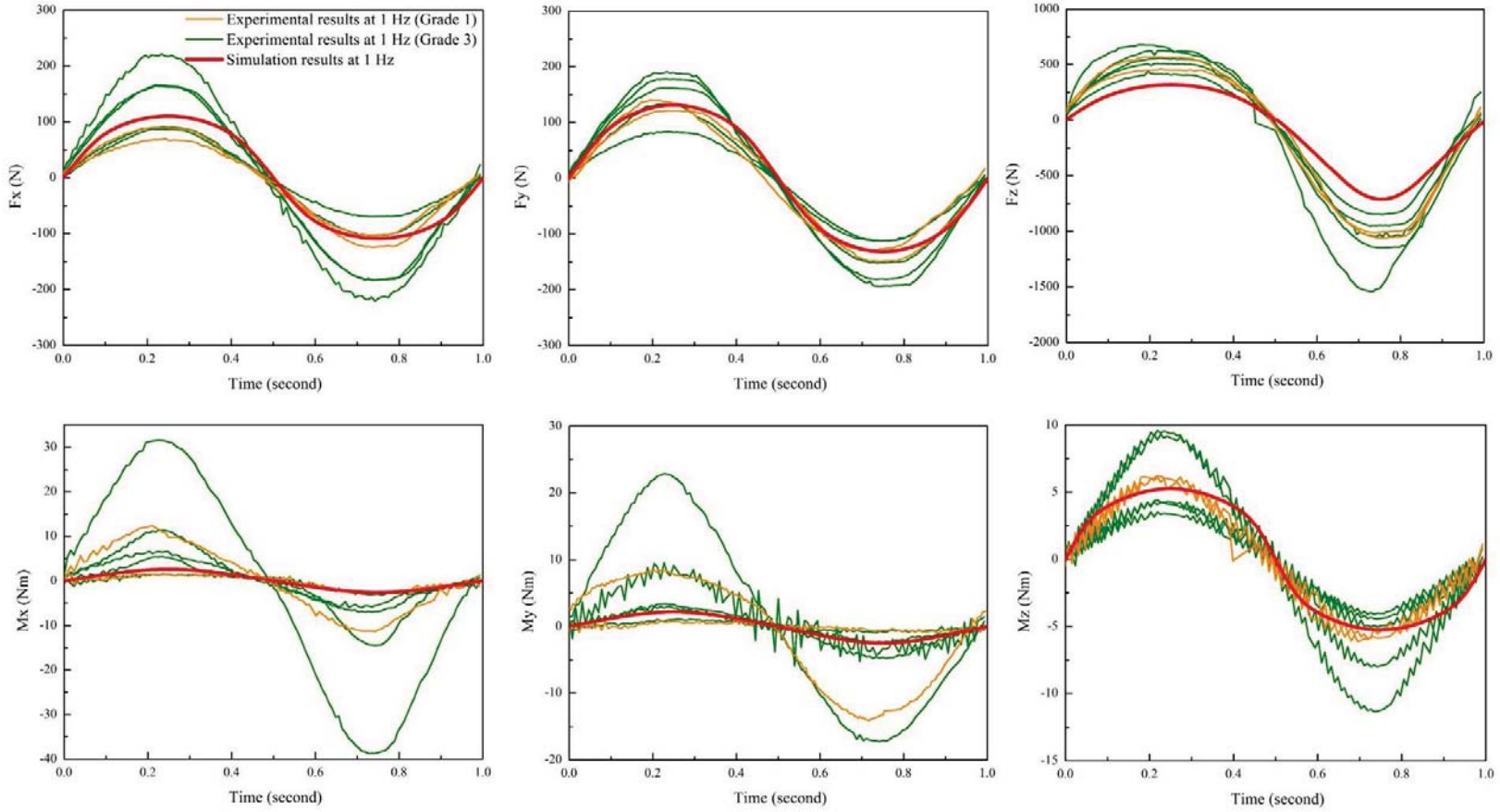

Figure 4-7 Simulated mechanical responses of the disc under different dynamic loadings (Dx, Dy, Dz, Rx, Ry, and Rz) at 1Hz, and compared with experimental results (Costi et al., 2008; Stokes and Gardner-Morse, 2016). Fx, Fy, and Fz represent the force in the x, y, and z axial, respectively. Mx, My, and Mz represent the moment around x, y, and z axial.

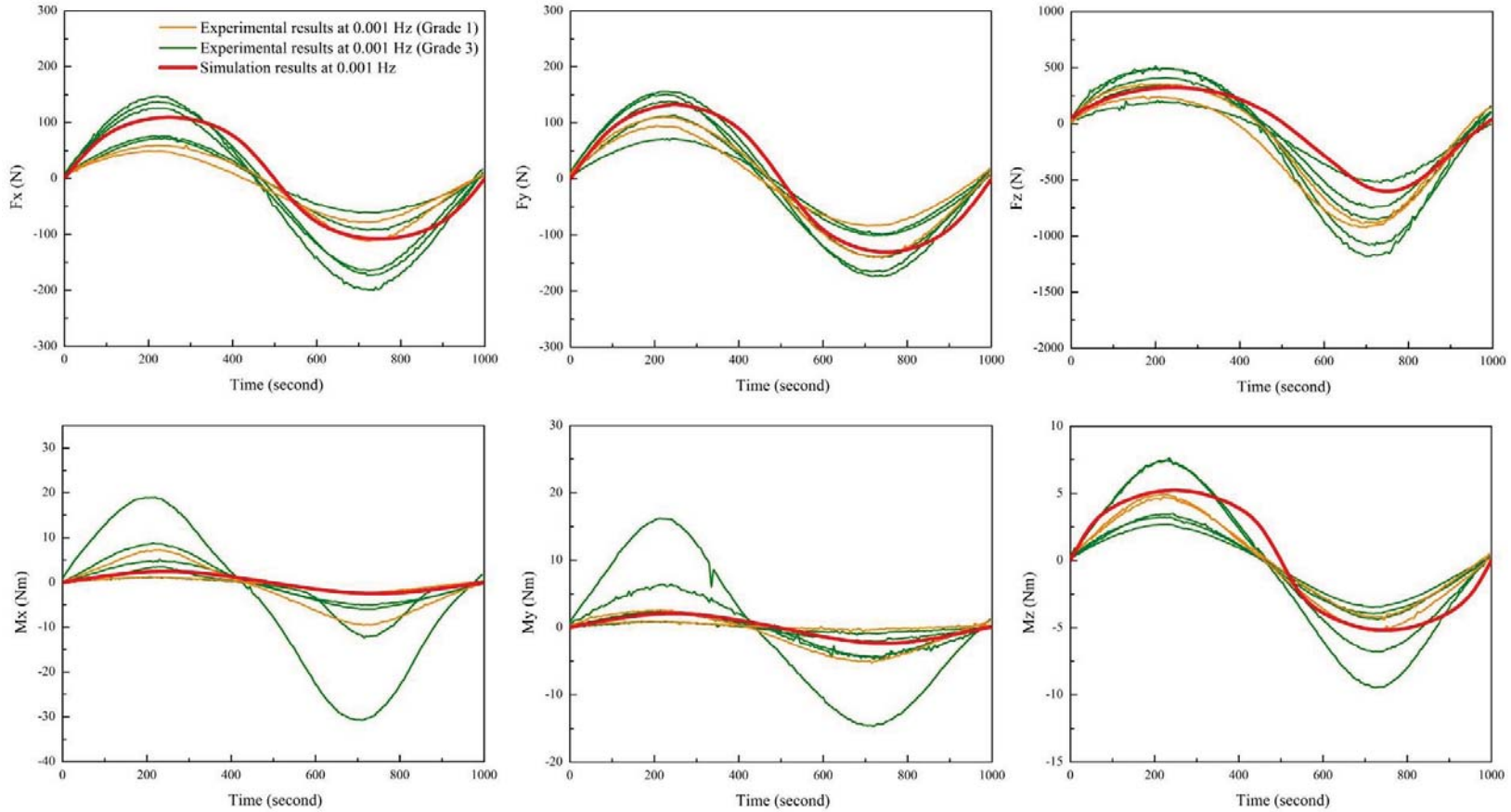

Figure 4-8 Simulated mechanical responses of the disc under different dynamic loadings (Dx, Dy, Dz, Rx, Ry, and Rz) at 0.001Hz, and compared with experimental results (Costi et al., 2008; Stokes and Gardner-Morse, 2016). Fx, Fy, and Fz represent the force in the x, y, and z axial, respectively. Mx, My, and Mz represent the moment around x, y, and z axial.

4.3.4 Osmotic Loading

Varying the external osmolarity is an important approach to investigate the contribution of fixed charges to the overall mechanical function of the tissue. Stokes et al. (Stokes et al., 2011) studied the response of human lumbar discs under constant compressive strain, in the bath with varying saline concentrations. They observed that varying external osmolarity from low to high causes a stress relaxation phenomenon. This is because the swelling pressure in the disc progressively reduces with time after increasing the external osmolarity. We simulate this stress relaxation phenomenon by following their experimental procedures. The disc is initially equilibrated in 0.15 M saline solution under 200 N compressive load. Then the compressive strain is fixed, and the bath saline concentration increases from 0.15 M to 1.5 M, see Figure 4-2 (e). Our simulated temporal relaxation of compressive load is in the range of experimental results, see Figure 4-9. However, in order to guarantee numerical stability, we ramp the external saline concentration linearly in 10,000 seconds, which is longer than that used in the experiment, which may cause the simulated relaxation of compressive load slower than the experimental result.

4.3.5 Intradiscal Electrical Potential under Dynamic Loading

The disc cells reside in a coupled mechano-electrochemical environment. The electrical potential around the cells is thought to be a potential factor that affects cellular activities (Setton and Chen, 2006). Iatridis et al. (Iatridis et al., 2009) reported that the spatial distribution of intradiscal electrical potentials under dynamic loading, which were measured under ±200 N axial load at 0.01 Hz following a 2-hour creep under 500 N compressive load, see Figure 4-2 (f). We simulate this phenomenon by following their

experimental protocol. The amplitude of the simulated electrical potential is normalized by the amplitude of dynamic load and compared with the experimental results. It is shown that our simulated results match well with the experimental results, not only the magnitude but also the distribution, see Figure 4-10.

4.4 Summary of Model

A more realistic anisotropic multiphysics model of IVD is developed based on the mechano-electrochemical continuum mixture theory. In this model, the solid phase, interstitial fluid, and ions are modeled as separated phases to characterize the nonlinear coupling phenomena among mechanical, electrical, and chemical fields. Moreover, the hydration-dependent anisotropic mechanical and transport properties of the disc tissue are also incorporated into the model. The numerical simulations, with one set of material parameters, demonstrate that this anisotropic multiphysics model is capable of systematically predicting disc mechanical behaviors and quantifying the mechanical, chemical, and electrical signals within the disc under various loading conditions.

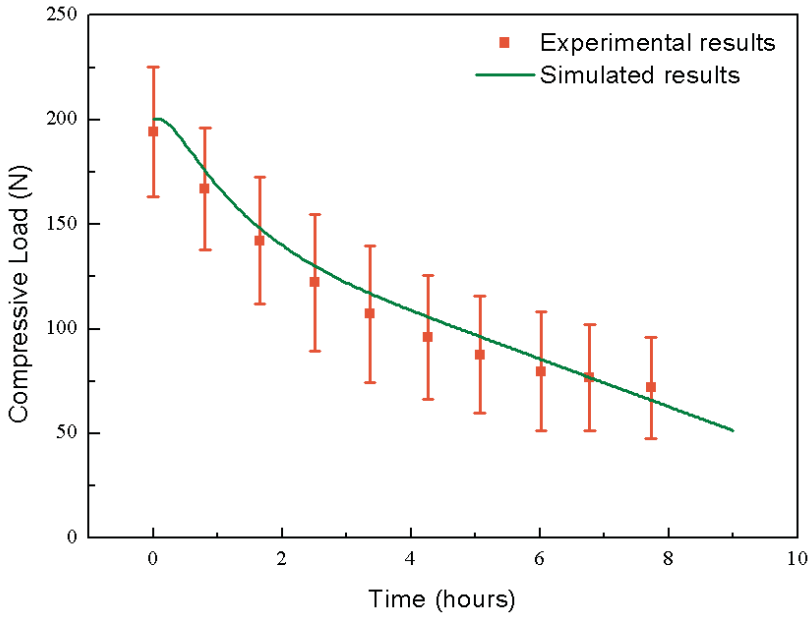

Figure 4-9 Simulated mechanical response of disc to the change of bath saline solution, from 0.15 M to 1.50 M, and compared with experimental results (Mean±SD) (Stokes et al., 2011).

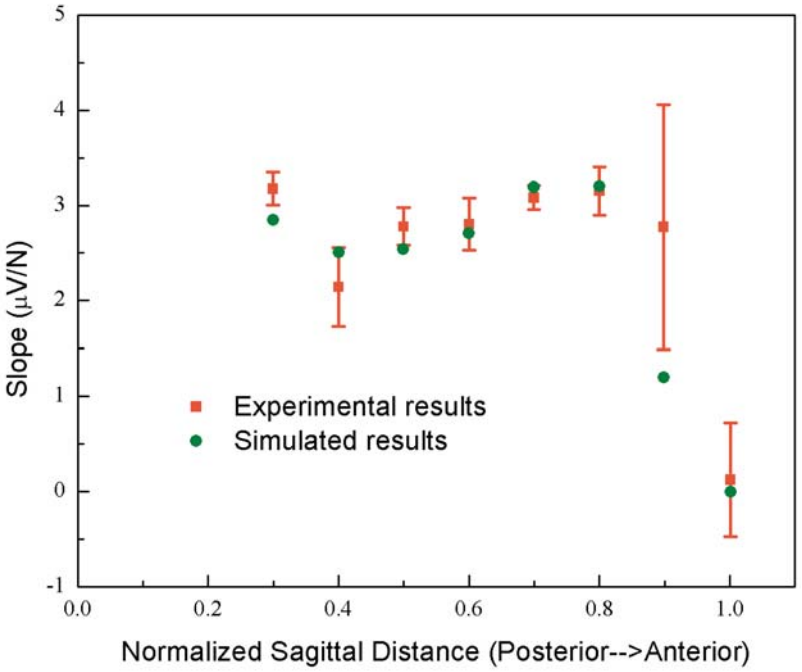

Figure 4-10 Simulated distribution of electrical potential under dynamical loading at mid-sagittal line, and compared with experimental results (Mean±SEM) (Iatridis et al., 2009).

Chapter 5

Initiation and Propagation of Damage in the Annulus Fibrosus Induced by Mechanical Loading

5.1 Introductory Remarks

Abnormal mechanical loading is a major factor that can cause the degeneration of IVDs. One possible mechanism is that abnormal mechanical loading causes the damage in the AF, which is supported by the strong association between the damage of AF and the disc degeneration with clinical observation, postmortem studies, and animal studies (Dullerud and Johansen, 1995; Masuda et al., 2005; Osti et al., 1990; Sharma et al., 2009; Yu et al., 1989). One of the typical damage patterns is the herniation of AF, which usually occurs in the posterior, or posterolateral AF regions (Maezawa and Muro, 1992; Ninomiya and Muro, 1992; Veres et al., 2009). The damage in AF has been classified into rim lesion, circumferential tear, and radial tear (Osti et al., 1992). The rim lesion is a horizontal tear of the outer AF. The circumferential tear is a tear in the circumferential direction and it is the most common damage in both posterior and anterior AF regions. The radial tear is a full thickness cleft radiated from the nucleus pulposus (NP) to the outer AF.

Many in vitro experiments have been conducted to study the association of different loading regimes with damage in the AF. For example, an axial compression on motion segments (vertebra-disc-vertebra) has been shown to cause fracture of the vertebra or CEP rather than the damage in AF (Brown et al., 1957; Lin et al., 1978; Roaf, 1960; Yoganandan et al., 1988); compression combined with flexion (compression-flexion) has been shown to cause damage in the posterior AF (Adams and Hutton, 1982a, b; Aultman et al., 2005; Mcnally et al., 1993; Tampier et al., 2007). Though these in vitro experiments have helped gain a significant amount of knowledge on the damage in AF, the transit process (initiation and propagation) of damage in the AF under mechanical loading has not been elucidated, which is important in quantifying the role of abnormal mechanical loading in the damage and degeneration of discs. It may be difficult to track the transit process of damage in the discs by observing and analyzing 2D tissue sections which is a widely used in vitro experimental approach in studying the damage of discs (Osti et al., 1992; Veres et al., 2008; Wade et al., 2015). Computational modeling is an alternative approach to study the damage of discs. Thus, the objective of this chapter is to develop a new computational model to study the initiation and propagation of damage in the AF.

5.2 Theoretical Model

This new computational model is based on the anisotropic multiphysics model developed in Chapter 4 and a continuum damage model (Balzani et al., 2006; Famaey et al., 2013). The anisotropic multiphysics model has been validated and shown to be able to describe nonlinear interactions among the multiple physical fields in the disc. The continuum damage model is able to model the damage of soft tissue, and it has been widely used in

modeling the damage of blood vessels which have similar fiber reinforced laminated structure to the AF (Balzani et al., 2006; Famaey et al., 2013).

In this study, we only considered the damage of the fiber bundles because: (1) the contribution of fiber bundles to the tensile modulus of AF is much larger than that of the ground matrix, and (2) the yield strain of fiber bundles under tension is much smaller than that of the ground matrix (Ebara et al., 1996; Fujita et al., 1997). The damage of fiber bundles was modeled by weighting the strain energy function of fiber bundles [eq. (4-22)] with a scalar damage variable, that is (Balzani et al., 2006; Famaey et al., 2013),

$$\psi_{AF} = \psi_m(\mathbf{C}, \phi_r^w) + \sum_{\theta=1,2} (1-d^\theta)\psi_f^\theta(\mathbf{C}, \mathbf{n}_r^\theta)\,, \tag{5-1}$$

where $d^\theta \in [0,1]$ is the damage variable. A possible evolution of the damage variable is given by (Balzani et al., 2006; Famaey et al., 2013),

$$d^\theta = d_{\max}\left[1-\exp\left(-\frac{\beta^\theta}{\gamma}\right)\right], \tag{5-2}$$

where $d_{\max} \in [0,1]$ and γ are two damage parameters, and β^θ is the internal damage variable which is a function of ψ_f^θ. In this study, we assumed that the damage was irreversible and unhealable. Thus, the value of β^θ is related to the maximum value of fiber strain energy in the loading history (within the time interval $0 \le \tau \le t$) (Balzani et al., 2006; Famaey et al., 2013),

$$\beta^\theta = \max_{0\le\tau\le t}\left\langle \psi_f^\theta(\tau) - \hat{\psi}_f \right\rangle, \tag{5-3}$$

where $\hat{\psi}_f$ is the strain energy at the initial damage state. The bracket, $\langle \bullet \rangle$, defined as $\langle \bullet \rangle = 0.5\left[(\bullet) + |\bullet|\right]$, is used to filter out negative values.

5.3 Numerical Simulation

A quarter of the 3D motion segment (L4-L5) was generated for numerical simulation on the assumption that the segment is approximately symmetric along the middle sagittal and middle axial planes, see Figure 5-1. The theoretical model developed above was discretized with finite element method following the approach proposed by Sun et al. (Sun et al., 1999), and implemented with COMSOL software. The values of (electro)chemical potentials for fluid and solutes in the blood serum were assigned at the interfaces between the CEP and the vertebra and at the periphery of AF. The mechanical loading boundary conditions were applied on the top of the vertebra surface. The mechanical, transport, and electrochemical properties of AF, NP, and CEP are shown in Table 4-1. The vertebra was modeled as a rigid body. In this study, the value of $\hat{\psi}_f$ in eq. (5-3) was assumed to be 100 kJ/m^3**,** independent of the anatomic region for the non-degenerated AF (Ebara et al., 1996). There are few experimental results available on the values of $d_{\max}$ and γ in eq. (5-2) for human AF. These two parameters govern the stress-stretch curve after the damage initiated. In this study, the values of $d_{\max}$ and γ were chosen to be 0.5 and 50 kJ/m^3, respectively. These values were chosen based on a displacement-load curve obtained with the tensile experiment on animal IVDs (Pezowicz, 2010).

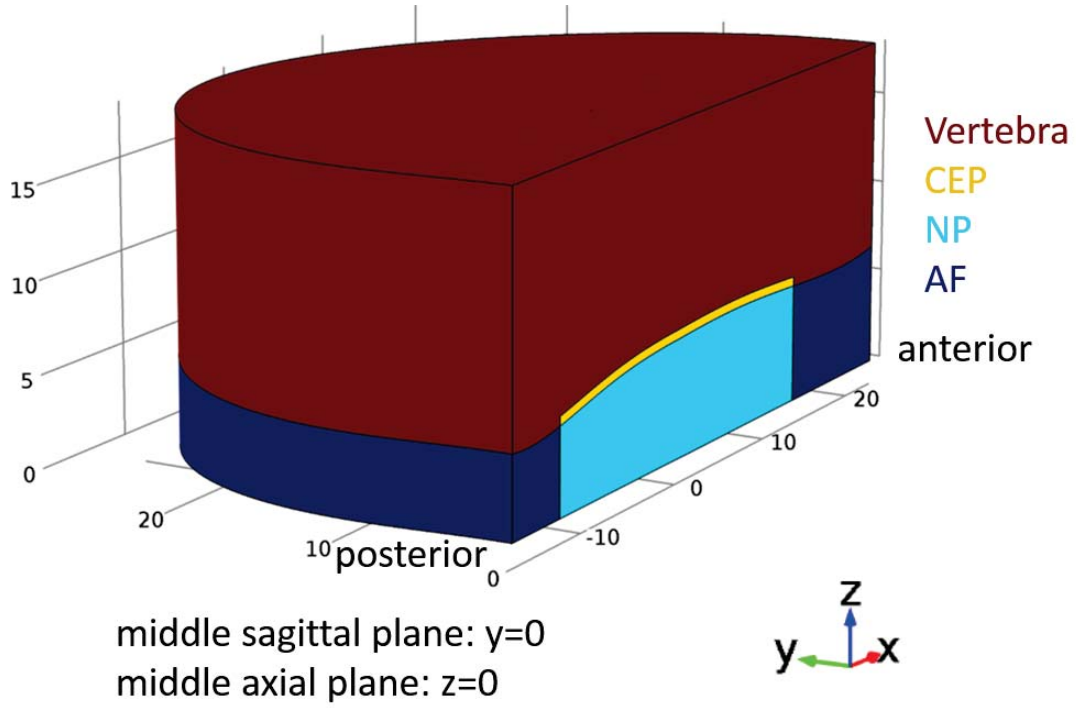

Figure 5-1 Schematic of a quarter of motion segment used in the numerical simulation. Length scale is in millimeter.

The initiation of damage under each of compression, flexion, and compression-flexion (compression followed with flexion), was simulated in this study. In the case of compression, the disc was vertically compressed at a rate of 1000 N/s to 2000 N. In the case of flexion, the disc was flexed at a rate of 1 °/s to 11°. The flexion was simulated by rotating the vertebra around the y axis (Figure 5-1). In the case of compression-flexion, the disc was flexed at a rate of 1 °/s to 11° following a 450 N compression (applied at 1000 N/s).

In this study, an overall damage variable, D, was defined to evaluate the damage of both families of fiber bundles, by,

$$D = \frac{1}{2}\sum_{\theta=1,2}(1-d^{\theta})\,. \tag{5-4}$$

The damage region was defined as wherever $D \le 0.9$ in this study. The volume fraction of damage region was defined as the volume ratio of the damage region to the whole AF region. It was used to evaluate the extent of the damage in the AF.

5.4 Results

5.4.1 Compression

The axial displacement increased nonlinearly with increasing the compressive load, see Figure 5-2. The displacement of the whole disc was 1.70 mm at a 2000 N of compression (with the rate of 1000 N/s). The damage initiated at about 700 N, then the volume fraction of damage region increased nonlinearly with the linear increase of the compressive load, see Figure 5-2.

The damage initiated in the outer posterior AF, middle posterior AF (adjacent to the vertebra), and the junction of posterior AF and CEP, see Figure 5-3 (a). The damage in these three regions increased with the increase of the compressive load. Additional damage initiated in outer anterior and outer lateral AF when the compressive load increased to about 1000 N, see Figure 5-3 (b), and this damage region expanded with increasing the compressive load. The radial thickness of the damaged AF reached to about 0.3 mm when the compressive load increased to 2000 N, see Figure 5-3 (c).

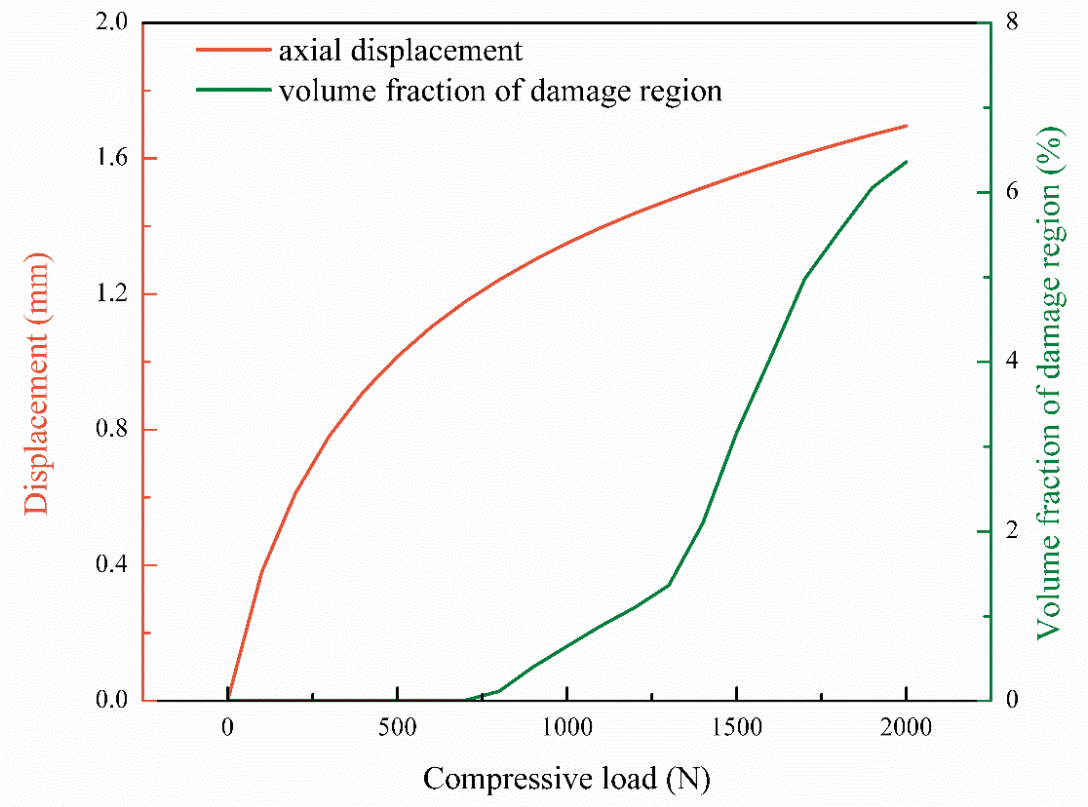

Figure 5-2 Axial displacement of disc surface and volume fraction of damage region in AF under compression.

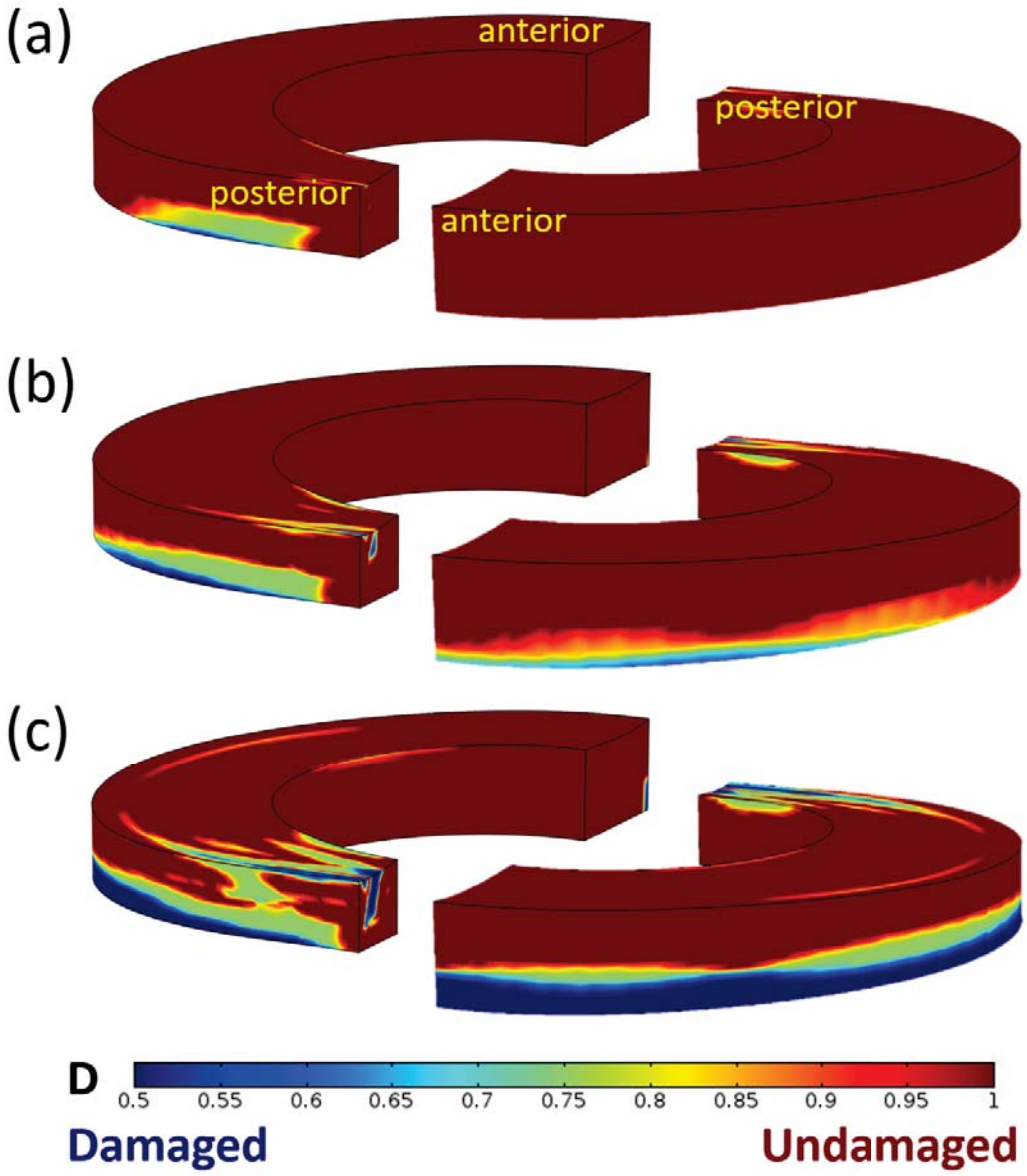

Figure 5-3 Damage distribution [represented by damage variable defined in eq. (5-4)] in AF compressed at a rate of 1000 N/s to: (a) 700 N; (b) 1000 N; and (c) 2000 N.

5.4.2 Flexion

Under flexion, the damage initiated at about 5° flexion, and the volume fraction of damage region increased nonlinearly to about 3.3% when the disc was flexed to 11°, see Figure 5-4. The damage initiated in the outer posterior AF adjacent to the vertebra when the disc was flexed to 5°, see Figure 5-5 (a). With the increase of flexion, the damage propagated vertically toward the mid-axial plane of the disc. Additional damage initiated in the middle-to-outer posterior AF when the disc flexion was increased to 8°, see Figure 5-5 (b). This new damage cut through the disc vertically when the flexion was further increased to 11°, and this damage merged with the initial damage in the outer posterior AF, forming a radial damage, see Figure 5-5 (c).

5.4.3 Compression-flexion

The damage initiated when the disc was flexed to about 5°, and volume fraction of damage region increased nonlinearly to 8.8% when the disc was flexed to 11°, see Figure 5-4. The damage initiated in the outer anterior AF, outer posterior AF, and the junction of posterior AF and CEP, see Figure 5-6 (a). The damage in these three regions expanded with the increase of flexion. When the disc was flexed to 9°, another damage initiated in the middle-to-outer anterior AF and inner-to-middle posterior AF, see Figure 5-6 (b). When the flexion further increased to 11°, the damage in the middle anterior AF merged with the damage in outer anterior AF, and the damage in the middle posterior AF propagated vertically to become a circumferential damage, see Figure 5-6 (c).

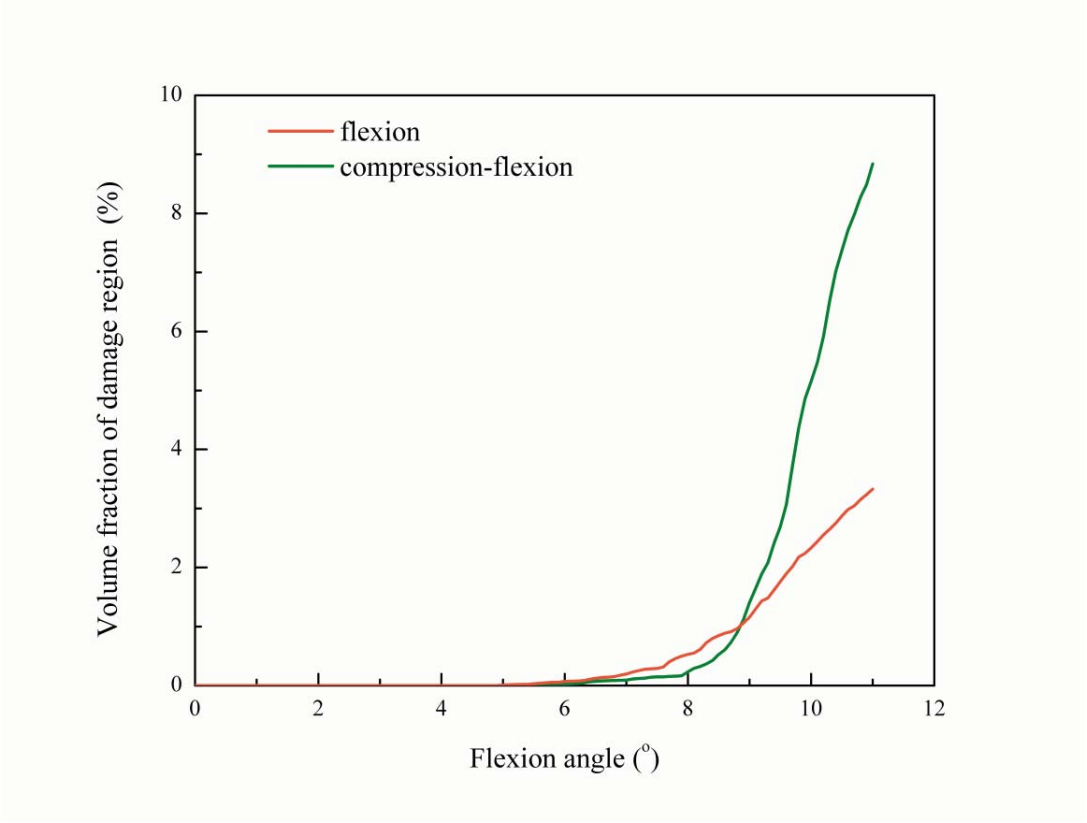

Figure 5-4 Volume fraction of damage region in AF under flexion and compression-flexion.

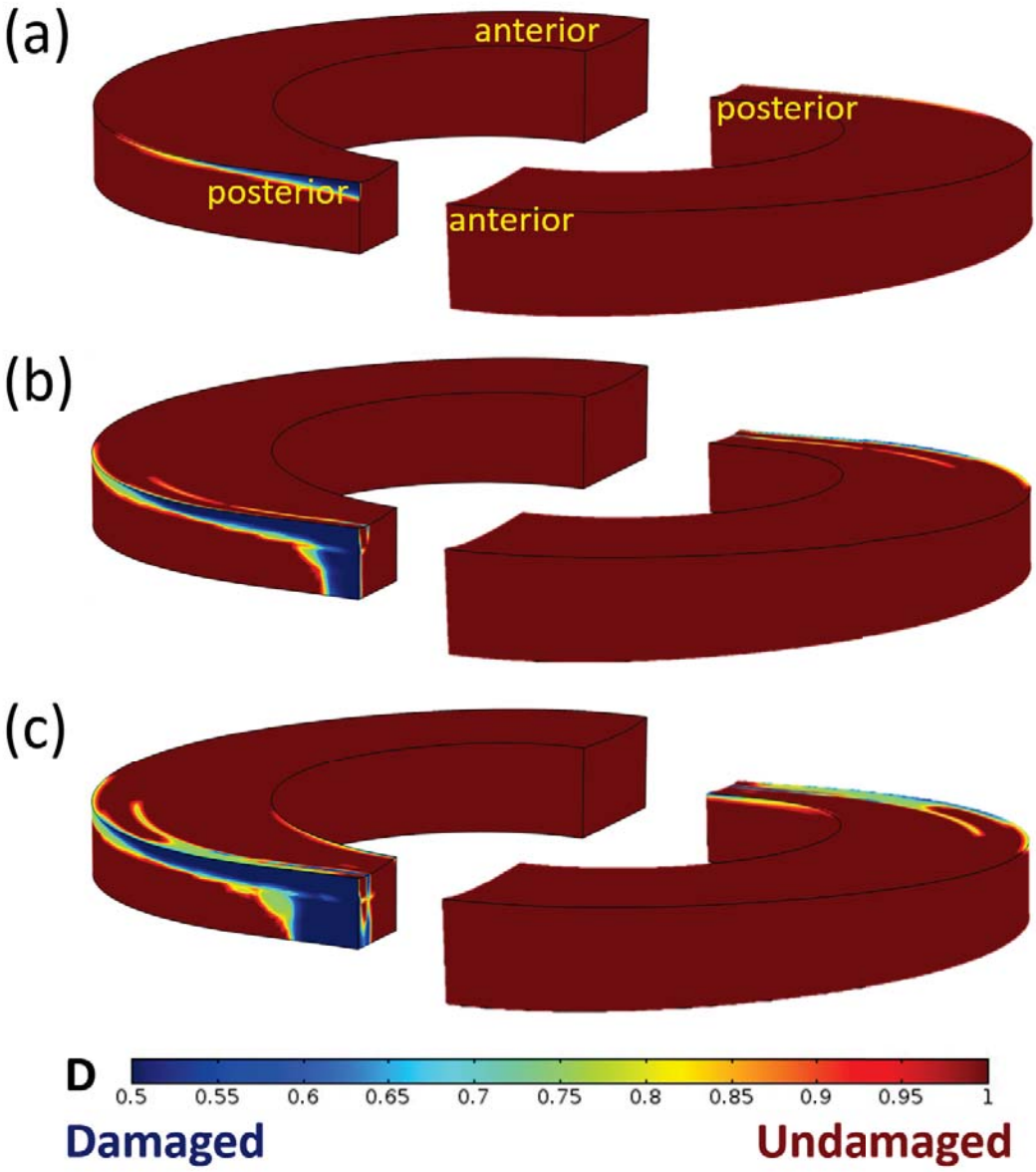

Figure 5-5 Damage distribution [represented by damage variable defined in eq. (5-4)] in AF under flexion at a rate of 1 °/s to: (a) 5°; (b) 8°; and (c) 11°.

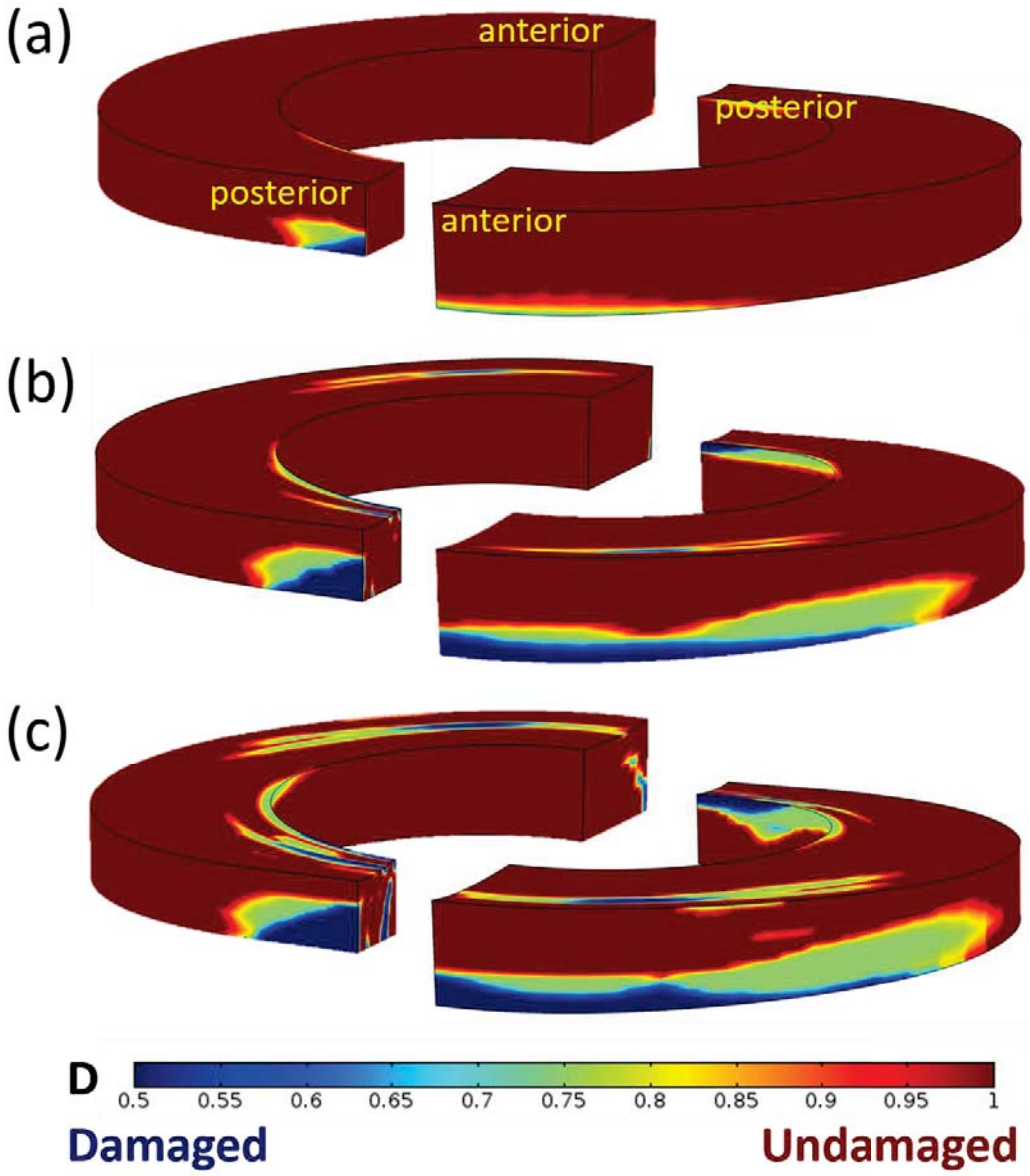

Figure 5-6 Damage distribution [represented by damage variable defined in eq. (5-4)] in AF under compression-flexion at a rate of 1 °/s to: (a) 5°; (b) 9°; and (c) 11°.

5.5 Discussion

In this study, a continuum damage model (Balzani et al., 2006) was incorporated into the anisotropic multiphysics model for IVDs developed in Chapter 4 to investigate the initiation and propagation of damage in the AF under compression, flexion, and compression-flexion. The continuum damage model has been widely used for modeling the damage of soft tissues (e.g., arterial walls) but not for the AF yet. In this study, only the damage of fiber bundles embedded in the AF ground matrix was modeled with the continuum damage model. The healing or repair of the damaged fiber bundles was not considered. The value of strain energy at initial damage state [$\hat{\psi}_f$ in eq. (5-3)] used in this study was from Ebara et al.(Ebara et al., 1996), which is not dependent on the anatomic regions for nondegenerate AF. Values of the other two parameters [$d_{\max}$ and γ in eq. (5-2)] were chosen based on an approximation from a displacement-load curve (Pezowicz, 2010) since very few experimental results are available in the literature. These values could affect the propagation speed of damage and the final damage state, and more experimental studies are needed to accurately determine their values. The axial displacement was predicted to be 1.35 mm under 1000 N (Figure 5-2), which is within the range of experimental measurements (1.08-1.71 mm with an average of 1.44 mm) (O'Connell et al., 2011). This result further demonstrates the robustness of the anisotropic multiphysics model developed in Chapter 4 in predicting the biomechanical behaviors of the IVD.

Under axial compression, when the loading magnitude reaches a value of 700 N or higher, the damage was predicted to initiate and propagate in three sub-regions of the posterior AF simultaneously; and with further increase in axial compressive load, the damage was also

predicted to appear in the anterior AF region [Figures 5-3 (a) and (b)]. The predicted initiation of damage in the junction of AF and CEP in this study is consistent with that from the finite element analysis by (Natarajan et al., 1994). This prediction is also consistent with the results from an in vitro experimental study measuring microstructure damage of ovine IVDs caused by pressurizing the NP (Veres et al., 2010). However, many in vitro experimental studies have reported that compressing a motion segment usually resulted in the fracture of CEP or crushing of the vertebrae rather than the damage of the disc (Brown et al., 1957; Lin et al., 1978; Roaf, 1960; Yoganandan et al., 1988). The differences between these in vitro experimental results and our predicted results are due to the different scales used in describing the damage. These in vitro experimental studies focused on the macroscale damage (or catastrophic damage) of the motion segment, and the failure loads were over 4000 N. In our current study, we focused on the microscale damage (with the volume fraction of damage region less than 7%) in the AF. The compressive load simulated in this study was less than 2000 N, which is much smaller than the failure load of the vertebral bodies and CEP.

Flexion and compression-flexion have different effects on the extent of damage. The volume fraction of damage region under flexion (up to 11°) was less than 3.3% (Figure 5-4), which is small and consistent with experimental finding that a 10° flexion would not cause damage in ovine discs (Wade et al., 2015). The volume fraction of damage region was 8.8% under the combination of 450 N compression and 11° flexion, which is about 2.7 fold of that under flexion alone (Figure 5-4). This difference, in addition to the fact that no damage occurred under 450 N compression (Figure 5-2), suggests that the combination of

compression and flexion is a more damageable loading regime. The predicted results of compression-flexion also indicate that microscale damage may occur under the combination of physiological compression (about 160 N to 830 N during the transition from lying to relax standing conditions; the values are converted with the disc area used in this study) (Wilke et al., 1999) and flexion (about 8° to 14° during the transition from erect standing to toe-touch flexion) (Veres et al., 2009).

Flexion and compression-flexion also have different effects on the location of damage initiation. Under flexion, damage initiated and propagated only in the outer and middle-to-outer posterior AF (Figure 5-5), whereas under compression-flexion, it initiated and propagated in the outer and inner-to-middle posterior AF, the junction of CEP and posterior AF, and the middle-to-outer, and outer anterior AF simultaneously (Figure 5-6). These differences are mainly due to the bulge of AF caused by compression. The stretches of the fiber bundles in the inner posterior AF and anterior AF in the disc under compression-flexion were higher compared to those under flexion (data not shown). Under compression-flexion, the damage in the junction of CEP and posterior AF and inner-to-middle posterior AF (circumferential damage) could form a radial damage [Figure 5-6 (c)]. This radial damage may provide a channel for NP material to migrate into AF, and may consequently cause disc herniation or extrusion of the NP material. Damage in the outer posterior AF and middle-to-outer posterior AF (circumferential damage) under flexion also could form a radial damage [Figure 5-5 (c)], but it would not cause the migration of NP material into AF region. Our predicted results indicate that circumferential damages can evolve into radial damages.

This study shows that the posterior AF is more susceptible to structure failure as damage initiated in the posterior AF under all three loading regimes (i.e., compression, flexion, and compression-flexion), which is consistent with the high frequency of damage in the posterior AF observed in human IVDs (Haefeli et al., 2006; Rajasekaran et al., 2013; Vernon-Roberts et al., 1997). Damage could initiate in three different sub-regions of the posterior AF (outer posterior AF, middle posterior AF, and the junction of posterior AF and CEP). Damage in the outer AF may facilitate the ingrowth of blood vessels and nerves, and consequently, cause low back pain (Adams and Roughley, 2006; Freemont et al., 1997; Peng et al., 2005). Damage initiated in the middle posterior AF could transform into circumferential damage with the increase of compression or flexion. The circumferential damage is due to the failure of fiber bundles rather than the inter-lamellar delamination. Similar damage phenomenon is also observed in in vitro experiments with damage development in the AF caused by pressurizing the NP (Pezowicz et al., 2006; Veres et al., 2008). The damage initiated in the junction of inner posterior AF and CEP is common in clinical observations as 65% of herniated lumbar discs were diagnosed with failure of the CEP junction (Rajasekaran et al., 2013), and an increasing number of studies support that this kind of damage is a mechanism causing further disc failure or degeneration (Rajasekaran et al., 2013; Veres et al., 2010).

This study has some limitations. Firstly, the roles of longitudinal ligaments and posterior elements in the deformation of disc were not considered in this study. This would limit our model in simulating the damage under in vivo loading condition, but it would not compromise the main objective of this study which is to develop a computational model to

simulate the damage in AF. Secondly, this study only considered the damage of fiber bundles in the AF, whereas the damage of ground matrix and the delamination of lamellae have not yet been included in the current model due to the lack of experimental results on human AF.

In summary, a new computational model was developed to simulate and predict the initiation and propagation of damage in the AF of a healthy human IVD under compression, flexion, and compression-flexion. This computational model is important for quantifying damage development in human IVDs under abnormal mechanical loading conditions.

Chapter 6

Glycosaminoglycan Synthesis Model for Cartilaginous Tissues

6.1 Introductory Remarks

The GAG plays an important role in cartilaginous tissues to support and transmit mechanical loads, and the decrease of GAG content is a sign of tissue degeneration (Antoniou et al., 1996; Maroudas, 1979). The GAG is produced and maintained by cells which live in a very complex mechno-electrochemical environment within the tissue (Maroudas, 1979; Setton and Chen, 2004; Snowden and Maroudas, 1972; Urban, 2002). A change in cell shape or volume has been known as a mechanism to perceive the alteration of extracellular environment by mammalian cells (Benzeev, 1991; Folkman and Moscona, 1978; Sarkadi and Parker, 1991). Currently, it has been found that direct membrane stretch has little or no influence on chondrocyte metabolic activities (O'Conor et al., 2014), which indicates cell volume change may play a role in regulating the synthesis activities. It was hypothesized that the change of cell volume could be a factor in mediating mechanotransduction in cartilaginous tissues (Guilak et al., 1995; Wong et al., 1997).

Osmotic loading and mechanical loading have been shown to affect the synthesis of GAG in vitro in both explant and cell culture experiments [e.g., (Bush and Hall, 2001; Gray et al., 1988; Gray et al., 1989; Guilak et al., 1994; Johnson et al., 2014; Maroudas and Evans, 1974; O'Conor et al., 2014; Sampat et al., 2013; Schneiderman et al., 1986; Urban et al., 1993)]. For example, the extracellular osmolarity has been found to have a dose-dependent effect on GAG synthesis rate by isolated cells (Ishihara et al., 1997; Negoro et al., 2008); the cells in the NP explant exhibit a higher synthesis rate of GAG at the osmolarity level close to the in situ value (van Dijk et al., 2011; van Dijk et al., 2013); the GAG synthesis rate has been observed to decrease in osmotic loaded articular cartilages (Bayliss et al., 1986; Schneiderman et al., 1986); a static compression has been shown to suppress GAG synthesis in articular cartilage (Kim et al., 1994; Schneiderman et al., 1986), whereas the GAG synthesis rate in bovine tail disc was found to be elevated if the static loading is less than 5 kg (Ohshima et al., 1995). However, there is no adequate theoretical model in the literature for the quantitative analysis and prediction of the effect of mechanical loading and/or osmotic loading on the synthesis rate of GAG in the cartilaginous tissues. Thus, the objective of this chapter is to develop a mathematical model to quantitatively investigate GAG synthesis rate by cells in cartilaginous tissues or in a culture medium under the mechanical and/or osmotic loading.

6.2 Development of GAG Synthesis Model

It has been found that cells of cartilaginous tissues exhibit maximum synthesis rate (R_0^{cell} , mole or mass per unit cell per unit time) of GAG at an in vivo state (refer to the optimal state, denoted by subscript 0) as mentioned in Section 6.1. Ishihara et al. experimentally

revealed that the change of GAG synthesis rate (R^{cell}) is proportional to the relative change of a cell volume (Ishihara et al., 1997). Based on their findings, in this study, we proposed a mathematical model for the relationship between GAG synthesis rate and cell volume:

$$\frac{R^{cell} - R_0^{cell}}{R_0^{cell}} = -\alpha \left| \frac{V^{cell} - V_0^{cell}}{V_0^{cell}} \right|, \tag{6-1}$$

where V_0^{cell} and V^{cell} are the cell volumes at the optimal state and current state, respectively, and α is a positive parameter characterizing the effect of cell volume change on GAG synthesis rate. Curve-fitting of eq. (6-1) to the experimental results (Ishihara et al., 1997) of GAG synthesis rate versus the volume changes of the cells from bovine NP, yielded $\alpha = 2.41$ (R^2=0.94), see Figure 6-1 (a).

The alteration of the cell volume can be attributed to its passive or active responses to biophysical stimuli. In this study, we focused only on the passive response of cell volume to osmotic loading and/or mechanical loading.

6.2.1 Effects of Osmotic Loading

It has been shown that the passive volumetric response of isolated chondrocytes or chondrocyte-like cells from the IVD to osmotic loading in a culture medium can be characterized by Boyle van't Hoff equation (Guilak et al., 2002; Nobel, 1969):

$$\frac{V^{cell} - V_0^{cell}}{V_0^{cell}} = \beta\left(\frac{\pi_0}{\pi} - 1\right), \tag{6-2}$$

where π_0 and π are the osmolarities at the optimal state and current state, respectively. The osmolarity can be estimated by the sum of the concentration of all dissolved particles

(or solutes, donated by i), that is, $\pi = \sum_i c^i$, where c^i is the concentration of solute i per fluid volume. The parameter β in eq. (6-2) is positive and its value is equal to the hydration of the cell at the optimal state (Ateshian et al., 2006). Substituting eq. (6-2) into eq. (6-1), it yields:

$$\frac{R^{cell}}{R_0^{cell}} = (1\text{-}\gamma \left| \frac{\pi_0}{\pi} - 1 \right|) \tag{6-3}$$

where $\gamma = \alpha\beta$. Curve-fitting to the experimental results (Ishihara et al., 1997) on GAG synthesis rate versus extracellular osmolarity, yielded $\gamma = 1.487$ and $\pi_0 = 404$ mOsm (R^2=0.91), see Figure 6-1 (b). Thus, the value of parameter β for bovine NP cells is 0.62, which is close to the value (about 0.6) for mesenchymal stem cells (Sampat et al., 2013).

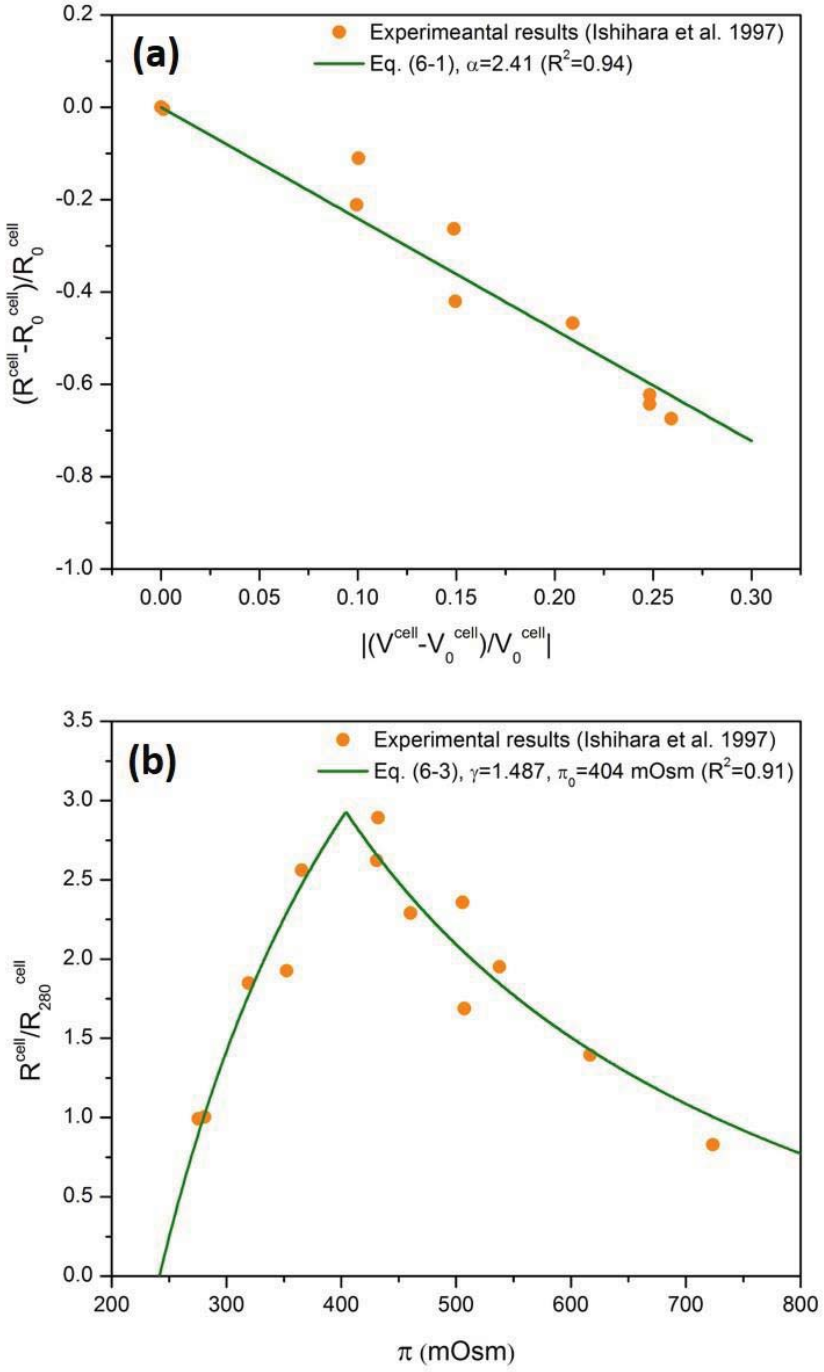

Figure 6-1 (a) GAG synthesis rate versus relative volume change of cells; (b) GAG synthesis rate versus extracellular osmolarity. The synthesis rates were normalized by the rate at 280 mOsm (R_{280}^{cell}) (Ishihara et al., 1997).

6.2.2 Effects of Mechanical Loading

The Boyle van't Hoff equation [i.e., eq. (6-2)] can characterize the volume change of an isolated cell under osmotic loading, but it is no longer valid for the cells in the tissue because the cells are encapsulated by the extracellular matrix (ECM) which provides external resistance to the deformation of the cell. In order to estimate the cell volume change as a function of tissue deformation, let us consider a simple case where a spherical cell is encapsulated in a larger sphere of the ECM, see Figure 6-2. The radii of a cell and matrix at the optimal state are r_c and r_m, respectively. The cell-matrix composite (Figure 6-2) is assumed to be subjected to a normal stress uniformly distributed at the matrix outer boundary, and the cell be attached to the matrix perfectly. At equilibrium state (without fluid flow), the deformation of the cell-matrix composite can be estimated by a linear elasticity theory. The equation of equilibrium in the spherical coordinate system is,

$$\frac{d}{dr}\left[\frac{1}{r^2}\frac{d}{dr}(r^2 u_r)\right] = 0, \tag{6-4}$$

where r is the radial coordinate, and u_r is the displacement in the radial direction. The relative volume change (i.e., dilatation) of the cell or composite can be obtained by calculating the change of the radius of the cell or composite using eq. (6-4). Thus, the dilatation of the cell, e_c [$e_c = (V^{cell} - V_0^{cell})/V_0^{cell}$, where V_0^{cell} is again the volume of the cell at the optimal state for GAG synthesis], is related to the dilatation of the composite (e), through

$$e_c = f(e) = \left[1 - \frac{E_m}{E_c}\frac{2(1-2\nu_c)(1-\chi^3)(\sqrt[3]{1+e}-1)}{2(1-2\nu_m)(\chi^3-\zeta)+(1-\zeta)(1+\nu_m)\chi^3}\right]^3 - 1, \tag{6-5}$$

where E_m and E_c are the Young's moduli of the matrix and cell, respectively, ν_m and ν_c are the Poisson's ratios of the matrix and the cell, respectively, $\chi = r_c / r_m$ (i.e., the ratio of radii), and

$$\zeta = \frac{E_c\left[2\chi^3(1-2\nu_m)+1+\nu_m\right]+2(1-\chi^3)(1-2\nu_c)E_m}{3(1-\nu_m)E_c}. \qquad (6\text{-}6)$$

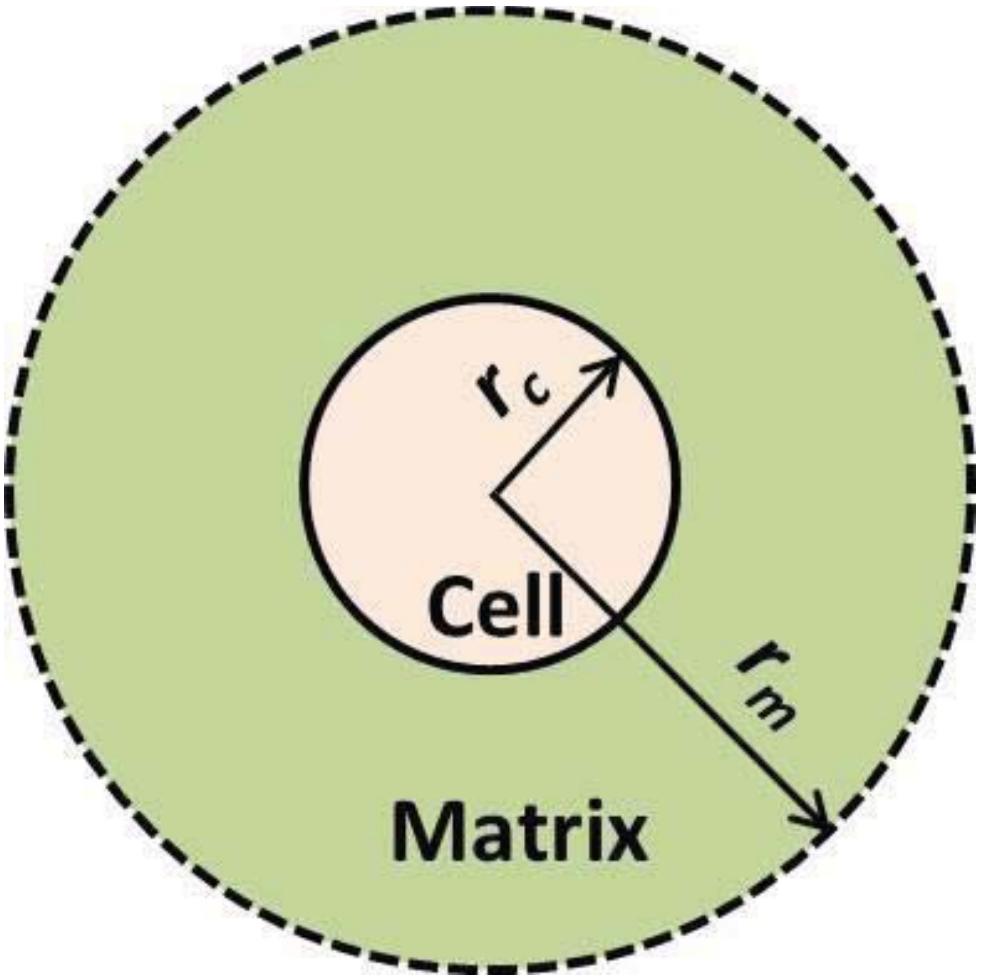

Figure 6-2 Schematic of a cell-matrix composite used for estimating the relative cell volume change.

From eqs. (6-1) and (6-5), the effect of local tissue deformation on GAG synthesis rate can be modeled as,

$$\frac{R^{cell}}{R_0^{cell}} = 1 - \alpha \left| e_c \right| = 1 - \alpha \left| f(e) \right|. \tag{6-7}$$

The Young's modulus for cartilage ECM and chondrocyte are 1000 kPa and 0.35 kPa, respectively, and the Poisson's ratio for ECM and chondrocyte are 0.04 and 0.43, respectively (Kim et al., 2008). The variation of the cell volume as a function of the composite dilatation is shown in Figure 6-3. Schneiderman et al. studied the effects of mechanical compression on GAG synthesis in human adult femoral head cartilage (Schneiderman et al., 1986). Based on experimental findings of (Schneiderman et al., 1986) and (Kim et al., 1994), the maximum GAG synthesis rate in cartilage is achieved when no external load is applied to the explant; thus, we assumed that the in situ cell volume at this state is V_0^{cell}. The volume fraction of chondrocytes in cartilage is assumed as 1% (i.e., $\chi^3 = 1\%$) (Stockwell, 1979), according to eq. (6-5), $\left| e_c \right| = \left| f(e) \right| \approx 1.52 \left| e \right|$, in the range of physiological deformations, see Figure 6-3. Curve-fitting to experimental results of (Schneiderman et al., 1986) on GAG synthesis rate versus tissue dilatation yielded $\alpha = 2.42$ (R^2=0.84), see Figure 6-4.

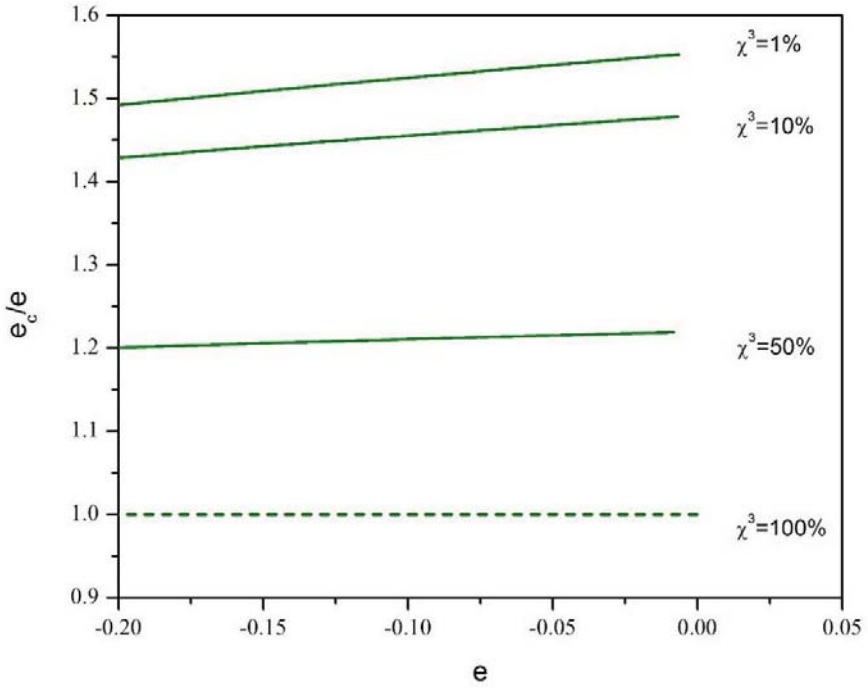

Figure 6-3 Relationship between composite dilatation (e) and relative cell volume change (e_c), χ^3 represents the cell volume fraction in the tissue.

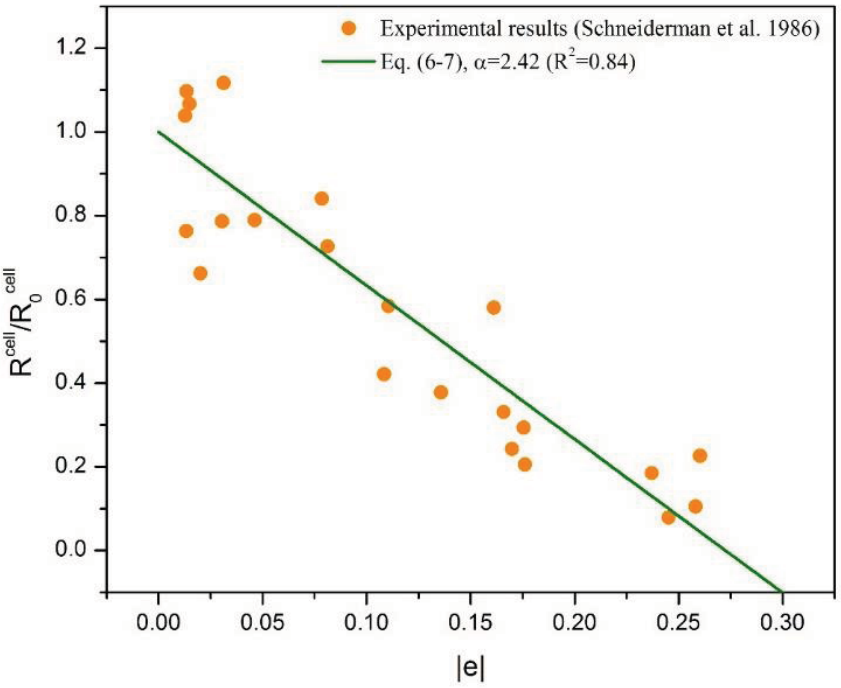

Figure 6-4 GAG synthesis rate in human femoral head cartilage explant versus tissue dilatation. The dilatation was converted from hydration (Lai et al., 1991).

6.3 Discussion

We proposed a mathematical model on cell volume dependent GAG synthesis rate [eq. (6-1)]. This model is based on the hypothesis that the change of cell volume is a primary mechanism for regulating the cell metabolic activities in cartilaginous tissues, and on the experimental findings that the GAG synthesis rate is sensitive to the cell volume and its maximum value is reached at an optimal cell volume (Ishihara et al., 1997; Negoro et al., 2008). In our model, the value of parameter α is assumed to be constant (i.e., independent of cell volume change). Although the physical meaning of the parameter α is not clear at cellular and molecular levels, it is interesting to note that the value of parameter α for isolated bovine NP cells in the culture medium under osmotic loading (α =2.41) is very close to the value for human chondrocytes in femoral head cartilage explant under mechanical loading (α =2.42). This is because the cell volume can be changed by osmotic loading or mechanical loading. It has been shown theoretically and experimentally that these two types of loading are equivalent if they impart to the cell with the same deformation (Lai et al., 1998; Schneiderman et al., 1986). Thus, it is the change in cell volume rather than the loading type that regulates the GAG synthesis. It is not a surprise to see the effect of osmotic loading on GAG synthesis [eq. (6-3)] for cells in the culture medium and the effect of static mechanical loading [eq. (6-7)] on GAG synthesis for cells in the explant can be delineated by a single model [eq. (6-1)], with the same value for parameter α. This finding indicates that one may obtain the value of α using isolated cells with an osmotic loading experiment to predict the GAG synthesis rate for cells in the IVD or articular cartilage under mechanical loading.

Since the relative volume change of the cells in the tissue is related to the local deformation of the tissue, an optimal loading condition exists in the tissue for cells to exhibit the maximum synthesis activities. For cartilage explants, the unloading condition has been reported to be the optimal loading condition (Kim et al., 1994; Schneiderman et al., 1986), whereas a compressed condition may be the optimal loading condition for IVDs in vitro (Ohshima et al., 1995).

We developed an analytical relationship for relative volume changes between cell and tissue by an approximation method [i.e., eq. (6-5)]. It predicts that the ratio of relative cell volume change to tissue dilatation is in the range of 1.42 to 1.55 for cartilage with 1% - 10% (Stockwell, 1979) of cell volume fraction and under less than 20% tissue deformation (Figure 6-3). The ratio, with 1% of cell volume fraction, changes less than 1% when the Young's modulus of ECM is increased or decreased by 5 times [Figure 6-5 (a)], whereas it changes by -4% to 7% (relative to the value at Poisson ratio equal to 0.04) when the Poisson's ratio varies in the physiological range from 0.0 to 0.1 (Athanasiou et al., 1991) [Figure 6-5 (b)]. This ratio has been found to be 1.0 to 1.2 for articular cartilage experimentally (Guilak et al., 1995), and about 2 by numerically modeling matrix and cell as biphasic materials (Guilak and Mow, 2000). Our result is consistent with these previous findings in the literature, which indicates our eq. (6-5) is reasonably accurate for estimating the relative cell volume change in the tissue at equilibrium state.

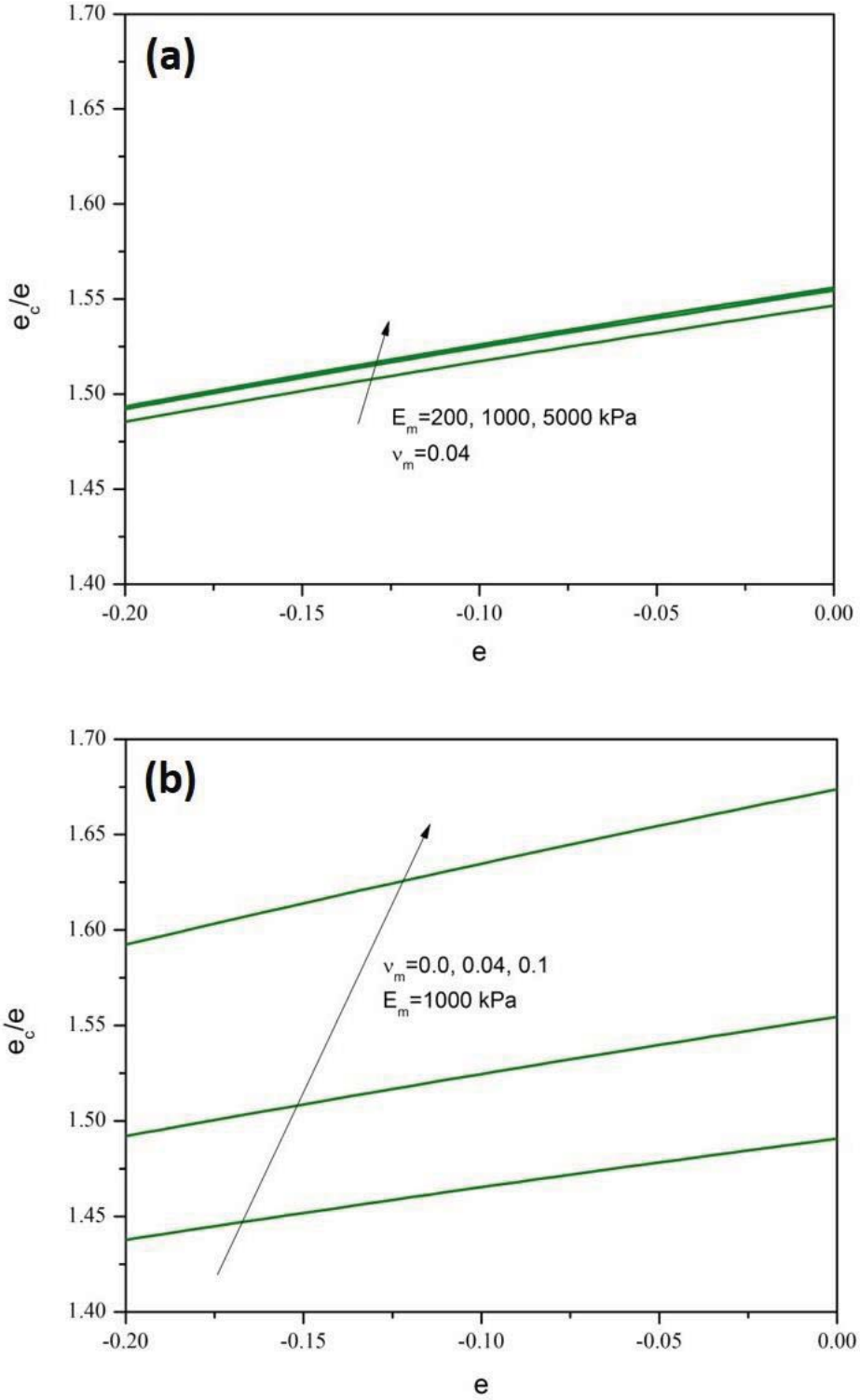

Figure 6-5 The effects of the (a) Young's modulus, and (b) Poisson's ratio of ECM on the ratio of relative cell volume change to tissue dilatation for χ^3=1% .

Notice that eq. (6-5) may not be used to estimate the relative cell volume change in the tissue under dynamic loading conditions because of the fluid pressurization effect (Lee et al., 1981; Soltz and Ateshian, 2000). This fluid pressurization effect will increase the stiffness of the tissue under dynamic loading, and may effectively reduce the tissue deformation. Thus, the deformation of a cartilage explant is smaller at a higher compressive loading frequency than that at a lower loading frequency, provided that the loading amplitude remains the same. Under this loading condition, the cell within the explant will experience smaller deformation at a higher frequency than that at a lower frequency. According to eq. (6-1), the GAG synthesis rate will be higher at a higher loading frequency. This analysis is consistent with the experimental findings on GAG synthesis rate reported in the literature (Sah et al., 1989).

In summary, a new mathematical model has been developed for GAG synthesis rate in cartilaginous tissues and it is able to describe the change of GAG synthesis rate with variations of the osmotic loading or mechanical loading. One can estimate the volume change of cells in a tissue by calculating tissue dilatation (relative to the optimal configuration). Based on this model, the loading applied to a cartilage explant should be reduced if the modulus of the matrix or scaffold is small at an initial stage of a repair or regeneration process in order to maintain cell volume at its optimum condition. One can also use this model to design a bioreactor system with proper extracellular environment or mechanical loading for growing tissue at the maximum rate of extracellular matrix synthesis. Incorporating this mathematical model and our previous developed cell-activity-coupled, mechano-electrochemical theory for cartilaginous tissues (Gu et al., 2014; Zhu et

al., 2014), we can quantitatively investigate the role of mechanical loading in tissue growth or degeneration in cartilaginous tissues.

Chapter 7

Prediction of Glycosaminoglycan Synthesis in the Intervertebral Disc under Mechanical Loads

7.1 Introductory Remarks

The most significant biochemical change in IVD degeneration is the loss of GAG content (Lyons et al., 1981). The loss of GAG directly compromises the disc mechanical roles in the spinal system (Adams et al., 1996; Lyons et al., 1981; Urban and McMullin, 1988; Zhu et al., 2014). Abnormal mechanical loading has been thought to be a major factor that initiates the disc degeneration (Adams and Roughley, 2006; Stokes and Iatridis, 2004; Urban and Roberts, 2003). It has been suggested that cell-mediated remodeling may be the main pathway of disc degeneration initiated by abnormal mechanical loading, aside from the structure failure directly caused by mechanical loading (Setton and Chen, 2006). The mechanism as to how the mechanical loads alter the cell biosynthetic behaviors is still

unknown. This is because many stimuli could be a potential regulator for cell synthetic activities in the disc (Setton and Chen, 2004, 2006; Stokes and Iatridis, 2004).

We have developed a cell volume dependent GAG synthesis theory to characterize the cell biosynthetic behavior in response to mechanical stimuli in Chapter 6. The theory is based on the hypothesis that the change of cell volume is a regulator for downstream posttranslational biosynthesis (Guilak et al., 1995; O'Conor et al., 2014; Wong et al., 1997). The deviation of cell volume from its optimal state was considered as a mechanical stimulus, and it was correlated with the reduction (or decrease) of GAG synthesis rate from its maximum value. This theory has been shown to be able to predict GAG synthesis rate of isolated intervertebral disc cells under different osmotic loading conditions. However, there is no mathematical model available to quantify the variation of GAG synthesis rate within the disc in response to the externally applied mechanical load. The difficulty of developing such a mathematical model lies in the fact that the tissue deformation and the GAG synthesis are two events at different scale levels.

Therefore, the objective of this chapter was to develop a multiscale mathematical model to predict GAG synthesis within disc tissue under mechanical loading. In this study, the mathematical model was first developed and validated with experimental results, then used to investigate the GAG synthesis within the disc subjected to static and diurnal compressions.

7.2 Development of Multiscale Mathematical Model

The multiscale mathematical model was based on cell volume dependent GAG synthesis theory (at the cell level) (Ohshima et al., 1995) and biphasic theory for cartilaginous tissues (at the tissue level) (Mow et al., 1980). In this study, it was assumed that the newly synthesized GAG binds to the solid matrix. Thus, the mass balance equation for GAG can be written as (Ateshian, 2007; Gu et al., 2014; Gu et al., 1998; Lai et al., 1991),

$$\frac{\partial c^{GAG}}{\partial t} + \nabla \cdot (\mathbf{v}^s c^{GAG}) = R^{GAG} \rho^{cell} - T^{GAG} \tag{7-1}$$

where c^{GAG} is the concentration of GAG (per tissue volume), $\mathbf{v}^s$ is the velocity of the solid matrix, R^{GAG} is GAG synthesis rate of each single cell, ρ^{cell} is the cell density (per tissue volume), and T^{GAG} is the breakdown rate of GAG (per tissue volume). Cell density changes with tissue deformation, that is, $\rho^{cell} = \rho_r^{cell} / J$, where ρ_r^{cell} is the cell density at reference state, and J is the volume ratio of tissue. T^{GAG} was assumed to be zero in this study because the turnover time for GAG in the IVD is about 20 years which is much longer than the duration of interest in this study (Roughley, 2004).

The cell volume dependent GAG synthesis theory [eq. (6-1)] developed in Chapter 6 was adopted to model the GAG synthetic behavior of a single cell in response to mechanical stimuli. In this theory, it was assumed that the relative change of GAG synthesis rate (i.e., R^{GAG}) is proportional to the relative cell volume change, and there is an optimal cell volume corresponding to the maximum GAG synthesis rate, mathematically,

$$\frac{R^{GAG}}{R_0^{GAG}} = 1 - \alpha \left| \frac{V^{cell} - V_0^{cell}}{V_0^{cell}} \right|, \tag{7-2}$$

where R_0^{GAG} is the maximum GAG synthesis rate, V^{cell} and V_0^{cell} are the cell volumes at current and optimal state, respectively, and α is a positive parameter characterizing the effect of cell volume change on GAG synthesis rate and it was assumed to be independent of cell volume in this study. The value of α was found to be 2.41 for isolated bovine intervertebral disc cells in Chapter 6, and this value was used in this study. Combining eqs. (7-1) and (7-2) yields,

$$\frac{\partial c^{GAG}}{\partial t} + \nabla \cdot (\mathbf{v}^s c^{GAG}) = Q\left(1 - \beta\left|\frac{V^{cell} - V_0^{cell}}{V_0^{cell}}\right|\right), \tag{7-3}$$

where Q $(= \rho^{cell} R_0^{GAG})$ is the maximum synthesis rate per tissue volume.

In order to evaluate the change of cell volume within the matrix caused by the mechanical loading on the tissue level, a cell-matrix unit approach was adopted, in which a spherical cell is encapsulated in a larger sphere of the ECM, see Figure 7-1. It was assumed that the cell-matrix composite is subjected to a uniformly distributed normal stress at the outer boundary, and the cell and matrix are attached perfectly. Therefore, the relationship between the dilatation of cell, e^c $[= (V^{cell} - V_r^{cell})/V_r^{cell}$, where V_r^{cell} is the cell volume at the reference state], and the dilatation of composite, e $(= J - 1)$, can be established through this unit approach. In this study, we assumed the total cells occupy 1% of the total tissue volume (Bibby et al., 2001; Urban et al., 2000), thus the ratio between cell radius (r^c) and composite radius (r) is 0.215 $(= \sqrt[3]{0.01})$. The cell was modeled as a single phase linear elastic material and the matrix was modeled as a biphasic material [eqs. (3-1) and (3-2)]. A hydration dependent hydraulic permeability model [eq. (3-10)] was adopted for disc tissue (Gu et al., 2003).

The stress of the mixture is contributed by both solid and fluid phases. Under a finite deformation, the stress of the solid matrix can be evaluated through, $\boldsymbol{\sigma}^s = \frac{2}{J}\mathbf{F}\frac{\partial \psi}{\partial \mathbf{C}}\mathbf{F}^T$, where $\mathbf{F}$ is the deformation gradient tensor, $J = \det(\mathbf{F})$, and $\mathbf{C} = \mathbf{F}^T\mathbf{F}$. A strain energy density function for hyperelastic compressible materials was adopted for modeling the disc tissue (Ehlers and Eipper, 1999), which states,

$$\psi = \frac{\mu}{2}(I_1 - 3) - \mu \ln J + \lambda(\phi_r^w)^2 \left[\frac{J-1}{\phi_r^w} - \ln(\frac{J-1}{\phi_r^w} + 1) \right], \tag{7-4}$$

where λ and μ are two Lamé constants, I_1 is the first invariant of $\mathbf{C}$, and ϕ_r^w is the fluid volume fraction at the reference state and it is related to the fluid volume fraction at current state through, $\phi^w = \left(\phi_r^w + J - 1\right)/J$.

7.3 Numerical Examples

This multiscale mathematical model was applied to study GAG synthesis in the live bovine tail IVD (Ohshima et al., 1995). The IVD was modeled as concentric cylinders with 6.0 mm in height. The core is nucleus pulposus (NP) with 5.5 mm in radius, and the outer layer is annulus fibrosus (AF) with 5.5 mm in radial thickness. The AF was divided into inner AF and outer AF with equal radial thickness, i.e., 2.75 mm each, see Figure 7-1 (Ohshima et al., 1995). Only one-eighth of the disc was used in the numerical simulation because of the axial-symmetry of the disc geometry (Figure 7-1). Finite element method was used to discretize the mathematical model following the approach in (Sun et al., 1999), and it was implemented in COMSOL. The biphasic material properties of the tissue and cell used in this study were listed in Table 7-1.

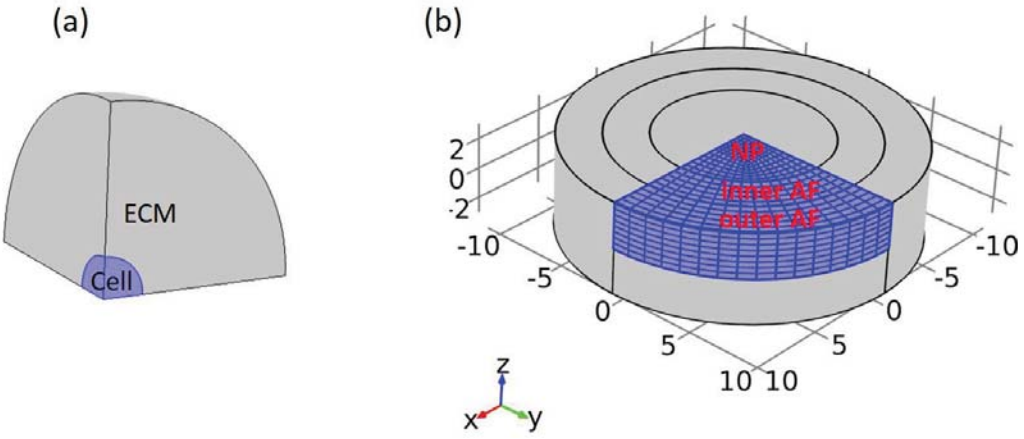

Figure 7-1 Schematics of (a) cell-matrix unit; (b) bovine tail IVD. Scale unit in mm.

Table 7-1 Material properties for finite element analysis.

	NP#	**AF#**	**Cell***
λ	0.04 MPa	0.14 MPa	1.29 kPa
μ	0.13 MPa	0.30 MPa	0.32 kPa
ϕ_r^w	0.89	0.76	N/A
k	$a = 0.04\times10^{-16}\,\mathrm{m}^4/(\mathrm{N}\cdot\mathrm{s})$ $b = 2.283$	$a = 0.18\times10^{-16}\,\mathrm{m}^4/(\mathrm{N}\cdot\mathrm{s})$ $b = 3.125$	N/A

#The ECM of NP and AF were modeled as biphasic material (Farrell and Riches, 2013; Iatridis and ap Gwynn, 2004; Ohshima et al., 1995; Perie et al., 2005).
*The cell was modeled as linear elastic material (Cao et al., 2011).

Several assumptions were made in the numerical model in order to compare our model prediction with experimental results by Ohshima et al's study (Ohshima et al., 1995) : (1) the strain state under in-vivo loading condition was assumed to be an optimal condition for GAG synthesis in which its synthesis rate reaches a maximum value (Bayliss et al., 1986; Ishihara et al., 1997; Schneiderman et al., 1986), (2) the variation of maximum GAG synthesis rate in the axial direction was assumed to be negligible, (3) the variation of GAG content had no effect on mechanical properties, and (4) the maximum GAG synthesis rate per tissue volume (i.e., Q in eq. (7-3)) was assumed to be uniform in the NP and linearly varied from inner AF to outer AF as suggested by experimental findings (Bayliss et al., 1988; Bayliss et al., 1986; Oshima et al., 1993).

In Ohshima et al's study, the discs were undergone with unconfined compression creep tests with a constant load of 4.9 N, 49.0 N, 98.0 N, or 147.0 N for 8 hours, and GAG content synthesized (amount of incorporated ^{35}S-sulfate) per tissue weight during the eight hours creep process was measured (Ohshima et al., 1995). In order to compare predicted results and experimental results, the unit of GAG content in mole per tissue volume was converted to be in mole per tissue weight by scaling tissue mass density (ρ^{tissue}) of 1.04 g/cm^3 for NP and 1.10 g/cm^3 for AF (Gu et al., 1996).

The in-vivo strain state (i.e., the optimal state) in the bovine tail disc was determined by adjusting in-vitro compressive loads on the disc until the simulated overall water content in NP reached the value in vivo (i.e., $\phi^w = 0.86$) at the end of 8-hour creep test. The cell volume change (with respect to the cell volume in the optimal state) was calculated based

on the local tissue dilation. The spatial distributions of maximum GAG synthesis rate per unit tissue volume (Q) in eq. (7-3) was determined by curve-fitting the distributions of the synthesized GAG content in the disc subjected to the 49.0 N compressive load in 8 hours (only the medial to dorsal experimental results were used in the curve-fitting due to the axial-symmetry assumption) (Ohshima et al., 1995). The model validation was conducted by comparing model predictions of GAG content distribution in the disc with those measured at 4.9 N, 98.0 N, and 147.0 N compressive loads.

The effects of different mechanical loading conditions on the GAG synthesis were investigated with this model, including one static compression (0.2 MPa) and two dynamic compressions with diurnal loads (0.15/0.25 MPa and 0.1/0.3 MPa in 12/12 hours shift). For the dynamic loading cases, the disc was compressed for two diurnal cycles under each loading condition, the first cycle was a preconditioning cycle and the GAG content synthesized during the second cycle was used to investigate the effects of different loading regimes on GAG synthesis.

7.4 Results

The relationship between cell dilatation and the dilation of cell-matrix composite were determined with the cell-matrix unit approach, see Figure 7-1. The relationships were similar for both the NP and AF regions. The cell dilatation was about two times larger than the dilatation of the cell-matrix composite (Figure 7-2).

The creep processes in bovine tail IVD under various compressive loads (from 0 to 150 N) were simulated. The water content averaged over the NP region was evaluated at the end of 8-hour creep process, which decreased from 0.89 to 0.82 with increasing the compressive load, see Figure 7-3. The predicted water contents under various compressive loads were in agreement with the experimentally measured results (Ohshima et al., 1995). At the end of 8-hour creep process, the strain in the disc under 58.8 N was chosen as the in-vivo loading condition (i.e., optimal state) because the water content averaged over the NP region at this condition equaled to the in-vivo water content ($\phi^w = 0.86$).

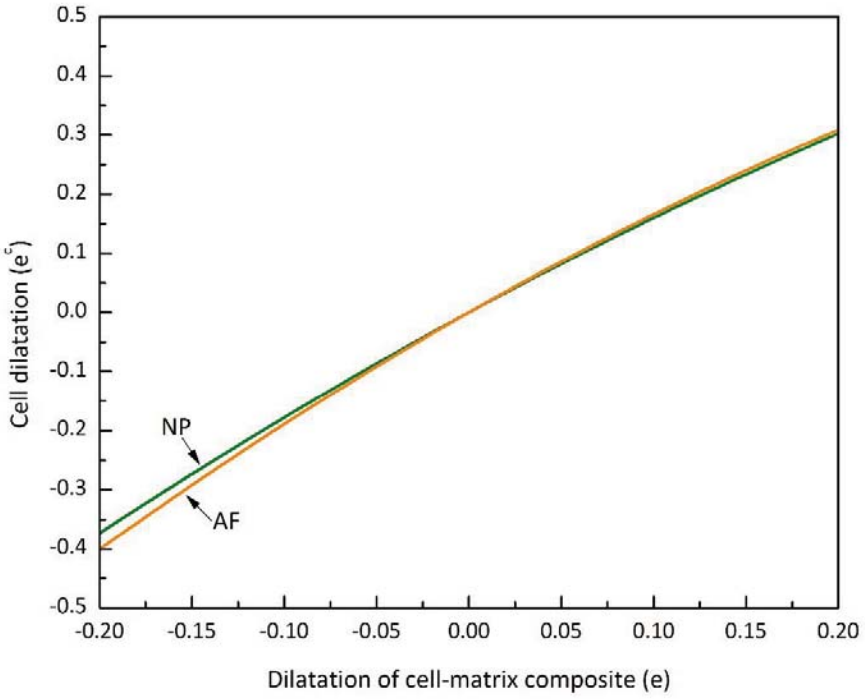

Figure 7-2 Relationship of the dilatations between cell-matrix composite (e) and cell (e^c).

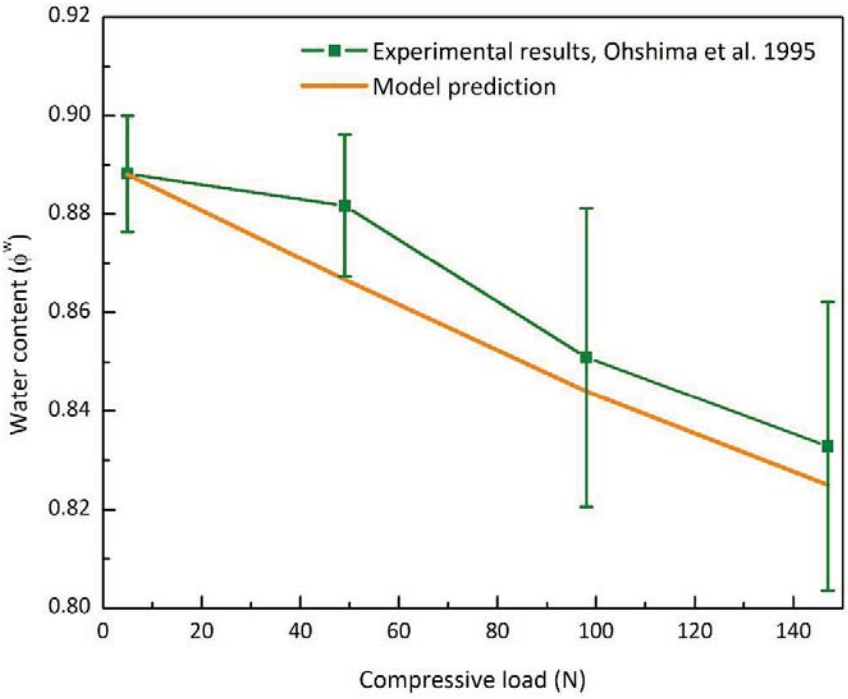

Figure 7-3 Effect of mechanical loading on the water content averaged over NP.

The spatial distribution of maximum GAG synthesis rate was obtained by curve-fitting (R^2=0.94) the measured GAG content (per tissue weight) from the experimental results under 49.0 N compressive load, see Figure 7-4. Note that only the experimental results from medial to dorsal were used in curve-fitting because it was assumed that the bovine tail disc is axial-symmetric in this study. Then, the GAG content synthesized during the 8-hour creep process under 4.9 N, 98.0 N, and 147.0 N were predicted with the multiscale mathematical model. The predictions were in the range of experimental results, see Figure 7-5. The predicted GAG synthesis rate averaged over NP, inner AF, and outer AF were shown in Figure 7-6, respectively. The GAG synthesis rate in discs under 4.9 N and 49.0

N increased with time while the rate in the discs under 98.0 N and 147.0 N first increased then decreased with time,see Figure 7-6.

Spatial distributions of GAG content synthesized under static and diurnal loading conditions were predicted to be similar, with highest GAG content at the interface of AF and NP and decreasing toward the central NP and outer AF. The GAG content synthesized in the NP during a diurnal cycle with 0.1/0.3 MPa and 0.15/0.25 MPa diurnal loads was about 5% lower and 4% higher than the GAG content synthesized with a 0.2 MPa static load, respectively (Figure 7-7). The GAG contents synthesized in the AF during a diurnal cycle were similar to that with a 0.2 MPa static load and 0.1/0.3 MPa diurnal loads, which was about 12% lower than the synthesized GAG content under 0.15/0.25 MPa diurnal load, see Figure 7-7.

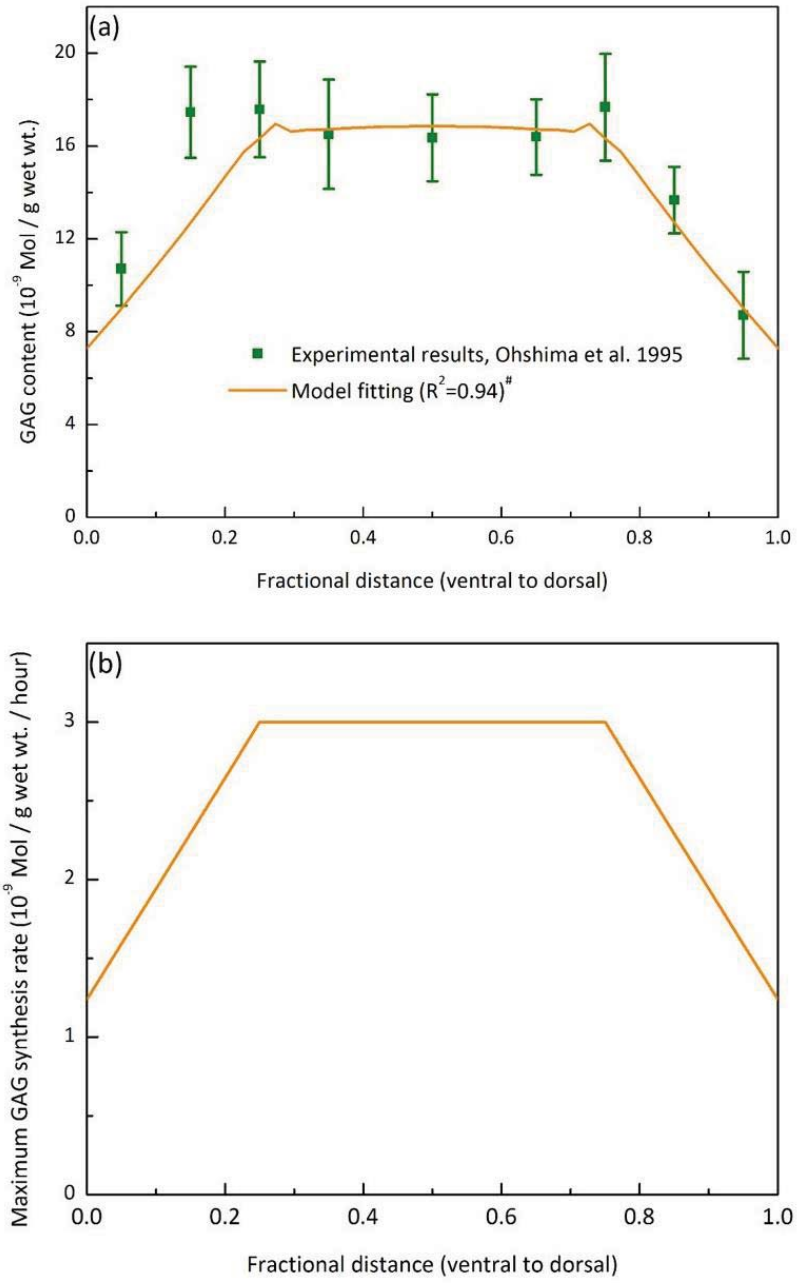

Figure 7-4 (a) Curve-fitting of experimental results of the synthesized GAG content under 49.0 N compressive load. #R2 was calculated with the experimental results from medial to dorsal. (b) Maximum GAG synthesis rate (per tissue weight) yielded from curve-fitting in (a). GAG content refers to the amount of newly synthesized GAG per tissue weight over a period of 8 hours.

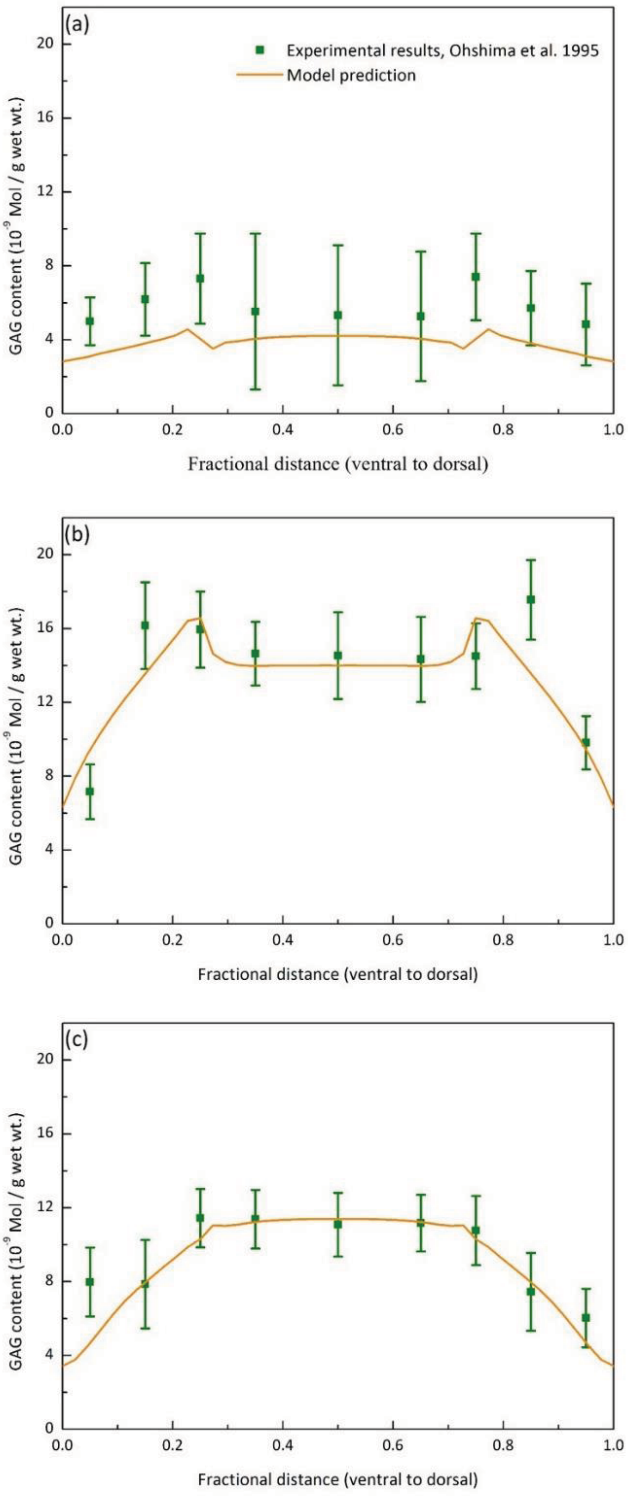

Figure 7-5 Model predictions of synthesized GAG content over 8-hour creep process under (a) 4.9 N; (b) 98.0 N; (c) 147 N compressive load. GAG content refers to the amount of newly synthesized GAG per tissue weight over a period of 8 hours.

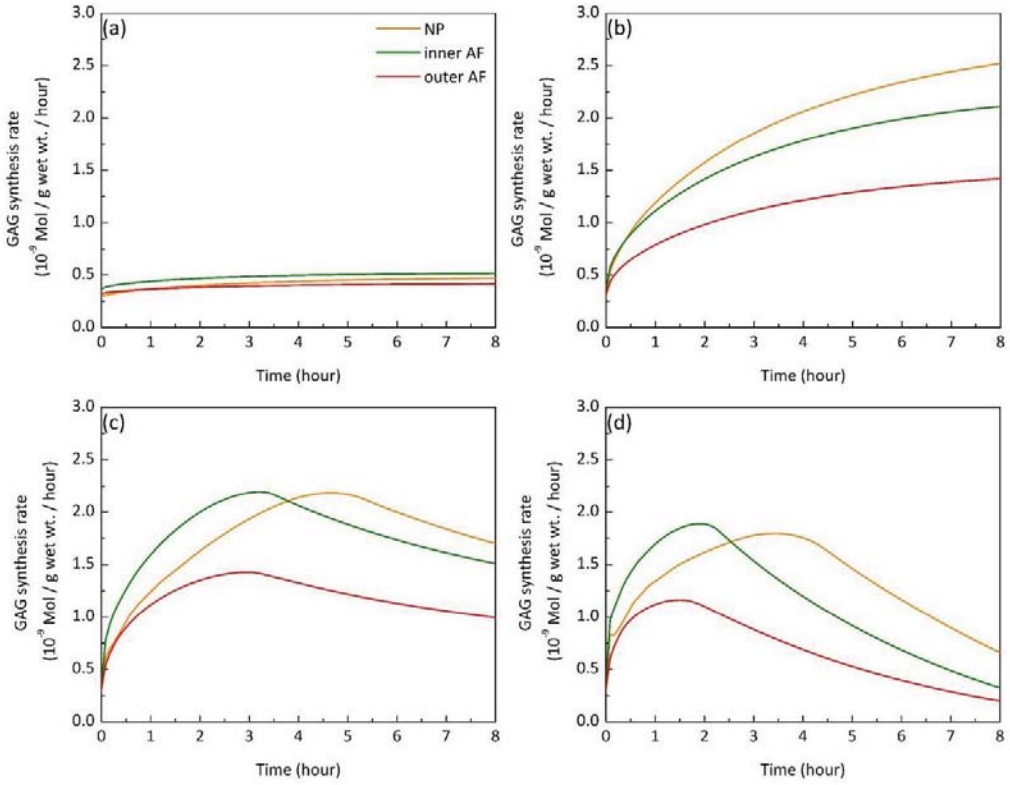

Figure 7-6 Model prediction of GAG synthesis rate under (a) 4.9 N; (b) 49.0 N; (c) 98.0 N; (d) 147.0 N compressive loads.

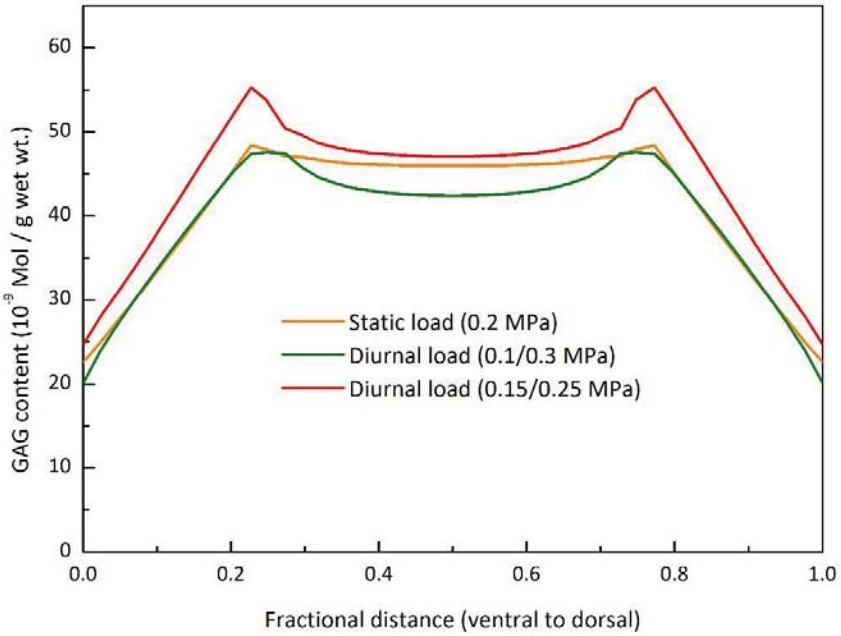

Figure 7-7 Comparison of synthesized GAG contents under diurnal and static loading conditions. Only GAG contents synthesized during the second loading cycle (i.e., 24-48 hours) were compared.

7.5 Discussions

The primary goal of this study was to develop a multiscale mathematical model to predict the effect of mechanical loading on the GAG synthesis within the IVD. This multiscale mathematical model is based on the cell volume dependent GAG synthesis theory developed in Chapter 6 that predicts the variation of GAG synthesis rate of a cell under the influence of a mechanical stimulus, and the biphasic theory (Mow et al., 1980) that predicts the tissue deformation of IVD under mechanical loading. These two theories describe two different (biological and mechanical) phenomena at different scale levels (cell level and tissue level) were coupled together with a cell-matrix unit approach which establishes a relationship between GAG synthesis rate and local tissue volume change.

In the cell volume dependent GAG synthesis theory, the variation of GAG synthesis rate is correlated with the variation of cell volume. The mechanism by which disc cell volume change is correlated with the GAG synthesis rate is currently unclear. This unknown mechanism is related to the positive parameter α in eq. (7-2), which was assumed to be independent of cell volume in this study. The model prediction is sensitive to the value of α as GAG synthesis rate is proportional to its value [see eq. (7-2)]. The value of α has been found to be 2.41 for isolated bovine NP cells under osmotic loading in Chapter 6, and this value was also found to work for both bovine NP and AF cells resided within the ECM in this studies.

Both solid matrix of NP and AF were modeled as isotropic hyperelastic materials in this study. The water contents predicted with the biphasic theory are within the range of experimental measurements (Figure 7-3), which indicates that the biphasic finite element model is able to predict the tissue volumetric strain (i.e., tissue dilatation). It is important to note that the effect of GAG content change on ECM material properties must be taken into consideration when this multiscale mathematical model is used to predict GAG synthesis over a long period of time. This is because the GAG has a remarked contribution to the effective mechanical properties of connective tissues (Canal Guterl et al., 2010; Lai et al., 1991).

The ratio of cell dilatation to tissue dilatation was evaluated with finite element method based on an idealized morphology in this study, but the ratio is comparable with that evaluated with finite element method based on a real cell morphology (Cao et al., 2011).

In this study, the ratio was evaluated at a static (or equilibrium) state with the cell-matrix unit, which is different from creep and diurnal loading conditions. However, this difference in loading condition will have a very limited influence on the prediction of GAG synthesis. This is because the characteristic time (or diffusion time, $t = h^2 / [(\lambda + 2\mu)k]$, where h is the characteristic length of the unit) for the cell-matrix unit is in the magnitude of seconds, which is much smaller than the characteristic time of creep and diurnal loading (Gao and Gu, 2014). In the above analysis, the mechanical and transport properties of the matrix instead of equivalent properties of the cell-matrix unit were used in the estimation because the cell volume fraction is only about 1%. Note that this relationship cannot be used if the IVD is under dynamical loading with frequency higher than 0.01 Hz, because the diffusion time is comparable with the period of dynamical loading, thus the fluid flow will have a significant effect on the deformation of cell (Kim et al., 2008; Soltz and Ateshian, 2000).

The maximum GAG synthesis rates fitted by the multiscale mathematical model averaged over NP, inner AF, and outer AF were about 3.0, 2.6, and 1.7 $\times 10^{-9}$ mol/ g wet wt./hour, respectively (Figure 7-4), which are comparable with GAG synthesis rates measured in vitro with tissue samples from human IVD and bovine tail IVD (Bayliss et al., 1988; Oshima et al., 1993) . The content of GAG synthesized during the creep processes predicted by the multiscale mathematical model were in the range of experimental measurements (Figure 7-5). The model is also capable of predicting the higher GAG content at the interface between AF and NP, which is consistent with experimental findings (Ohshima et al., 1995), see Figures 7-4 (a) and 7-5. The synthesized GAG content depends on both

maximum GAG synthesis rate (Q) and the dilatation of cell (or the dilatation of tissue) as shown in eq. (7-3). Since the maximum GAG synthesis rate was assumed to be uniform in the NP [Figure 7-4 (b)], the higher synthesized GAG content at the interface between AF and NP is due to the inhomogeneous dilatation in the NP. This inhomogeneous dilatation is caused by the constrained effect of the AF.

The GAG synthesis rate predicted by the multiscale mathematical model was shown to depend on loading magnitude, loading duration, and the anatomic region (Figure 7-6), which is in accordance with the experimental findings (Chan et al., 2011; Lotz, 2004; Setton and Chen, 2004, 2006; Stokes and Iatridis, 2004). The temporal variation of GAG synthesis rate depends on the tissue strain. The synthesis rate increases when the tissue strain approaching the strain at optimal state, and it decreases when the tissue strain deviates from the strain at optimal state. The GAG synthesis rate in the outer AF was found to be the lowest compared with that in NP and inner AF, which is consistent with experimental findings (Horner et al., 2002).

Several assumptions have been made in the model development and numerical simulation, which may affect the prediction. Firstly, we assumed the mechanical properties are nonlinear and isotropic for AF, which differs from its anisotropic nature. This assumption would affect the predicted cell dilatation and resultantly affect predicted GAG content in the AF. Secondly, we assumed the disc is perfectly axial-symmetric in all aspects (e.g., geometry, material properties, and cellular metabolic activities) in the numerical simulation, and only the experimental results from median to dorsal disc were used in the curve-fitting,

thus the model prediction matches better with experimental results at the dorsal AF than that at the ventral AF [Figures 7-4 (a) and 7-5]. Thirdly, we assumed the newly synthesized GAG binds to the extracellular matrix without considering the diffusion of GAG within the disc and release of GAG to the culture medium (Korecki et al., 2007), this assumption may not affect predicted GAG content significantly because the GAG diffusivity in the tissue is very low [about 5×10^{-8} mm^2/s (Nims et al., 2014)] and its diffusion length (0.05 mm) in 8 hours is much smaller than the length scale of the disc. Fourthly, we assumed the maximum GAG synthesis rate linearly varies from inner AF to outer AF, which may differ from that in the real situation and affects the predicted results. This assumption may be a factor causing a discrepancy between model prediction and experimental result in the AF [Figures 7-4 (a) and 7-5].

It was found that static loading and diurnal loading have different effects on the content of synthesized GAG (within the same time period), and the effects of diurnal loading depend on the amplitude of the load (Figure 7-7). The difference in synthesized GAG content between 0.2 MPa static load and 0.1/0.3 MPa diurnal loads is small (primarily in the NP), which agrees with experimental findings (Korecki et al., 2007). The higher GAG content synthesized with 0.15/0.25 MPa diurnal loads indicates that mechanical loading plays an important role in maintaining ECM integrity.

In summary, a multiscale mathematical model was developed to predict the GAG synthetic activity within IVD under mechanical loading. The robustness of the model was demonstrated by the agreement between predicted results and experimental results. The

model is important to understand the effect of mechanical loading at the tissue level on GAG synthesis at the cellular level. This model is also important for designing loading strategies to grow tissue in tissue engineering.

Chapter 8

Summary and Recommendations for Future Work

8.1 Summary

The degeneration of lumbar IVDs has been implicated as a possible cause of low back pain which affects more than 600 millions of people worldwide. Abnormal mechanical loading is thought to be a primarily etiological factor leading to degenerative changes to discs. The disc structures may fail under abnormal mechanical loading, which would result in the disc degeneration. Moreover, the balance between the synthesis and breakdown of extracellular matrix components may be disturbed under abnormal mechanical loading, which would cause disc degeneration through a cell-mediated remodeling pathway. Despite this, there is a lack of approach to quantify the abnormal mechanical loading, and there is a lack of knowledge on how the cell perceives and responds to the extracellular mechanical stimuli. Therefore, the objectives of this dissertation were twofold: (1) to develop biomechanical models to characterize disc biomechanical behaviors; and (2) to develop mechanobiological models to characterize the responses of cellular biosynthetic behaviors to mechanical stimuli. In order to achieve these research objectives, five studies (Chapter

3 to Chapter 7) were carried out in this dissertation, and the important findings of each study are summarized below.

In Chapter 3, a new constitutive model for hydration-dependent aggregate modulus of hydrated and soft materials was derived based on the biphasic theory and transport models, that is, $H_A = A(1-\phi^w)^b(\phi^w)^{2-b}/(2-\phi^w)^2$, where H_A $(=\lambda+2\mu)$ is the aggregate modulus, ϕ^w is the volume fraction of fluid (i.e., hydration), A and b (>2) are two parameters related to the transport properties of the biphasic materials. A linear model for hydration-dependent shear modulus in the literature was verified for hydrogels. The effects of tissue hydration on mechanical properties (aggregate modulus and Poisson's ratio) were investigated. It was found that the value of Poisson's ratio is very sensitive to the tissue hydration in soft materials with high water content. The predictions of the aggregate modulus and shear modulus for hydrogels by the model compared well with those from experimental results. This study is important for developing new techniques for noninvasively assessing the mechanical properties of biological soft tissues using quantitative MRI methods as well as for designing scaffolds with proper mechanical properties for tissue engineering applications. This study is also very important in modeling the long-term degeneration of IVD because this study provides constitutive models to characterize the alteration of mechanical properties during disc degeneration.

In Chapter 4, a more realistic anisotropic multiphysics model was developed based on the continuum mixture theory and employed to characterize the nonlinear coupling phenomena among anisotropic and large solid deformation, anisotropic transport of

interstitial water and solutes, and the electro-osmotic effect in the IVD. Numerical simulations demonstrated that this model is capable of systematically predicting the mechanical and electrochemical signals within the disc under various loading conditions, which is essential in understanding the biomechanics and mechanobiology of IVDs.

In Chapter 5, a computational model was developed to investigate the initiation and propagation of damage in the AF. The computational model was based on the anisotropic multiphysics model for IVDs developed in Chapter 4 and a continuum damage model. The initiation and propagation of damage in the AF under compression (up to 2000 N), flexion (up to 11°), and compression (450 N)-flexion (up to 11°) were simulated. The simulation results showed that the damage initiates in different regions under different mechanical loading conditions. The posterior AF was shown to be more susceptible to structure failure as it damages under all the three loading conditions. The damage in the posterior AF could initiate in the outer, middle, and inner regions. It has been found that circumferential damages could evolve into radial damages. The damages under compression-flexion could provide a pathway for the nucleus pulposus (NP) to migrate into the AF. The computational model developed in this study is important in quantifying the abnormal mechanical loading and preventing the damage to the disc.

In Chapter 6, a mechanobiology mathematical model to quantitatively describe the cell volume dependent GAG synthesis rate in the cartilaginous tissues was developed. This model was developed based on the hypothesis that the change of cell volume is a primary mechanism for cells to perceive the mechanical stimuli, and also based on experimental

findings that the maximum synthesis rate of GAG is achieved at an optimal cell volume, larger or smaller than this level the GAG synthesis rate decreases. Using this model, we investigated the effects of osmotic loading and mechanical loading on GAG synthesis rate. It was found our proposed mathematical model is able to well describe the change of GAG synthesis rate in isolated cells and in cartilage with variations of the osmotic loading or mechanical loading. This model is important for evaluating the GAG synthesis activity within cartilaginous tissues as well as understanding the role of mechanical loading in tissue growth or degeneration. It is also important for designing a bioreactor system with proper extracellular environment or mechanical loading for growing tissue at the maximum synthesis rate of the extracellular matrix.

In Chapter 7, a multiscale mathematical model was developed to quantify the effect of mechanical loading on GAG synthesis. This model was based on the cell volume dependent GAG synthesis theory developed in Chapter 6 and the biphasic theory. The GAG synthesis (at the cell level) was coupled with the mechanical loading (at the tissue level) via a cell-matrix unit approach which established a relationship between the variation of cell volume and the local tissue volume change. This multiscale mathematical model was used to predict the effect of static load (creep load) on GAG synthesis in bovine tail discs. The predicted results are in the range of experimental results. This model was also used to investigate the effect of static (0.2 MPa) and diurnal loads (0.1/0.3 MPa and 0.15/0.25 MPa in a 12/12 hours shift) on GAG synthesis. It was found that static load and diurnal loads have different effects on GAG synthesis in a diurnal cycle, and the diurnal load effects depend on the amplitude of the load. The model is important to understand the effect of

mechanical loading at the tissue level on GAG synthesis at the cellular level, as well as to optimize the mechanical loading in growing engineered tissue.

In summary, mathematical models have been developed and validated to quantitatively describe the biomechanical behaviors of the IVD and the cellular biosynthetic responses to mechanical stimuli in this dissertation. These mathematical models provide numerical approaches to quantify the abnormal mechanical loading which may cause disc degeneration. These mathematical models are important in understanding the etiology of disc degeneration, as well as in preventing and treating disc degeneration.

8.2 Recommendations for Future Work

A series of biomechanics and mechanobiology mathematical models have been developed in this dissertation. Applying these mathematical models in understanding, preventing, and treating disc degeneration is the recommendations for the future work. More specifically, three future works are recommended:

(1) **Applying these mathematical models to understand disc degeneration.** The disc degeneration is a slow and long-term process, thus it is difficult to investigate the degeneration process with experimental approaches. These mathematical models could be used in simulating the whole disc degeneration process caused by abnormal mechanical loading, with which the spatiotemporal variation of disc composition, extracellular signals, and overall disc biomechanical functions could be quantified. These quantitative information would enhance our understanding of

disc degeneration caused by abnormal mechanical loading. Moreover, these mathematical models could be combined with the cell-activity-coupled mechano-electrochemical continuum mixture theory (Gu et al., 2014) developed by our research group to investigate the non-genetic factors causing disc degeneration.

(2) **Quantifying abnormal mechanical loading.** These mathematical models could be used to estimate if a mechanical loading condition would initiate disc degeneration. This application is especially valuable in preventing disc degeneration caused by occupational factors (Battie et al., 2007).

(3) **Applying these mathematical models in treating disc degeneration.** These mathematical models could be used to predict the disc degeneration with patient-specific information, such as disc geometry measured from MRI. This application would help doctors to design an appropriate treatment strategy, and estimate the treatment outcome of some therapies, such as physical therapy. These mathematical models also could be used to design scaffolds and loading regimes to grow engineered disc tissue to treat degenerated discs.

Appendix

We use a one-dimensional (in the x-direction) water diffusion case to show that the D defined in eq. (3-7) is the mutual diffusion coefficient of water. In this one-dimensional case, a water chamber is divided by a hydrogel specimen into the upstream and downstream compartments. Let us assume there is a difference in water concentration between the two compartments, but no difference in hydrostatic pressure between the upstream and downstream compartments (there may exist a pressure gradient within the hydrogel specimen during the diffusion process). Based on Fick's law, the water volume flux in the x-direction (J_x^w) in the specimen may be expressed as

$$J_x^w = -D^w \vartheta \frac{\partial c^w}{\partial x} \ , \tag{A1}$$

where D^w is the mutual diffusion coefficient of water, ϑ is the partial volume of water, and c^w is the molar concentration of water (per mixture volume). It follows from eqs. (3-2) and (3-3) that:

$$\frac{\partial p}{\partial x} = H_A \frac{\partial e}{\partial x} \ , \tag{A2}$$

where $e = \frac{\partial u}{\partial x}$ for this one-dimensional case, and u is the displacement in the x-direction. Based on Darcy's law, i.e., eq. (3-4), we also have,

$$J_x^w = -k \frac{\partial p}{\partial x} \ . \tag{A3}$$

Combining eqs. (A1-A3), we have:

$$D^w \vartheta \frac{\partial c^w}{\partial x} = H_A k \frac{\partial e}{\partial x} \ . \tag{A4}$$

Since the specimen is assumed to be saturated and intrinsically incompressible, the relative volume change (i.e., dilation, e) at any point within the gel is due to the change in water volume. Thus, if the deformation is infinitesimal, we obtain:

$$e = \vartheta (c^w - c_r^w) \ , \tag{A5}$$

where c_r^w is the water concentration at $e = 0$. From eqs. (A4) and (A5), we can show that the D defined in eq. (3-7) is the mutual diffusion coefficient of water, i.e.,

$$D^w = D = H_A k \ . \tag{A6}$$

Bibliography

Acaroglu, E.R., et al., 1995. Degeneration and aging affect the tensile behavior of human lumbar anulus fibrosus. Spine (Phila Pa 1976) 20, 2690-2701.

Adams, M.A., et al., 2000. Mechanical initiation of intervertebral disc degeneration. Spine 25, 1625-1636.

Adams, M.A., Hutton, W.C., 1982a. The mechanics of prolapsed intervertebral disc. Int Orthop 6, 249-253.

Adams, M.A., Hutton, W.C., 1982b. Prolapsed intervertebral disc. A hyperflexion injury 1981 Volvo Award in Basic Science. Spine (Phila Pa 1976) 7, 184-191.

Adams, M.A., et al., 1996. 'Stress' distributions inside intervertebral discs - The effects of age and degeneration. J Bone Joint Surg Br 78b, 965-972.

Adams, M.A., Roughley, P.J., 2006. What is intervertebral disc degeneration, and what causes it? Spine 31, 2151-2161.

Adams, P., Muir, H., 1976. Qualitative changes with age of proteoglycans of human lumbar disks. Ann Rheum Dis 35, 289-296.

Agoras, M., Castaneda, P.P., 2014. Anisotropic finite-strain models for porous viscoplastic materials with microstructure evolution. Int J Solids Struct 51, 981-1002.

Allan, D.B., Waddell, G., 1989. An historical perspective on low back pain and disability. Acta Orthopaedica Scandinavica 60, 1-23.

Annunen, S., et al., 1999. An allele of COL9A2 associated with intervertebral disc disease. Science 285, 409-412.

Antoniou, J., et al., 1996. The human lumbar intervertebral disc - Evidence for changes in the biosynthesis and denaturation of the extracellular matrix with growth, maturation, ageing, and degeneration. J Clin Invest 98, 996-1003.

Aoki, T., et al., 2012. Correlation between apparent diffusion coefficient and viscoelasticity of articular cartilage in a porcine model. Skeletal Radiol 41, 1087-1092.

Argoubi, M., ShiraziAdl, A., 1996. Poroelastic creep response analysis of a lumbar motion segment in compression. J Biomech 29, 1331-1339.

Armstrong, C.G., Mow, V.C., 1982. Variations in the intrinsic mechanical properties of human articular cartilage with age, degeneration, and water content. J Bone Joint Surg Am 64, 88-94.

Ateshian, G.A., 2007. On the theory of reactive mixtures for modeling biological growth. Biomech Model Mechan 6, 423-445.

Ateshian, G.A., et al., 2006. A mixture theory analysis for passive transport in osmotic loading of cells. J Biomech 39, 464-475.

Athanasiou, K.A., et al., 1994. Comparative study of the intrinsic mechanical properties of the human acetabular and femoral head cartilage. J Orthop Res 12, 340-349.

Athanasiou, K.A., et al., 1991. Interspecies comparisons of in situ intrinsic mechanical properties of distal femoral cartilage. J Orthop Res 9, 330-340.

Aultman, C.D., et al., 2005. The direction of progressive herniation in porcine spine motion segments is influenced by the orientation of the bending axis. Clin Biomech 20, 126-129.

Ayotte, D.C., et al., 2000. Direction-dependent constriction flow in a poroelastic solid: The intervertebral disc valve. J Biomech Eng-T Asme 122, 587-593.

Ayotte, D.C., et al., 2001. Direction-dependent resistance to flow in the endplate of the intervertebral disc: an ex vivo study. J Orthopaed Res 19, 1073-1077.

Baer, A.E., et al., 2003. The micromechanical environment of intervertebral disc cells determined by a finite deformation, anisotropic, and biphasic finite element model. J Biomech Eng 125, 1-11.

Baer, A.E., Setton, L.A., 2000. The micromechanical environment of intervertebral disc cells: effect of matrix anisotropy and cell geometry predicted by a linear model. J Biomech Eng 122, 245-251.

Balzani, D., et al., 2006. Simulation of discontinuous damage incorporating residual stresses in circumferentially overstretched atherosclerotic arteries. Acta Biomater 2, 609-618.

Battie, M.C., et al., 2007. Occupational and genetic risk factors associated with intervertebral disc disease. Spine 32, 2926-2926.

Bayliss, M.T., et al., 1988. 1988 Volvo award in basic science. Proteoglycan synthesis in the human intervertebral disc. Variation with age, region and pathology. Spine (Phila Pa 1976) 13, 972-981.

Bayliss, M.T., et al., 1986. In vitro method for measuring synthesis rates in the intervertebral disc. J Orthop Res 4, 10-17.

Belytschko, T., et al., 1974. Finite element stress analysis of an intervertebral disc. J Biomech 7, 277-285.

Benzeev, A., 1991. Animal cell shape changes and gene expression. Bioessays 13, 207-212.

Best, B.A., et al., 1994. Compressive mechanical properties of the human anulus fibrosus and their relationship to biochemical composition. Spine 19, 212-221.

Bibby, S.R., Urban, J.P., 2004. Effect of nutrient deprivation on the viability of intervertebral disc cells. Eur Spine J 13, 695-701.

Bibby, S.R.S., et al., 2001. The pathophysiology of the intervertebral disc. Joint Bone Spine 68, 537-542.

Boos, N., et al., 1993. Quantitative MR imaging of lumbar intervertebral disks and vertebral bodies: influence of diurnal water content variations. Radiology 188, 351-354.

Broberg, K.B., 1983. On the mechanical behavior of intervertebral disks. Spine 8, 151-165.

Brodin, H., 1955. Paths of nutrition in articular cartilage and intervertebral discs. Acta Orthop Scand 24, 177-183.

Brown, T., et al., 1957. Some mechanical tests on the lumbosacral spine with particular reference to the intervertebral discs: A preliminary report. J Bone Joint Surg Am 39, 1135-1164.

Bush, P.G., Hall, A.C., 2001. The osmotic sensitivity of isolated and in situ bovine articular chondrocytes. J Orthopaed Res 19, 768-778.

Canal Guterl, C., et al., 2010. Electrostatic and non-electrostatic contributions of proteoglycans to the compressive equilibrium modulus of bovine articular cartilage. J Biomech 43, 1343-1350.

Cao, L., et al., 2007. Three-dimensional morphology of the pericellular matrix of intervertebral disc cells in the rat. J Anat 211, 444-452.

Cao, L., et al., 2011. Three-dimensional finite element modeling of pericellular matrix and cell mechanics in the nucleus pulposus of the intervertebral disk based on in situ morphology. Biomech Model Mechanobiol 10, 1-10.

Cassidy, J.J., et al., 1989. Hierarchical structure of the intervertebral disc. Connect Tissue Res 23, 75-88.

Chahine, N.O., et al., 2004. Anisotropic strain-dependent material properties of bovine articular cartilage in the transitional range from tension to compression. J Biomech 37, 1251-1261.

Chan, S.C.W., et al., 2011. The effects of dynamic loading on the intervertebral disc. Eur Spine J 20, 1796-1812.

Chen, A.C., et al., 2001. Depth- and strain-dependent mechanical and electromechanical properties of full-thickness bovine articular cartilage in confined compression. J Biomech 34, 1-12.

Chiu, E.J., et al., 2001. Magnetic resonance imaging measurement of relaxation and water diffusion in the human lumbar intervertebral disc under compression in vitro. Spine (Phila Pa 1976) 26, E437-444.

Clague, D.S., et al., 2000. Hydraulic permeability of (un)bounded fibrous media using the lattice Boltzmann method. Phys Rev E 61, 616-625.

Cortes, D.H., et al., 2014. Elastic, permeability and swelling properties of human intervertebral disc tissues: A benchmark for tissue engineering. Journal of Biomechanics 47, 2088-2094.

Costi, J.J., et al., 2008. Frequency-dependent behavior of the intervertebral disc in response to each of six degree of freedom dynamic loading - Solid phase and fluid phase contributions. Spine 33, 1731-1738.

Danielsson, M., et al., 2004. Constitutive modeling of porous hyperelastic materials. Mech Mater 36, 347-358.

DeLucca, J.F., et al., 2016. Human cartilage endplate permeability varies with degeneration and intervertebral disc site. J Biomech 49, 550-557.

Derbyshire, W., Duff, I., 1974. NMR of agarose gels. Faraday discussions of the chemical society 57, 243-254.

Deyo, R.A., Bass, J.E., 1989. Lifestyle and low-back pain. The influence of smoking and obesity. Spine 14, 501-506.

Donnan, F.G., 1924. The theory of membrane equilibria. Chemical Reviews 1, 73-90.

Dullerud, R., Johansen, J.G., 1995. CT-diskography in patients with sciatica. Comparison with plain CT and MR imaging. Acta radiologica 36, 497-504.

Ebara, S., et al., 1996. Tensile properties of nondegenerate human lumbar anulus fibrosus. Spine 21, 452-461.

Eberlein, R., et al., 2001. An anisotropic model for annulus tissue and enhanced finite element analyses of intact lumbar disc bodies. Computer methods in biomechanics and biomedical engineering 4, 209-229.

Edelman, R.R., et al., 1994. In vivo measurement of water diffusion in the human heart. Magnetic resonance in medicine : official journal of the Society of Magnetic Resonance in Medicine / Society of Magnetic Resonance in Medicine 32, 423-428.

Ehlers, W., Eipper, G., 1999. Finite elastic deformations in liquid-saturated and empty porous solids. Transport Porous Med 34, 179-191.

Ehlers, W., et al., 2009. An extended biphasic model for charged hydrated tissues with application to the intervertebral disc. Biomech Model Mechan 8, 233-251.

Ehlers, W., Markert, B., 2001. A linear viscoelastic biphasic model for soft tissues based on the Theory of Porous Media. J Biomech Eng 123, 418-424.

Elliott, D.M., Setton, L.A., 2001. Anisotropic and inhomogeneous tensile behavior of the human anulus fibrosus: Experimental measurement and material model predictions. J Biomech Eng-T Asme 123, 256-263.

Evans, R.C., Quinn, T.M., 2005. Solute diffusivity correlates with mechanical properties and matrix density of compressed articular cartilage. Arch Biochem Biophys 442, 1-10.

Eyre, D.R., Muir, H., 1976. Types I and II collagens in intervertebral disc. Interchanging radial distributions in annulus fibrosus. Biochem J 157, 267-270.

Famaey, N., et al., 2013. A three-constituent damage model for arterial clamping in computer-assisted surgery. Biomech Model Mechan 12, 123-136.

Farrell, M.D., Riches, P.E., 2013. On the poisson's ratio of the nucleus pulposus. Journal of biomechanical engineering 135, 104501.

Federico, S., Herzog, W., 2008. On the permeability of fibre-reinforced porous materials. Int J Solids Struct 45, 2160-2172.

Folkman, J., Moscona, A., 1978. Role of cell shape in growth control. Nature 273, 345-349.

Freemont, A.J., et al., 1997. Nerve ingrowth into diseased intervertebral disc in chronic back pain. Lancet 350, 178-181.

Frijns, A.J.H., et al., 1997. A validation of the quadriphasic mixture theory for intervertebral disc tissue. Int J Eng Sci 35, 1419-1429.

Froimson, M.I., et al., 1997. Differences in patellofemoral joint cartilage material properties and their significance to the etiology of cartilage surface fibrillation. Osteoarthr Cartilage 5, 377-386.

Fujita, Y., et al., 1997. Radial tensile properties of the lumbar annulus fibrosus are site and degeneration dependent. J Orthopaed Res 15, 814-819.

Galante, J.O., 1967. Tensile properties of the human lumbar annulus fibrosus. Acta Orthop Scand, Suppl 100:101-191.

Gao, X., Gu, W.Y., 2014. A new constitutive model for hydration-dependent mechanical properties in biological soft tissues and hydrogels. J Biomech 47, 3196-3200.

Gray, M.L., et al., 1988. Mechanical and physicochemical determinants of the chondrocyte biosynthetic response. J Orthopaed Res 6, 777-792.

Gray, M.L., et al., 1989. Kinetics of the chondrocyte biosynthetic response to compressive load and release. Biochim Biophys Acta 991, 415-425.

Gu, W., et al., 2014. Simulation of the progression of intervertebral disc degeneration due to decreased nutritional supply. Spine (Phila Pa 1976) 39, E1411-1417.

Gu, W.Y., et al., 1998. A mixture theory for charged-hydrated soft tissues containing multi-electrolytes: Passive transport and swelling behaviors. J Biomech Eng-T Asme 120, 169-180.

Gu, W.Y., et al., 1996. A technique for measuring volume and true density of the solid matrix of cartilaginous tissues, Advance in Bioengineering, ASME BED, pp. 89-90.

Gu, W.Y., et al., 1999. The anisotropic hydraulic permeability of human lumbar anulus fibrosus - Influence of age, degeneration, direction, and water content. Spine 24, 2449-2455.

Gu, W.Y., Yao, H., 2003. Effects of hydration and fixed charge density on fluid transport in charged hydrated soft tissues. Ann Biomed Eng 31, 1162-1170.

Gu, W.Y., et al., 2003. New insight into deformation-dependent hydraulic permeability of gels and cartilage, and dynamic behavior of agarose gels in confined compression. J. Biomech. 36, 593-598.

Gu, W.Y., et al., 2004. Diffusivity of ions in agarose gels and intervertebral disc: effect of porosity. Ann Biomed Eng 32, 1710-1717.

Guerin, H.A.L., Elliott, D.M., 2006. Degeneration affects the fiber reorientation of human annulus fibrosus under tensile load. J Biomech 39, 1410-1418.

Guilak, F., et al., 2002. The effects of osmotic stress on the viscoelastic and physical properties of articular chondrocytes. Biophysical journal 82, 720-727.

Guilak, F., et al., 1994. The effects of matrix compression on proteoglycan metabolism in articular cartilage explants. Osteoarthritis and cartilage / OARS, Osteoarthritis Research Society 2, 91-101.

Guilak, F., Mow, V.C., 2000. The mechanical environment of the chondrocyte: a biphasic finite element model of cell-matrix interactions in articular cartilage. J Biomech 33, 1663-1673.

Guilak, F., et al., 1995. Chondrocyte deformation and local tissue strain in articular cartilage: a confocal microscopy study. J Orthop Res 13, 410-421.

Haefeli, M., et al., 2006. The course of macroscopic degeneration in the human lumbar intervertebral disc. Spine 31, 1522-1531.

Hardin, J., et al., 2011. Becker's World of the Cell. Pearson.

Hassett, G., et al., 2003. Risk factors for progression of lumbar spine disc degeneration: the Chingford Study. Arthritis Rheum 48, 3112-3117.

Hatami-Marbini, H., Etebu, E., 2013. Hydration dependent biomechanical properties of the corneal stroma. Experimental eye research 116, 47-54.

Heikkila, J.K., et al., 1989. Genetic and environmental factors in sciatica. Evidence from a nationwide panel of 9365 adult twin pairs. Ann Med 21, 393-398.

Heliovaara, M., 1989. Risk factors for low back pain and sciatica. Ann Med 21, 254-264.

Heneghan, P., Riches, P.E., 2008. The strain-dependent osmotic pressure and stiffness of the bovine nucleus pulposus apportioned into ionic and non-ionic contributors. J Biomech 41, 2411-2416.

Heuer, F., et al., 2007. Stepwise reduction of functional spinal structures increase range of motion and change lordosis angle. J Biomech 40, 271-280.

Holm, S., et al., 2004. Experimental disc degeneration due to endplate injury. J Spinal Disord Tech 17, 64-71.

Holm, S., et al., 1981. Nutrition of the intervertebral disc: solute transport and metabolism. Connect Tissue Res 8, 101-119.

Holmes, M.H., Mow, V.C., 1990. The nonlinear characteristics of soft gels and hydrated connective tissues in ultrafiltration. J Biomech 23, 1145-1156.

Holz, M., et al., 2000. Temperature-dependent self-diffusion coefficients of water and six selected molecular liquids for calibration in accurate H-1 NMR PFG measurements. Phys Chem Chem Phys 2, 4740-4742.

Holzapfel, G.A., et al., 2000. A new constitutive framework for arterial wall mechanics and a comparative study of material models. J Elasticity 61, 1-48.

Holzapfel, G.A., et al., 2005. Single lamellar mechanics of the human lumbar anulus fibrosus. Biomech Model Mechan 3, 125-140.

Horner, H.A., et al., 2002. Cells from different regions of the intervertebral disc - Effect of culture system on matrix expression and cell phenotype. Spine 27, 1018-1028.

Horner, H.A., Urban, J.P.G., 2001. 2001 Volvo Award winner in basic science studies: Effect of nutrient supply on the viability of cells from the nucleus pulposus of the intervertebral disc. Spine 26, 2543-2549.

Hu, Y.H., et al., 2012. Indentation: A simple, nondestructive method for characterizing the mechanical and transport properties of pH-sensitive hydrogels. J Mater Res 27, 152-160.

Iatridis, J.C., ap Gwynn, I., 2004. Mechanisms for mechanical damage in the intervertebral disc annulus fibrosus. Journal of Biomechanics 37, 1165-1175.

Iatridis, J.C., et al., 2009. Spatially resolved streaming potentials of human intervertebral disk motion segments under dynamic axial compression. J Biomech Eng-T Asme 131.

Iatridis, J.C., et al., 1999. Shear mechanical properties of human lumbar annulus fibrosus. J Orthopaed Res 17, 732-737.

Iatridis, J.C., et al., 2003. Influence of fixed charge density magnitude and distribution on the intervertebral disc: Applications of a poroelastic and chemical electric (PEACE) model. J Biomech Eng-T Asme 125, 12-24.

Iatridis, J.C., et al., 2007. Measurements of proteoglycan and water content distribution in human lumbar intervertebral discs. Spine 32, 1493-1497.

Iatridis, J.C., et al., 2006. Effects of mechanical loading on intervertebral disc metabolism in vivo. J Bone Joint Surg Am 88a, 41-46.

Iatridis, J.C., et al., 1998. Degeneration affects the anisotropic and nonlinear behaviors of human anulus fibrosus in compression. J Biomech 31, 535-544.

Iatridis, J.C., et al., 1997a. Alterations in the mechanical behavior of the human lumbar nucleus pulposus with degeneration and aging. J Orthopaed Res 15, 318-322.

Iatridis, J.C., et al., 1997b. The viscoelastic behavior of the non-degenerate human lumbar nucleus pulposus in shear. J Biomech 30, 1005-1013.

Iatridis, J.C., et al., 1996. Is the nucleus pulposus a solid or a fluid? Mechanical behaviors of the nucleus pulposus of the human intervertebral disc. Spine 21, 1174-1184.

Ishihara, H., Urban, J.P.G., 1999. Effects of low oxygen concentrations and metabolic inhibitors on proteoglycan and protein synthesis rates in the intervertebral disc. J Orthopaed Res 17, 829-835.

Ishihara, H., et al., 1997. Proteoglycan synthesis in the intervertebral disk nucleus: the role of extracellular osmolality. The American journal of physiology 272, C1499-1506.

Jackson, A.R., 2010. Transport and metabolism of glucose in intervertebral disc. University of Miami, Open Access Dissertations.

Jackson, A.R., et al., 2015. Association between intervertebral disc degeneration and cigarette smoking: clinical and experimental findings. JBJS Reviews 3, e2.

Jackson, A.R., et al., 2012. Nutrient transport in human annulus fibrosus is affected by compressive strain and anisotropy. Ann Biomed Eng 40, 2551-2558.

Jacobs, N.T., et al., 2014. Validation and application of an intervertebral disc finite element model utilizing independently constructed tissue-level constitutive formulations that are nonlinear, anisotropic, and time-dependent. J Biomech 47, 2540-2546.

Johannessen, W., Elliott, D.M., 2005. Effects of degeneration on the biphasic material properties of human nucleus pulposus in confined compression. Spine (Phila Pa 1976) 30, E724-729.

Johnson, Z.I., et al., 2014. Extracellular osmolarity regulates matrix homeostasis in the intervertebral disc and articular cartilage: Evolving role of TonEBP. Matrix biology : journal of the International Society for Matrix Biology.

Julkunen, P., et al., 2008. Stress-relaxation of human patellar articular cartilage in unconfined compression: prediction of mechanical response by tissue composition and structure. J Biomech 41, 1978-1986.

Karajan, N., 2012. Multiphasic intervertebral disc mechanics: theory and application. Arch Comput Method E 19, 261-339.

Kauppila, L.I., et al., 1997. Disc degeneration back pain and calcification of the abdominal aorta - A 25-year follow-up study in Framingham. Spine 22, 1642-1647.

Kawaguchi, Y., et al., 2002. The association of lumbar disc disease with vitamin-D receptor gene polymorphism. J Bone Joint Surg Am 84a, 2022-2028.

Kawaguchi, Y., et al., 1999. Association between an aggrecan gene polymorphism and lumbar disc degeneration. Spine 24, 2456-2460.

Kerttula, L., et al., 2001. Apparent diffusion coefficients and T2 relaxation time measurements to evaluate disc degeneration. A quantitative MR study of young patients with previous vertebral fracture. Acta Radiologica 42, 585-591.

Kerttula, L.I., et al., 2000a. Apparent diffusion coefficient in thoracolumbar intervertebral discs of healthy young volunteers. Journal of Magnetic Resonance Imaging : JMRI 12, 255-260.

Kerttula, L.I., et al., 2000b. Post-traumatic findings of the spine after earlier vertebral fracture in young patients: clinical and MRI study. Spine (Phila Pa 1976) 25, 1104-1108.

Kim, E., et al., 2008. The dynamic mechanical environment of the chondrocyte: a biphasic finite element model of cell-matrix interactions under cyclic compressive loading. J Biomech Eng 130, 061009.

Kim, Y.J., et al., 1994. Mechanical regulation of cartilage biosynthetic behavior: physical stimuli. Arch Biochem Biophys 311, 1-12.

Klisch, S.M., Lotz, J.C., 2000. A special theory of biphasic mixtures and experimental results for human annulus fibrosus tested in confined compression. J Biomech Eng 122, 180-188.

Knauss, R., et al., 1999. Self-diffusion of water in cartilage and cartilage components as studied by pulsed field gradient NMR. Magnet Reson Med 41, 285-292.

Korecki, C.L., et al., 2007. Characterization of an in vitro intervertebral disc organ culture system. Eur Spine J 16, 1029-1037.

Korhonen, R.K., et al., 2002. Comparison of the equilibrium response of articular cartilage in unconfined compression, confined compression and indentation. J Biomech 35, 903-909.

Lai, W.M., et al., 1998. On the conditional equivalence of chemical loading and mechanical loading on articular cartilage. J Biomech 31, 1181-1185.

Lai, W.M., et al., 1991. A triphasic theory for the swelling and deformation behaviors of articular cartilage. Journal of Biomechanical Engineering 113, 245-258.

Lai, W.M., Mow, V.C., 1980. Drag-induced compression of articular cartilage during a permeation experiment. Biorheology 17, 111-123.

Laible, J.P., et al., 1993. A poroelastic-swelling finite element model with application to the intervertebral disc. Spine 18, 659-670.

Lanir, Y., 1987. Biorheology and fluid flux in swelling tissues. I. Bicomponent theory for small deformations, including concentration effects. Biorheology 24, 173-187.

Lee, R.C., et al., 1981. Oscillatory compressional behavior of articular cartilage and its associated electromechanical properties. J Biomech Eng-T Asme 103, 280-292.

Li, L.P., et al., 2003. Strain-rate dependent stiffness of articular cartilage in unconfined compression. J Biomech Eng-T Asme 125, 161-168.

Liess, C., et al., 2002. Detection of changes in cartilage water content using MRI T-2-mapping in vivo. Osteoarthr Cartilage 10, 907-913.

Lin, H.S., et al., 1978. Mechanical response of the lumbar intervertebral joint under physiological (complex) loading. J Bone Joint Surg Am 60, 41-55.

Lotz, J.C., 2004. Animal models of intervertebral disc degeneration: lessons learned. Spine (Phila Pa 1976) 29, 2742-2750.

Lotz, J.C., et al., 1998. 1998 Volvo Award winner in biomechanical studies - Compression-induced degeneration of the intervertebral disc: An in vivo mouse model and finite-element study. Spine 23, 2493-2506.

Lotz, J.C., et al., 2002. Mechanobiology of the intervertebral disc. Biochem Soc T 30, 853-858.

Lu, Y.M., et al., 1996. Do bending, twisting, and diurnal fluid changes in the disc affect the propensity to prolapse? A viscoelastic finite element model. Spine 21, 2570-2579.

Lyons, G., et al., 1981. Biochemical changes in intervertebral disc degeneration. Biochim Biophys Acta 673, 443-453.

Mackie, J.S., Meares, P., 1955. The diffusion of electrolytes in a cation-exchange resin membrane .1. Theoretical. Proc R Soc Lon Ser-A 232, 498-509.

Maclean, J.J., et al., 2004. Anabolic and catabolic mRNA levels of the intervertebral disc vary with the magnitude and frequency of in vivo dynamic compression. J Orthop Res 22, 1193-1200.

Maezawa, S., Muro, T., 1992. Pain provocation at lumbar discography as analyzed by computed-tomography discography. Spine 17, 1309-1315.

Marchand, F., Ahmed, A.M., 1990. Investigation of the laminate structure of lumbar disc anulus fibrosus. Spine (Phila Pa 1976) 15, 402-410.

Maroudas, A., 1979. Physicochemical properties of articular carilage. Pitman Medical, London.

Maroudas, A., Evans, H., 1974. Sulfate diffusion and incorporation into human articular cartilage. Biochim Biophys Acta 338, 265-279.

Masaro, L., Zhu, X.X., 1999. Physical models of diffusion for polymer solutions, gels and solids. Prog Polym Sci 24, 731-775.

Masuda, K., et al., 2005. A novel rabbit model of mild, reproducible disc degeneration by an anulus needle puncture: correlation between the degree of disc injury and radiological and histological appearances of disc degeneration. Spine (Phila Pa 1976) 30, 5-14.

Matsui, H., et al., 1998. Familial predisposition for lumbar degenerative disc disease. A case-control study. Spine (Phila Pa 1976) 23, 1029-1034.

Mcnally, D.S., et al., 1993. Can intervertebral disc prolapse be predicted by disc mechanics. Spine 18, 1525-1530.

Mcnally, D.S., Arridge, R.G.C., 1995. An analytical model of intervertebral disc mechanics. J Biomech 28, 53-&.

Melrose, J., et al., 1992. A longitudinal study of the matrix changes induced in the intervertebral disc by surgical damage to the annulus fibrosus. J Orthop Res 10, 665-676.

Miller, J.A., et al., 1988. Lumbar disc degeneration: correlation with age, sex, and spine level in 600 autopsy specimens. Spine (Phila Pa 1976) 13, 173-178.

Moon, S.M., et al., 2013. Evaluation of intervertebral disc cartilaginous endplate structure using magnetic resonance imaging. Eur Spine J 22, 1820-1828.

Mow, V., Guo, X.E., 2002. Mechano-electrochemical properties of articular cartilage: Their inhomogeneities and anisotropies. Annu Rev Biomed Eng 4, 175-209.

Mow, V.C., et al., 1989. Biphasic indentation of articular cartilage--II. A numerical algorithm and an experimental study. J Biomech 22, 853-861.

Mow, V.C., et al., 1984. Fluid transport and mechanical properties of articular cartilage: A review. J Biomech 17, 377-394.

Mow, V.C., et al., 1980. Biphasic creep and stress relaxation of articular cartilage in compression? Theory and experiments. J Biomech Eng-T Asme 102, 73-84.

Nachemso.A, et al., 1970. In vitro diffusion of dye through the end-plates and the annulus fibrosus of human lumbar inter-vertebral discs. Acta Orthopaedica Scandinavica 41, 589-&.

Natarajan, R.N., et al., 1994. A model to study the disc degeneration process. Spine 19, 259-265.

Negoro, K., et al., 2008. Effect of osmolarity on glycosaminoglycan production and cell metabolism of articular chondrocyte under three-dimensional culture system. Clin Exp Rheumatol 26, 534-541.

Nguyen-minh, C., et al., 1998. Measuring diffusion of solutes into intervertebral disks with MR imaging and paramagnetic contrast medium. Am J Neuroradiol 19, 1781-1784.

Nims, R.J., et al., 2014. Synthesis rates and binding kinetics of matrix products in engineered cartilage constructs using chondrocyte-seeded agarose gels. J Biomech 47, 2165-2172.

Ninomiya, M., Muro, T., 1992. Pathoanatomy of lumbar disc herniation as demonstrated by computed tomography/discography. Spine (Phila Pa 1976) 17, 1316-1322.

Nobel, P.S., 1969. The Boyle-Van't Hoff relation. Journal of Theoretical Biology 23, 375-379.

Normand, V., et al., 2000. New insight into agarose gel mechanical properties. Biomacromolecules 1, 730-738.

O'Connell, G.D., et al., 2009. Theoretical and uniaxial experimental evaluation of human annulus fibrosus degeneration. J Biomech Eng-T Asme 131.

O'Connell, G.D., et al., 2011. Axial creep loading and unloaded recovery of the human intervertebral disc and the effect of degeneration. J Mech Behav Biomed 4, 933-942.

O'Connell, G.D., et al., 2012. Human annulus fibrosus material properties from biaxial testing and constitutive modeling are altered with degeneration. Biomech Model Mechanobiol 11, 493-503.

O'Connell, G.D., et al., 2007. Comparison of animals used in disc research to human lumbar disc geometry. Spine 32, 328-333.

O'Conor, C.J., et al., 2014. TRPV4-mediated mechanotransduction regulates the metabolic response of chondrocytes to dynamic loading. Proceedings of the National Academy of Sciences of the United States of America 111, 1316-1321.

Ohshima, H., Urban, J.P., 1992. The effect of lactate and pH on proteoglycan and protein synthesis rates in the intervertebral disc. Spine (Phila Pa 1976) 17, 1079-1082.

Ohshima, H., et al., 1995. Effect of static load on matrix synthesis rates in the intervertebral disc measured in vitro by a new perfusion technique. J Orthop Res 13, 22-29.

Oshima, H., et al., 1993. The use of coccygeal disks to study intervertebral disc metabolism. J Orthopaed Res 11, 332-338.

Osti, O.L., et al., 1990. 1990 Volvo Award in experimental studies. Anulus tears and intervertebral disc degeneration. An experimental study using an animal model. Spine (Phila Pa 1976) 15, 762-767.

Osti, O.L., et al., 1992. Annular tears and disc degeneration in the lumbar spine. A post-mortem study of 135 discs. J Bone Joint Surg Br 74, 678-682.

Oyen, M.L., et al., 2012. Size effects in indentation of hydrated biological tissues. J Mater Res 27, 245-255.

Paassilta, P., et al., 2001. Identification of a novel common genetic risk factor for lumbar disk disease. JAMA 285, 1843-1849.

Peng, B., et al., 2005. The pathogenesis of discogenic low back pain. J Bone Joint Surg Br 87b, 62-67.

Perie, D., et al., 2005. Confined compression experiments on bovine nucleus pulposus and annulus fibrosus: sensitivity of the experiment in the determination of compressive modulus and hydraulic permeability. J Biomech 38, 2164-2171.

Pezowicz, C., 2010. Analysis of selected mechanical properties of intervertebral disc annulus fibrosus in macro and microscopic scale. J Theor App Mech-Pol 48, 917-932.

Pezowicz, C.A., et al., 2006. Mechanisms of anular failure resulting from excessive intradiscal pressure - A microstructural-micromechanical investigation. Spine 31, 2891-2903.

Pope, M.H., et al., 2002. Spine ergonomics. Annu Rev Biomed Eng 4, 49-68.

Poutet, J., et al., 1996. The effective mechanical properties of random porous media. J Mech Phys Solids 44, 1587-1620.

Rajasekaran, S., et al., 2013. ISSLS Prize Winner: The anatomy of failure in lumbar disc herniation. Spine 38, 1491-1500.

Rannou, F., et al., 2003. Cyclic tensile stretch modulates proteoglycan production by intervertebral disc annulus fibrosus cells through production of nitrite oxide. J Cell Biochem 90, 148-157.

Rannou, F.P., et al., 2004. Intervertebral disc degeneration: The role of the mitochondrial pathway in annulus fibrosus cell apoptosis induced by overload. Arthritis Rheum 50, S286-S286.

Roaf, R., 1960. A study of the mechanics of spinal injuries. J Bone Joint Surg Br 42, 810-823.

Roberts, A.P., Garboczi, E.J., 2000. Elastic properties of model porous ceramics. J Am Ceram Soc 83, 3041-3048.

Roberts, S., et al., 1989. Biochemical and structural properties of the cartilage end-plate and its relation to the intervertebral disc. Spine (Phila Pa 1976) 14, 166-174.

Roberts, S., et al., 1996. Transport properties of the human cartilage endplate in relation to its composition and calcification. Spine (Phila Pa 1976) 21, 415-420.

Rodriguez, A.G., et al., 2011. Human disc nucleus properties and vertebral endplate permeability. Spine 36, 512-520.

Rosenberg, L., Schubert, M., 1967. The proteinpolysaccharides of bovine nucleus pulposus. J Biol Chem 242, 4691-4701.

Roughley, P.J., 2004. Biology of intervertebral disc aging and degeneration - Involvement of the extracellular matrix. Spine 29, 2691-2699.

Ruiz, C., et al., 2013. Material property discontinuities in intervertebral disc porohyperelastic finite element models generate numerical instabilities due to volumetric strain variations. J Mech Behav Biomed 26, 1-10.

Sah, R.L.Y., et al., 1989. Biosynthetic response of cartilage explants to dynamic compression. J Orthopaed Res 7, 619-636.

Sambrook, P.N., et al., 1999. Genetic influences on cervical and lumbar disc degeneration - A magnetic resonance imaging study in twins. Arthritis Rheum 42, 366-372.

Sampat, S.R., et al., 2013. Applied osmotic loading for promoting development of engineered cartilage. J Biomech 46, 2674-2681.

Sarkadi, B., Parker, J.C., 1991. Activation of ion transport pathways by changes in cell volume. Biochim Biophys Acta 1071, 407-427.

Schmidt, H., et al., 2013. What have we learned from finite element model studies of lumbar intervertebral discs in the past four decades? J Biomech 46, 2342-2355.

Schmidt, H., et al., 2007. Application of a calibration method provides more realistic results for a finite element model of a lumbar spinal segment. Clin Biomech (Bristol, Avon) 22, 377-384.

Schneiderman, R., et al., 1986. Effects of mechanical and osmotic pressure on the rate of glycosaminoglycan synthesis in the human adult femoral head cartilage: an in vitro study. J Orthopaed Res 4, 393-408.

Schroeder, Y., et al., 2010. A biochemical/biophysical 3D FE intervertebral disc model. Biomech Model Mechan 9, 641-650.

Sen, S., et al., 2012. Human annulus fibrosus dynamic tensile modulus increases with degeneration. Mech Mater 44, 93-98.

Setton, L.A., Chen, J., 2004. Cell mechanics and mechanobiology in the intervertebral disc. Spine (Phila Pa 1976) 29, 2710-2723.

Setton, L.A., Chen, J., 2006. Mechanobiology of the intervertebral disc and relevance to disc degeneration. J Bone Joint Surg Am 88A, 52-57.

Setton, L.A., et al., 1993. Compressive properties of the cartilaginous end-plate of the baboon lumbar spine. J Orthopaed Res 11, 228-239.

Sharma, A., et al., 2009. Association between annular tears and disk degeneration: A longitudinal study. Am J Neuroradiol 30, 500-506.

Shirazi-Adl, A., et al., 2010. Analysis of cell viability in intervertebral disc: Effect of endplate permeability on cell population. J. Biomech. 43, 1330-1336.

Skaggs, D.L., et al., 1994. Regional variation in tensile properties and biochemical composition of the human lumbar anulus fibrosus. Spine 19, 1310-1319.

Smith, L.J., et al., 2011. Degeneration and regeneration of the intervertebral disc: lessons from development. Dis Model Mech 4, 31-41.

Snowden, J., Maroudas, A., 1972. Proteoglycans and physicochemical properties of articular cartilage. Scand J Clin Lab Inv 29, 30-&.

Soltz, M.A., Ateshian, G.A., 2000. Interstitial fluid pressurization during confined compression cyclical loading of articular cartilage. Ann Biomed Eng 28, 150-159.

Stammen, J.A., et al., 2001. Mechanical properties of a novel PVA hydrogel in shear and unconfined compression. Biomaterials 22, 799-806.

Stockwell, R.A., 1979. Biology of cartilage cells. CUP Archive.

Stokes, I.A.F., Gardner-Morse, M., 2016. A database of lumbar spinal mechanical behavior for validation of spinal analytical models. J Biomech 49, 780-785.

Stokes, I.A.F., Iatridis, J.C., 2004. Mechanical conditions that accelerate intervertebral disc degeneration: Overload versus immobilization. Spine 29, 2724-2732.

Stokes, I.A.F., et al., 2011. Refinement of elastic, poroelastic, and osmotic tissue properties of intervertebral disks to analyze behavior in compression. Ann Biomed Eng 39, 122-131.

Sun, D.D.N., Leong, K.W., 2004. A Nonlinear hyperelastic mixture theory model for anisotropy, transport, and swelling of annulus fibrosus. Ann Biomed Eng 32, 92-102.

Sun, D.N., et al., 1999. A mixed finite element formulation of triphasic mechano-electrochemical theory for charged, hydrated biological soft tissues. Int J Numer Meth Eng 45, 1375-1402.

Takahashi, M., et al., 2001. The association of degeneration of the intervertebral disc with 5a/6a polymorphism in the promoter of the human matrix metalloproteinase-3 gene. J Bone Joint Surg Br 83b, 491-495.

Tampier, C., et al., 2007. Progressive disc herniation - An investigation of the mechanism using radiologic, histochemical, and microscopic dissection techniques on a porcine model. Spine 32, 2869-2874.

Tanaka, T., Fillmore, D.J., 1979. Kinetics of swelling of gels. J Chem Phys 70, 1214-1218.

Urban, J.P., McMullin, J.F., 1988. Swelling pressure of the lumbar intervertebral discs: influence of age, spinal level, composition, and degeneration. Spine (Phila Pa 1976) 13, 179-187.

Urban, J.P., Roberts, S., 2003. Degeneration of the intervertebral disc. Arthritis Res Ther 5, 120-130.

Urban, J.P.G., 2002. The role of the physicochemical environment in determining disc cell behaviour. Biochem Soc T 30, 858-864.

Urban, J.P.G., et al., 1993. Regulation of matrix synthesis rates by the ionic and osmotic environment of articular chondrocytes. J Cell Physiol 154, 262-270.

Urban, J.P.G., et al., 1978. Diffusion of small solutes into the intervertebral disc: as in vivo study. Biorheology 15, 203-223.

Urban, J.P.G., Maroudas, A., 1979. The measurement of fixed charged density in the intervertebral disc. Biochim Biophys Acta 586, 166-178.

Urban, J.P.G., et al., 2000. The nucleus of the intervertebral disc from development to degeneration. Am Zool 40, 53-61.

van Dijk, B., et al., 2011. Culturing bovine nucleus pulposus explants by balancing medium osmolarity. Tissue Eng Part C-Me 17, 1089-1096.

van Dijk, B.G.M., et al., 2013. Long-term culture of bovine nucleus pulposus explants in a native environment. Spine J 13, 454-463.

Varlotta, G.P., et al., 1991. Familial predisposition for herniation of a lumbar disc in patients who are less than twenty-one years old. J Bone Joint Surg Am 73, 124-128.

Veres, S.P., et al., 2008. ISSLS prize winner: microstructure and mechanical disruption of the lumbar disc annulus: part II: how the annulus fails under hydrostatic pressure. Spine 33, 2711-2720.

Veres, S.P., et al., 2009. The morphology of acute disc herniation: a clinically relevant model defining the role of flexion. Spine (Phila Pa 1976) 34, 2288-2296.

Veres, S.P., et al., 2010. ISSLS prize winner: how loading rate influences disc failure mechanics: a microstructural assessment of internal disruption. Spine 35, 1897-1908.

Vernon-Roberts, B., et al., 1997. Pathogenesis of tears of the anulus investigated by multiple-level transaxial analysis of the T12-L1 disc. Spine (Phila Pa 1976) 22, 2641-2646.

Wade, K.R., et al., 2015. "Surprise" loading in flexion increases the risk of disc herniation due to annulus-endplate junction failure a mechanical and microstructural investigation. Spine 40, 891-901.

Walsh, A.J.L., Lotz, J.C., 2004. Biological response of the intervertebral disc to dynamic loading. J Biomech 37, 329-337.

Watase, M., Nishinari, K., 1983. Rheological properties of agarose gels with different molecular weights. Rheol Acta 22, 580-587.

Wilke, H.J., et al., 1999. New in vivo measurements of pressures in the intervertebral disc in daily life. Spine 24, 755-762.

Williamson, A.K., et al., 2001. Compressive properties and function-composition relationships of developing bovine articular cartilage. J Orthop Res 19, 1113-1121.

Wilson, W., et al., 2005. A comparison between mechano-electrochemical and biphasic swelling theories for soft hydrated tissues. J Biomech Eng-T Asme 127, 158-165.

Wong, M., et al., 1997. Chondrocyte biosynthesis correlates with local tissue strain in statically compressed adult articular cartilage. J Orthopaed Res 15, 189-196.

Xia, Y., et al., 1994. Diffusion and relaxation mapping of cartilage-bone plugs and excised disks using microscopic magnetic resonance imaging. Magnet Reson Med 31, 273-282.

Yao, H., Gu, W.Y., 2004. Physical signals and solute transport in cartilage under dynamic unconfined compression: Finite element analysis. Ann Biomed Eng 32, 380-390.

Yao, H., Gu, W.Y., 2006. Physical signals and solute transport in human intervertebral disc during compressive stress relaxation: 3D finite element analysis. Biorheology 43, 323-335.

Yao, H., Gu, W.Y., 2007. Convection and diffusion in charged hydrated soft tissues: a mixture theory approach. Biomech Model Mechan 6, 63-72.

Yoganandan, N., et al., 1988. Microtrauma in the lumbar spine: a cause of low back pain. Neurosurgery 23, 162-168.

Yu, S.W., et al., 1989. Comparison of MR and diskography in detecting radial tears of the anulus: a postmortem study. AJNR Am J Neuroradiol 10, 1077-1081.

Zhu, Q., et al., 2014. Temporal changes of mechanical signals and extracellular composition in human intervertebral disc during degenerative progression. J Biomech.

Zhu, Q., et al., 2012. Cell viability in intervertebral disc under various nutritional and dynamic loading conditions: 3d Finite element analysis. J. Biomech. 45, 2769-2777.

Zhu, Q.Q., et al., 2016. Simulation of biological therapies for degenerated intervertebral discs. J Orthopaed Res 34, 699-708.